Institut für Physik und Astronomie
Arbeitsgruppe III

A Dark Matter line search using 3D-modeling of Cherenkov showers below 10 TeV with VERITAS

Dissertation
zur Erlangung des akademischen Grades
"doctor rerum naturalium"
(Dr. rer. nat.)
in der Wissenschaftsdisziplin "Theoretische Astroteilchenphysik"

eingereicht an der
Mathematisch-Naturwissenschaftlichen Fakultät
der Universität Potsdam

von
Nils Håkansson

Potsdam, den 12th July 2017

Published online at the
Institutional Repository of the University of Potsdam:
URN urn:nbn:de:kobv:517-opus4-397670
http://nbn-resolving.de/urn:nbn:de:kobv:517-opus4-397670

Zusammenfassung

"A Dark Matter line search using 3D-modeling of Cherenkov showers below 10 TeV with VERITAS" von Nils Håkansson.
Dunkle Materie, DM, wurde noch nicht direkt beobachtet, aber die Theorie ist sehr solide. Es gibt Beobachtungen, die als indirekte Beweise gelten, z.B. galaktische Rotationskurven, die besagen, dass Galaxien zu schnell rotieren um ohne eine zusätzliche Massenkomponente zusammenhalten zu können, oder elliptische Zwerggalaxien, die massereicher sind als die sichtbare Materie vermuten lässt. Diese Beobachtungen könnten z.B. mit dem Vorhandensein von DM erkärt werden, aber bis jetzt fehlt die Beobachtung eines Phänomens, das ausschließlich durch DM erklärt werden kann. Eine Möglichkeit wäre die Beobachtung einer speziellen Energiesignatur durch Teleskope, welche das Thema der vorliegenden Arbeit ist.

Das Very Energetic Radiation Imaging Telescope Array System, $VERITAS$, ist ein Teleskoparray für Cherenkov-Strahlung. Entsprechend der Theorie sollten Teilchen dunkler Materie annihilieren und z.B. ein $\gamma\gamma$ Paar bilden. Dieses sollte im Teleskop eine spezielle Energiesignatur hinterlassen, nämlich eine monoenergetische Linie bei einer Energie, die der Teilchenmasse entspricht. Diese "smoking-gun" Signatur wird mit einer sliding window Liniensuche bei Energien $< 10\,\mathrm{TeV}$ gesucht.

In der VERITAS Kollaboration werden standardmäßig eine Hillas-Analyse und Nachschlagetabellen aus Teilchensimulationen verwendet, um die Energie des Teilchens zu berechnen, das den Cherenkov-Schauer verursacht hat. Hier wird eine verbesserte Analysemethode verwendet. Dabei wird jeder Schauer als 3D-Gaußkurve modelliert, was die Qualität der Energierekonstruktion erheblich verbessern sollte. Dafür wurden fünf elliptische Zwerggalaxien beobachtet und einzeln sowie insgesamt analysiert, insgesamt $\sim$224 h Beobachtungszeit. Dabei werden zwei verschiedene Teilchensimulationsprogramme verwendet, CARE und GrISU.

In dieser Arbeit wurde die Energieauflösung und die Bias-Korrektur um einige Prozent gegenüber der Standardanalyse verbessert. Es wurde jedoch keine signifikante Linie detektiert. Die vielversprechendste Linie befindet sich bei einer Energie von $\sim 422\,\mathrm{GeV}$ und hat einen Querschnitt von $8.10 \cdot 10^{-24}\mathrm{cm}^3\mathrm{s}^{-1}$ und ein Signifikanzlevel von $\sim 2.73\ \sigma$ bzw. 1.56σ vor bzw. nach statistischer Korrektur. Außerdem wurden obere Grenzwerte für verschiedene Annihilierungsprozesse berechnet. Sie stimmen mit anderen aktuellen Grenzwerten überein ($\sim 8.56 \cdot 10^{-26} - 6.61 \cdot 10^{-23}\mathrm{cm}^3\mathrm{s}^{-1}$). Zukünftig werden mehr Beobachtungsdaten und neue Teleskoparrays, wie das Cherenkov Telescope Array, CTA, mit Hilfe dieser Analysemethode bessere Ergebnisse ermöglichen.

Abstract

"A Dark Matter line search using 3D-modeling of Cherenkov showers below 10 TeV with VERITAS" by Nils Håkansson.
Dark matter, DM, has not yet been directly observed, but it has a very solid theoretical basis. There are observations that provide indirect evidence, like galactic rotation curves that show that the galaxies are rotating too fast to keep their constituent parts, and galaxy clusters that bends the light coming from behind-lying galaxies more than expected with respect to the mass that can be calculated from what can be visibly seen. These observations, among many others, can be explained with theories that include DM. The missing piece is to detect something that can exclusively be explained by DM. Direct observation in a particle accelerator is one way and indirect detection using telescopes is another. This thesis is focused on the latter method.

The Very Energetic Radiation Imaging Telescope Array System, $VERITAS$, is a telescope array that detects Cherenkov radiation. Theory predicts that DM particles annihilate into, e.g., a $\gamma\gamma$ pair and create a distinctive energy spectrum when detected by such telescopes, e.i., a monoenergetic line at the same energy as the particle mass. This so called "smoking-gun" signature is sought with a sliding window line search within the sub-range $\sim 0.3 - 10$ TeV of the VERITAS energy range, $\sim 0.01 - 30$ TeV.

Standard analysis within the VERITAS collaboration uses Hillas analysis and look-up tables, acquired by analysing particle simulations, to calculate the energy of the particle causing the Cherenkov shower. In this thesis, an improved analysis method has been used. Modelling each shower as a 3D-gaussian should increase the energy recreation quality. Five dwarf spheroidal galaxies were chosen as targets with a total of $\sim$ 224 hours of data. The targets were analysed individually and stacked. Particle simulations were based on two simulation packages, CARE and GrISU.

Improvements have been made to the energy resolution and bias correction, up to a few percent each, in comparison to standard analysis. Nevertheless, no line with a relevant significance has been detected. The most promising line is at an energy of $\sim$ 422 GeV with an upper limit cross section of $8.10 \cdot 10^{-24}\text{cm}^3\text{s}^{-1}$ and a significance of $\sim 2.73\ \sigma$, before trials correction and $\sim 1.56\ \sigma$ after. Upper limit cross sections have also been calculated for the $\gamma\gamma$ annihilation process and four other outcomes. The limits are in line with current limits using other methods, from $\sim 8.56 \cdot 10^{-26} - 6.61 \cdot 10^{-23}\text{cm}^3\text{s}^{-1}$. Future larger telescope arrays, like the upcoming Cherenkov Telescope Array, CTA, will provide better results with the help of this analysis method.

Contents

List of Figures

List of Tables

List of Abbreviations

Abbreviation	Expanded
AGN	Active Galactic Nuclei
$b\bar{b}$	Bottom anti-bottom
$c\bar{c}$	Charm anti-charm
CTA	Cherenkov Telescope Array
DM	Dark Matter
dSphs	Dwarf Spheroidal galaxies
Fermi-LAT	Fermi Large Array Telescope
GC	Galactic Centre
IB	Internal Bremsstrahlung
LHC	Large Hadron Collider
LSP	Lightes Supersymmetric Particle
M87	Messier 87
MSSM	Minimal Supersymmetric Standard Model
NFW	Navarro-Frenk-White
SUSY	Super Symmetric
$\tau^+\tau^-$	Tau plus tau minus
$t\bar{t}$	Top anti-top
VERITAS	Very Energetic Radiation Imaging Telescope Array System
W^+W^-	W plus W minus
WIMP	Weakly Interacting Massive Particle
Z^0Z^0	Z zero Z zero

Chapter 1

Introduction and Justification

The Standard Model of particles, SM, contains all observed particles that the physics community knows exist, such as photons, electrons and top-quarks. It divides them up into different groups, gauge bosons, leptons and quarks. Different experiments and observations have been done to test this model, e.g. using particle accelerators to collide protons to see which quarks they are made of. However, not all astrophysical events are explainable with the SM.

A lot of work have gone into explaining what happens in the Universe with what is called the standard model of cosmology. The expansion of the Universe was discovered in the 1920's by Edwin Hubble after observing galaxies moving away from each other by studying their redshifts, i.e. that, on average, the light that is observed from galaxies are shifted red-wards more and more in the electromagnetic spectrum the further away that the galaxies are. This is because the galaxies are moving away from the Milky Way, MW, due to the expansion of space. Later on, the idea that everything had to come from one point, the point where everything is expanding from, was conceived. Here, SM and the old standard model of cosmology ran into problems. Only extended models could explain what happened in the early Universe. From observations of the expanding Universe and how particles behaved under various circumstances, as well as a huge amount of theoretical work, a new standard model of cosmology has evolved, called ΛCDM, which is the current standard model of cosmology.

In ΛCDM, most of the Universe, $\sim 68\%$, consists of dark energy. Of the remaining $\sim 32\%$, DM constitutes the dominant fraction, $\sim 86\%$. Stated differently, $\sim 27\%$ of the Universe is DM, the rest of the matter is "normal" matter, such as quarks.

In ΛCDM it is often assumed that DM is a particle, but always non-baryonic, i.e not the stuff that everything we can see is made of, and even though there is an abundance of theories regarding the particle nature of DM, the particle themselves remain unobserved and a mystery.

Evidence that support the existence of DM and dark energy are observations of, among others, gravitational lensing [28], galaxy rotation curves [37] first observed by Frits Zwicky in the 1930's, and the cosmic microwave background, CMB, anisotropies [8]. These are all well studied but are also all purely gravitational. Astronomical observations require that the DM particles are non-relativistic, i.e. much slower than the speed of light, since this supports the galaxy and galactic cluster formation due to the DM particles not traversing great distances in the early Universe. The DM particles could thus be able to gather densely and subsequently gravitationally trap the normal matter that form galaxies. DM particles moving non-relativistically is also called "cold", from which the CDM, meaning Cold Dark Matter, in ΛCDM comes. DM must be electrically neutral and non-baryonic since studies of the CMB imply that most of the dark matter in the Universe should only interact with ordinary matter and photons via gravity and the weak force. The DM particles must be stable on cosmological time scales because otherwise all of DM that was created in the early universe would already be gone today.

In ΛCDM, one of the most popular type of DM candidate is a Weakly Interacting Massive Particle, $WIMP$. As the name suggests, these particles are assumed to interact with normal matter primarily via weak nuclear interaction and to be massive. WIMPs are typically assumed to be Majorana fermions, meaning they are their own antiparticles and can thus annihilate with themselves, [12]. An annihilating DM particle pair can result in different outcomes, e.g. a $\gamma\gamma$ pair or a γ and a fermion anti-fermion pair. Each outcome has a small chance of occurring. Some WIMPs can naturally reproduce the observed relic abundance of DM today, i.e. the number density of DM particles left over after self-annihilation from when they were in thermal equilibrium in the Early Universe. There are no particles that fit the observation criteria in the SM, but do in extended models.

There are other ways to detect DM than the aforementioned gravitational observations, e.g. direct detection using underground detectors, such as $XENON$, production in particle accelerators such as the Large Hadron Collider, LHC, indirect detection using ground based telescopes such as the Very Energetic Radiation Imaging Telescope Array System, $VERITAS$, or space based telescopes such as the Fermi Large Area Telescope, $Fermi-LAT$.

The same annihilation process that went on in the Early Universe could today produce an observable contribution to the measured cosmic-ray flux on Earth [18], [68], [56], [60], and [64]. In order to produce a large enough signal to be detectable by the two telescope types mentioned, the density of DM particles needs to be high. Today, this can be places like galactic clusters or the galaxies themselves. At, or close to the Galactic centre is a good place, because it is near to Earth. On the other hand, just a high density might not be enough to get a detection in other galaxies. They also need to be more or less free from other sources, there would otherwise be to much noise produced to be able to detect a DM signal. Thus, dwarf spheroidal galaxies, $dSphs$, like Segue 1, are prime candidates. Some dSphs are especially suited because they are relatively close, < 100 kpc, and have very high mass-to-light ratios, M/L, $\mathcal{O}$ 1000 $\mathrm{M}_\odot/\mathrm{L}_\odot$.

When the gamma-rays from the annihilating DM have travelled, in a practically straight line from where they were created, to Earth, they can interact with the atmosphere. The reaction creates Cherenkov radiation as a tertiary product that can be detected using Imaging Atmospheric Cherenkov Telescopes, $IACTs$. Cherenkov radiation is produced because the incoming particle interacts with the atmosphere and creates a cascade of particles, some of which are charged particles. These charged particles are moving faster than the speed of light in the medium thus creating Cherenkov radiation. The Cherenkov radiation comes in the form of a photon shower in the blue wavelength range. The Cherenkov shower comes down in the shape of a cone. There are other cosmic rays, e.g. electrons and hadrons, that also create Cherenkov showers as tertiary outcomes. In order to correctly identify a DM target, the gamma-ray induced showers have to be separated from the non-gamma-ray induced showers when analysing.

In this thesis VERITAS was used to gather data. VERITAS is an IACT array of four telescopes that do indirect detection of gamma-rays. The telescopes are focused at about 12 kilometres height and thus sees a slice of the cone-shaped Cherenkov shower. VERITAS is sensitive in the $0.01 - 30$ TeV range, also known as the very high energy range. In the middle of this range, 1-10 TeV, the detection energy resolution of VERITAS is approximately $15 - 18\%$. Above and below this range in the energy spectrum, the energy resolution is worse. Towards the very edges of VERITAs energy range, the energy resolution worsens to around 35%.
Many of the highly attractive WIMP candidates lie in the low energy range, $0.01 - 0.5$ TeV. For most of this energy range, VERITAS is struggling to get

a good enough resolution and shower reconstruction to be able to detect DM, which is one of the scientific research that VERITAS is used for.
If the data collected by such a system is shown as photon flux versus energy, there are two distinct features that together can only be explained with DM: a continuous part followed by a strong, almost mono-energetic, peak. It is a so-called "smoking gun" signature for DM, [15].

The current standard within the VERITAS collaboration using the Eventdisplay analysis program is to use Hillas analysis, [44]. Hillas analysis is, in simple terms, when the image of the Cherenkov shower on the image plane of the IACT is fitted with an ellipse and the width, length and other parameters are acquired from that. These are then used to get the energy, sky position and other information about the Cherenkov shower. There are other analysis tools within the VERITAS collaboration, e.g. VEGAS, that has approximately equivalent properties as Eventdisplay. Hillas analysis works well, however, the energy resolution and energy threshold are not good enough to detect the practically mono-energetic line that is created when two DM particles annihilate into $\gamma\gamma$. Another difficulty is that this line is often predicted to be close to the lower threshold limit of VERITAS' energy range. Comparing VERITAS with other current telescope arrays shows that they are on equal footing with the observational quality. However, in theory, some of the other telescope arrays uses methods that should be better, such as 3D-modelling of the Cherenkov showers [47]. The 3D-model analysis directly characterises the Cherenkov shower, as opposed to the Hillas analysis method of characterising the shower images. This is done by fitting a 3D Gaussian to the shower itself. This difference removes one step in the analysis of the showers. The 3D-model analysis uses more parameters in the characterisation of a Cherenkov shower. The parameters in the 3D-model analysis, that does not have any equivalent in the Hillas analysis, e.g. the reduced 3D-width of the Gaussian, are almost completely independent of the other parameters and thus create a possibility to get a more accurate representation of the shower. Due to the relative independence of these parameters, the 3D-model analysis should be able to improve upon both the energy resolution and the energy threshold with respect to Hillas analysis. These are some of the reasons to implement the 3D-model in VERITAS data analysis.
Having more semi-independent parameters to cut on will increase the quality of the separation between the gamma and hadron generated Cherenkov showers. This should indirectly make the energy resolution better. Also helping in the gamma/hadron separation is that cuts can be made across

elevations and energies using the 3D-model reduced parameters.
The improvement that can be gained using the 3D-model analysis instead of the Hillas analysis thus comes from a lower energy threshold, better energy resolution and gamma/hadron separation. Several percent improvement in each category suggests that the 3D-model analysis is preferable to the Hillas analysis when searching for line emissions from self-annihilating DM.
Other areas of astrophysics will also benefit from these improvements. The 3D-model analysis will naturally improve on upper limits and low elevation observations. However, this will come at the cost of analysis time. Increasing the overlap with instruments at lower energies, like Fermi-LAT, is of great value for possible joint ventures in the future.

The 3D-model analysis method is one of the focuses of this thesis. Besides the 3D-model analysis itself, this thesis also focuses on acquiring an accurate energy from the simulated data when analysing real data. Using the energy acquired from the 3D-model analysis it is possible to do a search for the mono-energetic DM line. This is the third focus of this thesis. Such searches have been done before. Specifically, [72], became well cited and very popular for a short time for stating to have found a DM line at ~ 130 GeV. This is exactly in the region where VERITAS is struggling with its energy resolution. The findings of the paper were later restudied by the FERMI collaboration, [2], with a final statement that; although the line is no longer significant, $< 2\ \sigma$, there likely is something there that needs to be studied in more detail. Introducing the 3D-model analysis and line search should improve the output results for DM searches at low energies from the VERITAS collaboration.

In the future, it will be possible to apply the same analysis method to the Cherenkov Telescope Array, CTA, [75], which will be a step up for DM searches. This can basically be explained by technological improvements, better IACTs, higher resolution and faster cameras. More telescopes in general, and some larger telescopes will increase the detection area and lower the detection threshold as well.
The structure of this thesis is the following: In Chapter 2, the theory of DM will be discussed, what it is, where it is and how it can be detected using VERITAS. Chapter 3 describes the instrument, VERITAS, used for data acquisition for this thesis. In that chapter, some information on the upcoming CTA is given as well as information on Fermi-LAT with its overlapping energy region. The method that has been used is taken up in Chapter 4. Chapter 5 contains the data selection and reduction. Results are shown in Chapter 6 followed by Chapter 7 which has the conclusions and discussion.

Chapter 2

Theory

For this thesis, there is no intention of creating a new DM theory or propose a new DM particle candidate, but rather to use an advanced analysis method, the 3D-model with 3D-energy, to find out how a signal from DM is created, and how to improve the method.
It is still unknown what DM is. Analysis of galactic rotation curves and galaxy group movement have shown that mass is missing in comparison to what can be calculated from the light spectrum, i.e. something dark is missing [27]. Further observations, such as studies of the CMB anisotropy power spectrum, and intricate theories of the beginning of the Universe show that $\sim 25\%$ of the Universe consists of this dark missing component. In this thesis it is assumed that the ΛCDM is valid. In this chapter DM models, DM particle candidates, DM distribution, the signals that should be coming from the DM annihilation and how these interact with the atmosphere to create the Cherenkov radiation. The theory behind how the showers are reconstructed will also be discussed.

2.1 Dark Matter Models

There are many possible DM candidates. These candidates are not in the standard model of particles, see the left half of Fig.2.1. The DM particles belong to expanded theories, see the right half of Fig.2.1 and in [49]. However, not all expanded theories contain a DM particle candidate. The most prevailing theories, which often include DM candidates, are SUperSYmetric models, $SUSY$, and the Minimal Supersymmetric Standard Model, $MSSM$.

2.1.1 SUSY and MSSM

SUSY refers to the possibility that all the standard model particles have a heavier SUSY partner. The first functioning SUSY concept was created to explain, among other concepts, the hierarchy problem, e.g why gravity is 10^{24} times weaker than the weak force. Particles conveniently named "s" in front of the name of the standard model particle, and the force carriers gets an added "ino" at the end. Examples of this naming convention are stau and wino.

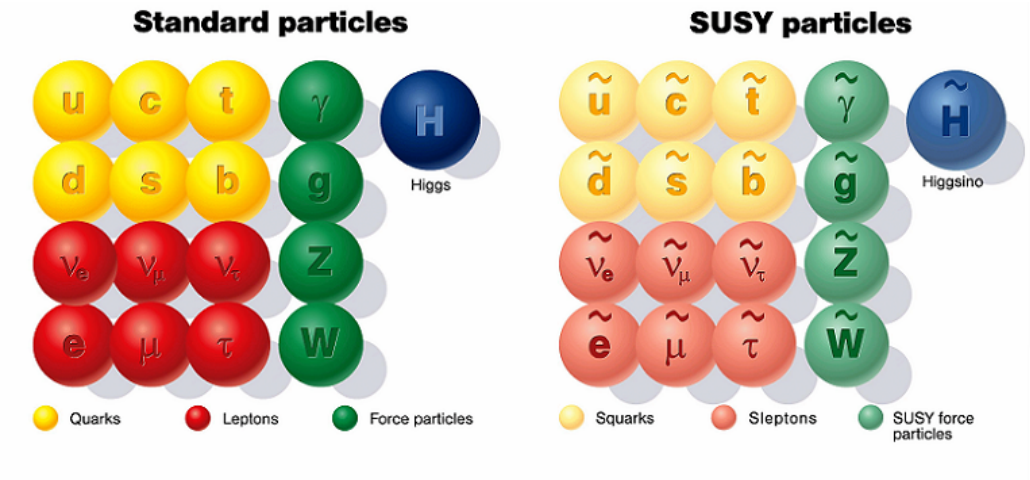

Figure 2.1: An overview of the different particle types in SUSY. The left half shows the standard model particles. The right half shows the extra SUSY particles. The figure is taken from [63].

In Fig. 2.1, it is assumed that the Higgs boson exists, which was validated during the time of this thesis, as it was announced that the Higgs boson had been found at LHC, [25], in 2012. This was a major breakthrough for science and it supports the theory of DM. However, it does remain to be seen which Higgs particle it is since there are many possibilities, [1].
MSSM attempts to explain DM and other phenomena by expanding the standard model as little as possible, requiring as few assumptions as possible, but still explaining interactions consistent with phenomenology.
Finding the Higgs has given support to the theory that some SUSY models could be correct. Which of the many possible MSSM particles are possible DM candidates will be discussed in the following section.

2.2 Dark Matter Particle Candidates

2.2.1 Majorana WIMPs and the LSP

A dark matter candidate in the MSSM is often assumed to be a Majorana particle because they need to be able to annihilate with themselves to create the correct amount of DM in today's Universe, [12].
The Lightest Supersymmetric Particle, LSP, that is also a DM candidate is the neutralino, which is a Majorana fermion. It is the supersymmetric partner to the neutrino, and as such it has the properties to be electrically neutral, massive, weakly interactive, and created cold. The term "cold", as already explained, refers to the particles moving much slower than the speed of light. These are the exact criteria needed for DM, and the neutralino is generally considered to be one of the most promising DM candidates. This got called the "WIMP miracle" when the already proposed WIMPs fitted with what was needed form observations of DM and the CMB. The WIMPs where proposed to explain the surprisingly low neutrino flux coming from the Sun, creating a heavy particle that collect in the centre of the Sun and cooling it down slightly, thus lowering the neutrino flux.
There are many possible masses and cross sections for DM candidates, as can be seen in the following figure:

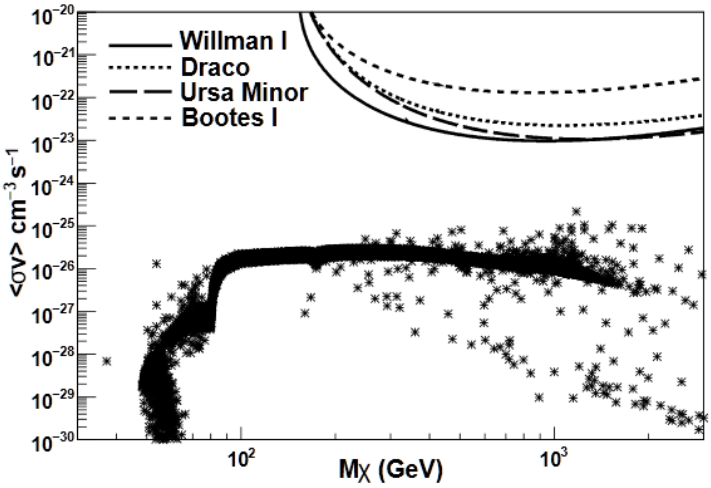

Figure 2.2: DM mass parameter space excluded by previous studies. Each star is a possible candidate. The figure is taken from [3].

The predicted mass of the DM WIMP generally falls into the range of a few 100 GeV, [14]. There are competing theories to WIMPs for the title of DM, such as Axions, [36], who were proposed to explain the strong charge parity problem i.e that charge parity, CP, is conserved in Quantum Chromo Dynamics, QCD, even though QCD is part of the standard model where CP should not be conserved, [19], but these are not in focus for this thesis.

2.2.2 Relic Abundance

The Friedmann equations, [53] or any good book on general relativity and cosmology, describes the expansion of space within a general relativistic framework assuming that the Universe is homogeneous and isotropic. The first equation describes the mass-energy density composition of today's Universe:

$$\frac{H^2}{H_0^2} = \Omega_R + \Omega_M + \Omega_k + \Omega_\Lambda, \tag{2.1}$$

where, from observations at different size scales and the CMB anisotropy power spectrum [46], most of the parameter terms are very well known in relation to the Universe's mass-energy budget. H is the Hubble parameter, which is the expansion rate of the Universe in units of 100 $\text{kms}^{-1}\text{Mpc}^{-1}$, at some earlier point in time, and H_0 is the Hubble parameter at the current time. $\Omega_R \approx 0\%$ is the radiation density today, $\Omega_M \approx 30\%$ is the total matter density (dark and visible matter with 27% and 3% respectively). $\Omega_k \approx 0\%$ is the spatial curvature density and $\Omega_\Lambda \approx 70\%$ is the vacuum density.
In the very early Universe, the temperature was very high and the Universe was in thermo-dynamical equilibrium, meaning that the number density of any particle species was roughly equal to the number density of photons. The particles of a species being constantly created and annihilated. As long as the temperature remained higher than the mass of the particle, the number of photons and the number of particles of that particle species would decrease together as time passed and the Universe expanded. When later the temperature dropped below the mass of the particle species, the number density of that species dropped exponentially. The particle species number density "froze out" of the thermo-dynamical equilibrium and left a substantial number of that particle species today. This is called the relic abundance of the species. A detailed description of this with simplifications made can be found in, [46] and in the above-mentioned paper and books.

For DM WIMPs the DM density, $\Omega_{\rm DM}$, using the Boltzmann equation is:

$$\Omega_{\rm DM}h^2 \approx \frac{3 \cdot 10^{-27}{\rm cm}^3{\rm s}^{-1}}{<\sigma\nu>} \simeq 0.1. \tag{2.2}$$

Here, h is the Planck constant, $<\sigma\nu>$ the DM velocity averaged cross-section and the 0.1 is an observed quantity in today's Universe, [46] and comes from studying the anisotropy power spectrum of the CMB, fitting all density parameters form Eq. 2.1 on the global scale, as measured by the Wilkinson Microwave Anisotropy Probe, $WMAP$, and others,[65]. The DM annihilation cross section should thus be on the scale of $10^{-26}{\rm cm}^3{\rm s}^{-1}$.
The missing mass relic abundance, from the time of thermal decoupling, that is observable today, fits with the theoretical predictions for DM.

2.3 Dark Matter Distribution

How are these DM particles distributed in the Universe as a whole and on smaller scales such as in galaxies and planetary systems?
For this thesis, it is only relevant how DM is distributed in galaxies. However, for the larger scale, according to simulations, DM should be distributed as a web-like structure with filaments, [48]. On the scale of planetary systems, such as the Solar system, the DM density seems to be low, [57].

On the galactic scale, DM is contained within halos around the galaxies. The two most frequently used DM mass distribution profiles that describes the DM halo density distribution of galaxies are the Navarro-Frenk-White, NFW, profile and the Einasto profile.
The following is the generalised NFW profile, [72]:

$$\rho_{\rm NFW}(r) \propto \frac{1}{(\frac{r}{r_s})^{\alpha}(1+\frac{r}{r_s})^{3-\alpha}}, \tag{2.3}$$

where the profile density, $\rho_{\rm NFW}$, is a function of radius, r, with the scale length r_s, [66], and α is a fit parameter of simulations. Based on the MW, the density is normalised to the fiducial value $\rho_{NFW}(r_0) = 0.4\ \frac{\rm GeV}{\rm cm^3}$ at the Suns distance from the Galactic centre, and the scaling radius is $r_s = 20$ kpc. In case of an inner slope of $\alpha = 1$, Eq. 2.3 reproduces the standard NFW profile.

The very similar Einasto profile can be described by the following general equation, [66]:

$$\rho_{\mathrm{E}}(\mathrm{r}) = \rho_0 \exp\left[-2\mathrm{n}\left\{\left(\frac{\mathrm{r}}{\mathrm{r_s}}\right)^{\frac{1}{\mathrm{n}}} - 1\right\}\right], \tag{2.4}$$

where $\rho_0 = 1.1 \cdot 10^8 \mathrm{M}_\odot$ kpc^{-3} is a normalisation factor, $r_s = 0.15$ kpc and $n = 3.3$, which are a scale length and a fit parameter respectively, for the MW according to [10]. These profiles generally have very similar features. There are however some differences, the most prominent being that the NFW profile goes to a non-physical infinity in the centre due to its divergent nature, which the Einasto profile does not. The NFW profile is usually set to a constant value from the core out to some fixed radius to correct for this.

2.4 Dark Matter Signal

With telescopes like VERITAS, it is not possible to directly observe DM, since VERITAS observes the Cherenkov radiation that is the result of gamma-rays interacting with the atmosphere that pair-produces and subsequent atmospheric interactions emit bremsstrahlung photons, see Sec. 2.5. There are two main ways to get from the DM particles to the needed gamma-rays, DM self-annihilation and DM decay.

However, before describing the signal coming from annihilation and decay it is important to understand the astrophysical J-factor.

2.4.1 J-factor

The J-factor is a scaling factor applied to the gamma-ray flux coming from dSphs, and it is dependent on the distance and source type, but not the DM particle physics model. This is because the J-factor describes the density distribution of DM in an astrophysical system and is integrated over the line of sight. It determines the strength of the signal provided by annihilating or decaying DM.
The J-factor for annihilating DM, can be described by, [24]:

$$J_\gamma(\Delta\Omega) = \int_{\Delta\Omega} d\Omega \int_{l.o.s} \rho^2_{\mathrm{DM}}(s, \Omega) ds, \tag{2.5}$$

where $s \geq 0$ is the path-length coordinate along the line-of-sight, Ω is the solid angle of the source, ρ_{DM} is the DM density profile, discussed in Sec. 2.3. The distance to the extended object is given by $r(s)$ and

$$\Delta\Omega = 2\pi[1 - \cos(\alpha_{\text{int}})], \tag{2.6}$$

with Ω being the solid angle, and α_{int} being the integration angle.
For decaying DM ρ^2 becomes ρ which is due to having the decay from each DM particle instead of the annihilation from pairs, [39].

2.4.2 Dark Matter Self-annihilation

If the dark matter particle is a Majorana fermion it can annihilate with itself, and since the DM particles are not electrically charged they can, due to the law of conservation of charge etc., create two gamma-ray photons.
It is however not as simple as there only being one possible DM self-annihilation channel. WIMP DM can annihilate into fermion, boson and quark pairs in different forms. Examples for the boson pairs are W^+W^- and Z^0Z^0, and an example of a lepton pair is $\tau^+\tau^-$, see [34], [13] and references therein. Top anti-top, $t\bar{t}$, bottom anti-bottom, $b\bar{b}$, and charm anti-charm, $c\bar{c}$, are all possible quark combinations that can be the result of WIMP DM annihilation. The exact mechanism for the annihilation depends on which particle is the DM particle. Fig. 2.3 shows Feynman sketches of possible alternatives.

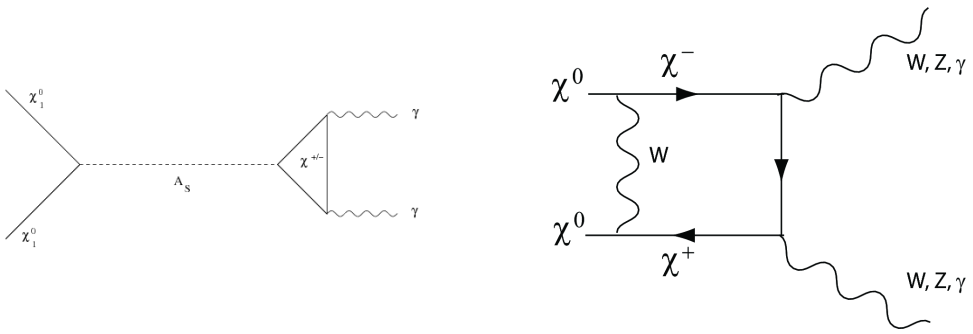

Figure 2.3: Two DM particles annihilating through possible mechanisms into for example photons. The left figure is taken from [34], and the right figure is taken from [13].

When the result of two annihilating DM particles is two SM particles, each of the resulting particles will have the same energy as each of the original DM particles. This is the highest energy any resulting particle can have from an annihilation of two DM particles, because all the energy is split equally due to momentum conservation. If there are more resulting SM particles, e.g. a photon and a fermion anti-fermion pair, they generally do not split the energy equally. A flux versus energy spectrum of the gathered Cherenkov light coming from the gamma-rays interacting with the Earths atmosphere would look like a continuous spectrum up until the end where there would be a very thin line, [16]. This is the so-called "smoking gun" signature of the annihilating DM particle. The line should be at an energy that is in principal the mass of the DM particle. Fig. 2.4 shows a model of what it in principal could look like.

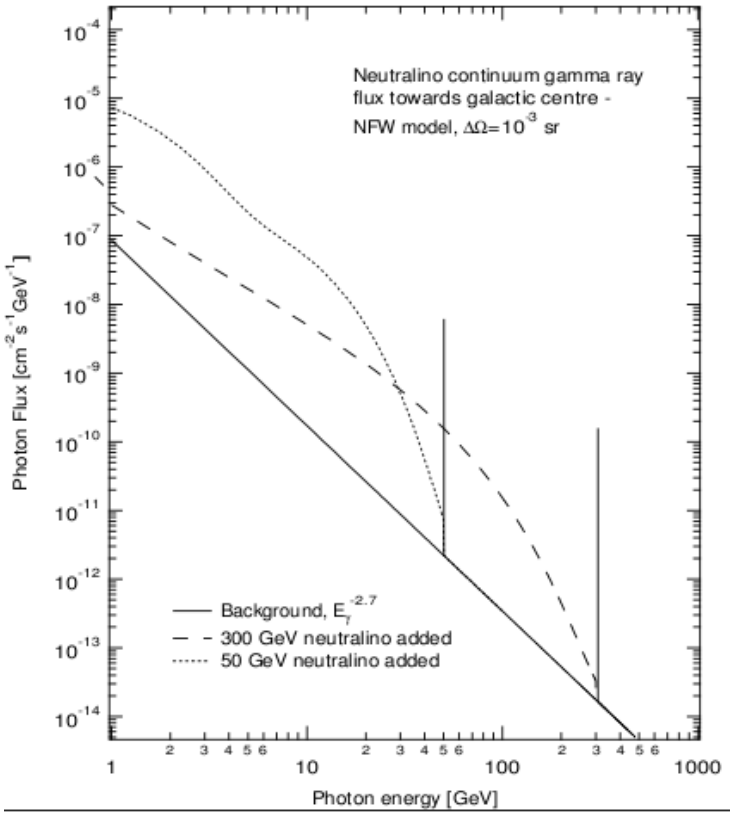

Figure 2.4: How a DM annihilation spectrum theoretically (in a perfect world) could look. The two sharp lines comes from direct annihilation into $\gamma\gamma$. To the left of the two sharp lines is the continuous flux. The figure is taken from [16].

Note that the dual photon outcome is helicity suppressed and thus very weak. This means that due to the conservation of momentum and the projection of the spin onto the direction of linear momentum there are less possible outcomes, see [22] and references therein. There are alternative outcomes, called internal bremsstrahlung, IB, in which two fermions and a photon are produced. The big difference is that the photon does not necessarily have the same energy as the incoming DM particles. This will result in an altogether widening of the line and no sharp drop-off. The benefit of this three-particle outcome is that it is not suppressed. Fig. 2.5 show a Feynman diagram of a possible outcome of the DM annihilation, and Fig. 2.6 shows how the energy spectrum can look.

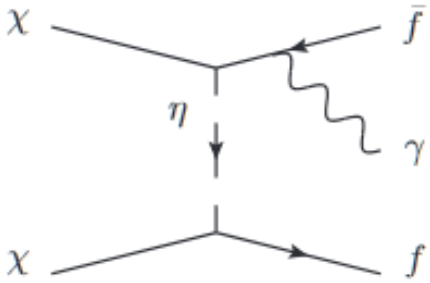

Figure 2.5: A Feynman diagram of a possible outcome from two DM particles annihilating. The figure was taken from [22].

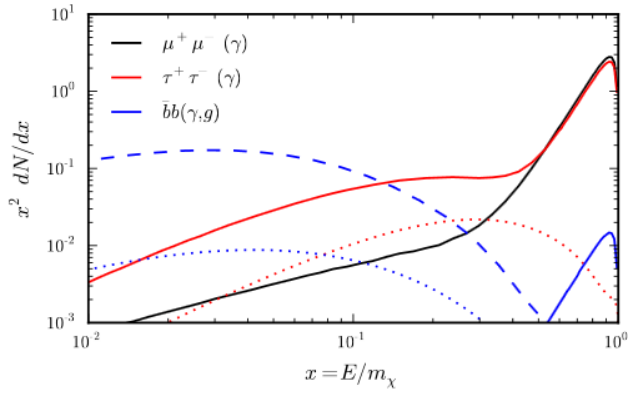

Figure 2.6: Gamma-ray spectrum where N denotes the number of photons produced per annihilation, as predicted by a toy model for different final-state fermions, $\bar{b}b$, $\tau^+\tau^-$ and $\mu^+\mu^-$, assuming the mass of the DM particle is 200 GeV. x is the energy over mass ratio. The solid and dotted lines are from three-body and two-body outcomes respectively. The figure is taken from [22].

The flux of photons from DM annihilation for some extended source per energy is given by:

$$\frac{d\Phi_\gamma(\Delta\Omega, E)}{dE} = \frac{\langle\sigma\nu\rangle}{8\pi m_\chi^2}\frac{dN_\gamma}{dE}J_\gamma(\Delta\Omega), \tag{2.7}$$

where $J_\gamma(\Delta\Omega)$ is the J-factor from Eq. 2.5, m_χ is the DM mass, $<\sigma\nu>$ is the averaged velocity dependent DM annihilation cross section, $\frac{dN_\gamma}{dE}$ is the differential gamma-ray spectrum. For VERITAS, the dwarf galaxy DM targets can mostly be seen as point sources.

There are three aspects to Eq. 2.7, the left-hand side is the observable part, the right-hand side before the integrals come from particle physics, and the J-factor describes the target.
As could be understood from eq. 2.2, $<\sigma\nu>$ is on the level of 10^{-26} cm^{3}s^{-1} for it to be compatible with the thermal relic abundance, also see [61].

2.4.3 Dark Matter Decay

There is not much difference between the equation of flux rate for DM decay the one for DM annihilation. There are two differences from Eq. 2.7; $\frac{\langle\sigma\nu\rangle}{8\pi m_\chi^2}$ becomes $\frac{\Gamma}{4\pi m_\chi}$, where Γ is the particle decay rate, and ρ^2 becomes ρ, see [39]:

$$\frac{d\Phi_{\gamma D}(\Delta\Omega, E)}{dE} = \frac{\Gamma}{4\pi m_\chi}\frac{dN_\gamma}{dE}\int_{\Delta\Omega} d\Omega \int_{\text{l.o.s}} \rho_x(s,\Omega)ds. \tag{2.8}$$

Using Fig. 2.3 as a reference, for DM decay, instead of a sharp line at the mass of the DM particle it contributes to a wider peak that is at half the energy of the DM particle. This is because of the different secondary particles spreading out the energy and losing some of the energy to other particle types such as electrons and positrons, and that only the energy of one DM particle is available instead of two as in DM annihilation.

2.4.4 Velocity Averaged Cross Section

If no line signal is found then the aim is to constrain the velocity averaged cross section, $< \sigma\nu >$. To make Eq. 2.7 applicable to real observations and to get the cross section upper limit, Eq. 2.7 can be rewritten as:

$$\langle \sigma\nu \rangle = \frac{8\pi m_\chi^2}{J_\gamma(\Delta\Omega)} \frac{N_\gamma}{T_{\rm obs} \int_{E_T}^{m_\chi} A_{\rm Eff}(E) \frac{dN_\gamma}{dE} dE}, \tag{2.9}$$

in which $\frac{N_\gamma}{T_{obs}}$ is the number of gamma-rays coming from the source at a certain energy during the observation time T_{obs}. $A_{\rm Eff}(E)$ is the energy dependent effective area. The integration of $A_{\rm Eff}(E)\frac{dN_\gamma}{dE}$ is done from the energy threshold, $E_{\rm T}$, up to the mass of the DM particle of interest. The energy threshold for a ground based Cherenkov telescope is defined as the peak in the differential rate of a Crab-like source, [29].

For DM annihilation into $\gamma\gamma$, $\frac{dN_\gamma}{dE} = 2$.

2.4.5 Branching-ratios and simulated γ-ray spectra

Only a small fraction of the possible annihilation outcomes has $\gamma\gamma$ as the outcome. The branching ratio, e.i. how much of each outcome there is, for $\gamma\gamma$ is loop-suppressed and is on the order of 10^{-4}, [50]. The term "Loop-suppressed", in short, means that the result of the effect is that the outcome is less likely to occur. Loop-suppression can be drawn with a Feynman diagram to be connected like a loop, hence the name, Fig. 2.7 shows examples of loops:

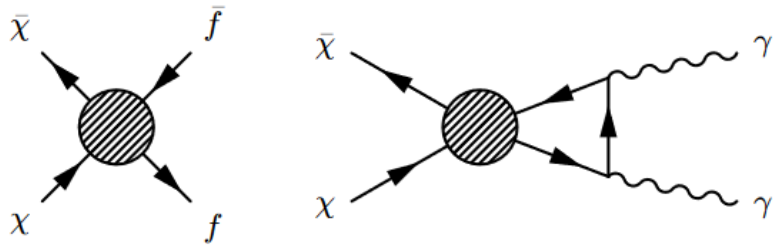

Figure 2.7: Example of Feynman diagrams with loops. The left diagram shows $\chi\bar{\chi} \to f\bar{f}$, and the right diagram shows $\chi\bar{\chi} \to \gamma\gamma$ The figure is taken from [32].

For this thesis, it will be assumed that 100% of the DM annihilations in the energy range of interest goes into any one of $\gamma\gamma$, $b\bar{b}$, W^+W^-, Z^0Z^0 or $\tau^+\tau^-$. Similar to what is done and assumed in [7].
In order to be able to calculate $< \sigma\nu >$ later on, the gamma-ray reference spectra for the different quarks, bosons and leptons are needed. There has been extensive work done in simulating the branching ratios and the resulting photon flux, as can be seen in [23] and [69]. The actual simulation data has not been used for this thesis. However, the equation fitted to the data has been used. From [69], where the simulation programme PYTHIA was used to create particle simulation spectra, there are two equations of interest that describe the different spectra. The first equation describes how the W^+W^-, Z^0Z^0 and $b\bar{b}$ spectra behave.

$$\frac{dN_\gamma}{dx} = x^{a_\tau} \exp(b + cx + dx^2 + ex^3). \tag{2.10}$$

The second equation describes the spectrum for the $\tau^+\tau^-$ branch:

$$\frac{dN_\gamma}{dx} = x^a(b_\tau x + c_\tau x^2 + dx^3) \exp(e_\tau x). \tag{2.11}$$

In Eq. 2.10 and 2.11, $x \equiv \frac{E}{m_\chi}$ for annihilation and $x \equiv 2\frac{E}{m_x}$ for decays, where m_χ is the DM particle mass and the speed of light is set to 1. The different parameters in Eq. 2.10 and 2.11 depend on the particle type of interest. The parameters a_τ, b_τ, c_τ and e_τ can, instead of being constant values like $a - e$ in Eq. 2.10, vary with energy. In that case, they follow the following equation:

$$P_\tau(m_\chi) = \sum_i a_i \log\left(\frac{m_\chi}{1\text{GeV}}\right)^{b_i}, \tag{2.12}$$

where $P_\tau(m_\chi)$ is the mass-dependent parameter of interest from equations 2.10 and 2.11. The iterator i is dependent on which particle outcome is used. The following table shows the parameter values for the individual particle types, and the figure shows examples of simulations used in [69].

Table 2.1: A table for the different parameters in Eq. 2.10 and 2.11. The variables without $_\tau$ are constant values and can be used directly in Eq. 2.10. The parameters with $_\tau$ varies with energy and the a_i/b_i go into Eq. 2.12, where i is the number of a_i/b_i pairs for that parameter, whereafter the result of Eq. 2.12 then goes into Eq. 2.11 where the parameter without $_\tau$ should have gone.

Par.	$\tau^+\tau^-$	$b\bar{b}$	W^+W^-	Z^0Z^0
a	-1.29		-1.36	-1.40
a_τ		$-1.46/0$		
		$+4.26 \cdot 10^{-2}/1$		
		$-4.37 \cdot 10^{-3}/2$		
b	$+7.83$	$+1.05$	$+0.5$	$+0.47$
b_τ	$+6.08/0$			
	$+0.27/1$			
c	-2.70	-17.8	-12.6	-14.4
c_τ	$-6.9/0$			
	$+5.2 \cdot 10^{-4}/1$			
	$-4.2 \cdot 10^{-8}/2$			
	$-1.6 \cdot 10^{-12}/3$			
d	-9.10^{-3}	$+12.3$	$+12.1$	$+16.3$
e	-5.06	-1.86	-9.86	-13.6
e_τ	$-5.25/0$			
	$+0.36/1$			
	$-0.040/2$			

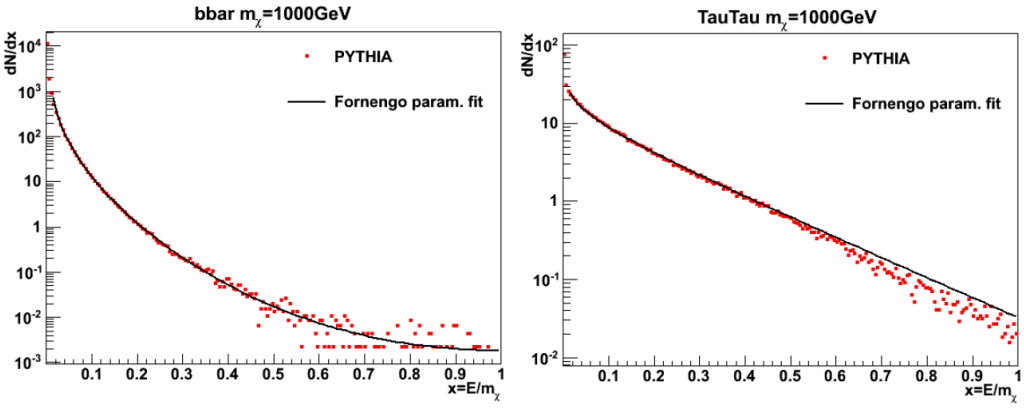

Figure 2.8: Examples of simulated spectra for $b\bar{b}$ and $\tau^+\tau^-$, left and right respectively, at the mass 1000 GeV, simulated by the particle simulation program Pythia. The figures are taken from [69].

The information on these equations, parameters and figures are from [69].

2.5 Gamma-rays and Atmospheric Interaction

When gamma-rays or cosmic rays enter Earth's atmosphere, the interaction can induce different types of particle cascades. If a charged particle, such as electrons that can be the product of pair production, travels faster than the speed of light of the atmosphere, Cherenkov showers can be induced via bremsstrahlung, see Fig. 2.9 and 2.10. Not all showers are of interest to when searching for DM.
There are four types of incoming particles that can, as a subsequent effect, induce Cherenkov showers that can be detected with Cherenkov telescopes, electrons, gamma-rays, protons and atomic nuclei. Each different particle leaving its own, more or less unique, light pool on the ground and shower image in the detectors. See Fig. 2.9 for an impression of a gamma-ray induced Cherenkov shower.

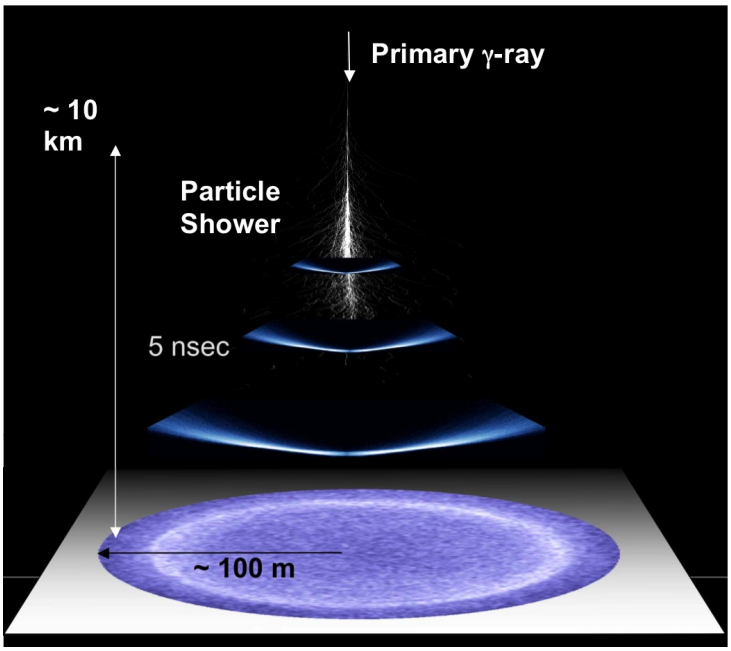

Figure 2.9: A Cherenkov shower induced by a gamma-ray at an average height with an average sized light pool. The figure is taken from [9].

The showers of interest are the ones that are induced by the gamma-ray photons coming from DM targets. Gamma-ray induced shower images are aligned with the source since the Cherenkov shower is more or less parallel to the incoming direction of the gamma-ray.

Another shower type is caused by protons. These are not wanted for this thesis and can, due to their much larger scattering angles and higher transverse movement, be selected against. The protons create a larger light pool in relation to the height in the atmosphere where the shower is created than the gamma-ray photon induced showers do. The light pool itself can also look different, e.g. by being more irregularly shaped.
There is the background of cosmic rays, different atomic nuclei, that are also not wanted. They have similar image properties as the proton induced showers, in that the size and shape of the images are different. The Cherenkov radiation from the cosmic rays is randomly oriented and can thus be discriminated against to a certain extent.

All these variables can be used to do gamma/hadron separation. Fig. 2.10 shows various tertiary particles from cosmic rays which gives an idea of why the light pools can be different.

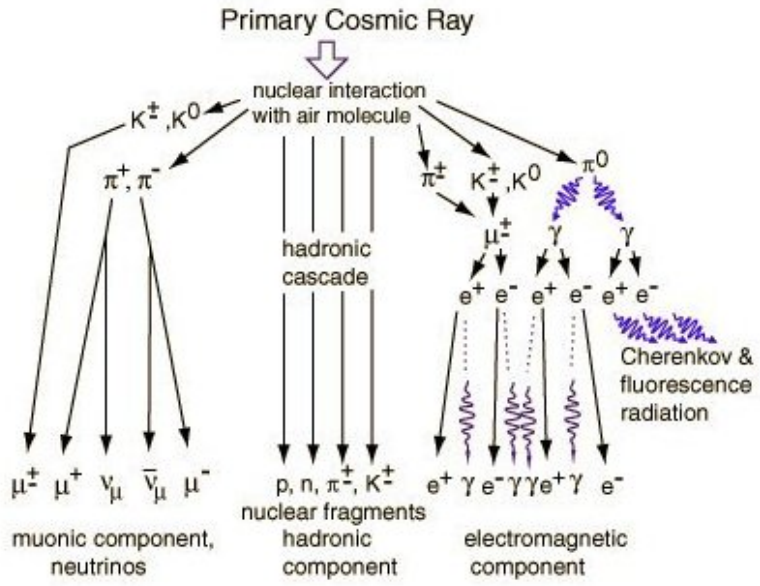

Figure 2.10: Different products of the interaction of cosmic rays with the atmosphere. The figure is taken from "kosack isapp lecture 1" page 152 during the 2013 Paris ISAPP summer school.

The fourth shower type is the hardest to discriminate against. They are induced by electrons or positrons. Because they are charged they can get deflected in magnetic fields and can thus not be aligned with any astrophysical object. The light pool size to distance ratio is almost exactly the same as

the one for photons. This is because electrons and positrons are produced as subsequent particles to photons and vice-versa via pair-production and bremsstrahlung, as can be seen in Fig. 2.11.

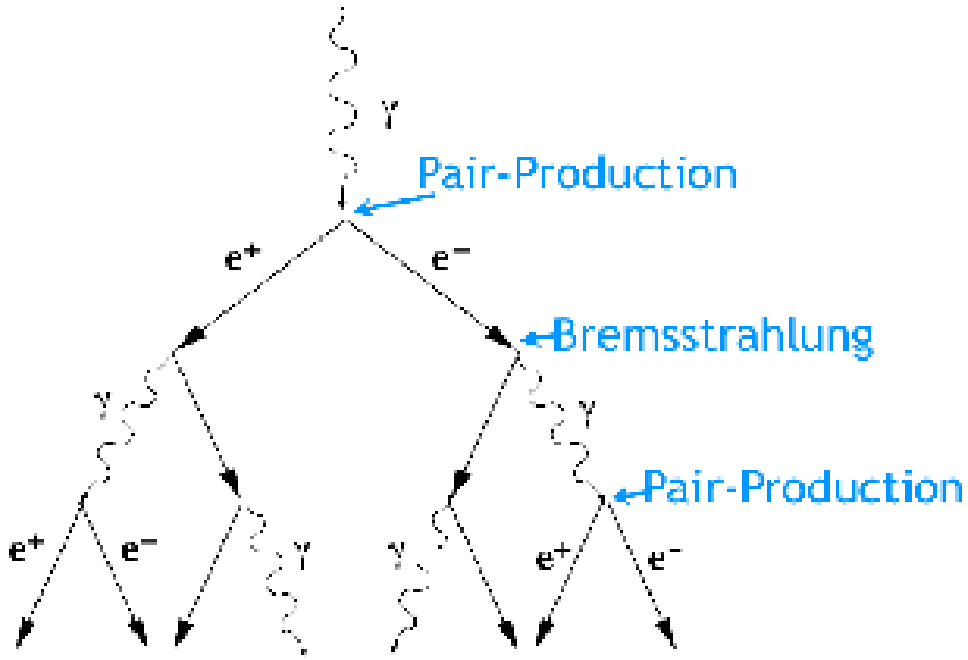

Figure 2.11: Photons pair-produce an electron-positron-pair and these in turn produce photons via bremsstrahlung in the atmosphere. The figure is taken from "kosack isapp lecture 2" page 87 at the 2013 Paris ISAPP summer school.

Statistically looking at the showers from photons and electrons show that there are small differences between them in the shower images [26]. The higher the energy, the larger the differences become. Thus, at the lowest energies for VERITAS, it is very difficult to separate electron induced showers and proton induced showers from the showers created by photons.

When a photon enters the atmosphere, if it has enough energy, it can produce Cherenkov photons as atleast tertiary particles via pair-production, Compton scattering of electrons or positrons in the atmosphere and bremsstrahlung. The minimum energy required for an electron with rest mass, m_e, to emit a Cherenkov photon is described in [58] and by:

$$E_{\min} = \frac{m_e c^2}{\sqrt{1 - \frac{1}{n^2}}}. \tag{2.13}$$

Here c is the speed of light in vacuum, and since both the electron rest mass, $m_e = 9.11 \times 10^{-31}$ kg, and the refractive index of air, $n = 1.000293$, are known, the minimum energy becomes $\sim 3.38 \times 10^{-12}$ Joules or ~ 21.10 MeV. Eq. 2.13 is valid for other charged particles when exchanging the electron rest mass to the rest mass of the other charged particle. The opening angle of the emitted Cherenkov radiation, θ, as seen in Fig. 2.12, can be computed in the following way:

$$\cos\theta = \frac{1}{\beta n}, \tag{2.14}$$

with $\beta = \frac{v}{c}$, where v is the particle velocity. The particle emits Cherenkov light while $v > \frac{c}{n}$, thus, the minimal β for a given refractive index n is calculated by:

$$\beta_{\text{min}} = \frac{1}{n}. \tag{2.15}$$

Assuming $\beta = 1$, the maximum Cherenkov angle is given by the following equation as:

$$\theta_{\text{max}} = \arccos\left(\frac{1}{n}\right). \tag{2.16}$$

As a consequence of the height dependence on the index of refraction, θ_{max} increases with the decreasing height. This is compensated by the fact that a photon with higher energy focuses the radiation. The photon does, however, penetrate deeper into the atmosphere before interacting. Thus, the light pool on the ground caused by the Cherenkov radiation cone changes very little with the energy of the primary photon, see Fig. 2.12.

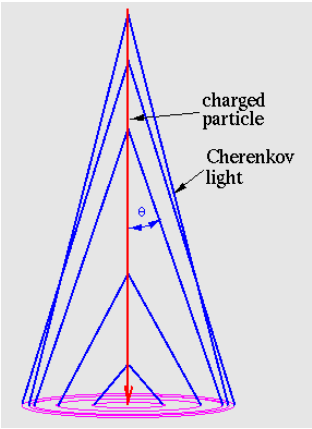

Figure 2.12: θ increases with decreasing height. The figure is taken from [17].

The opening angle of the showers in the energy range GeV-TeV is generally around ~ 1 degree. Since the showers are created at an altitude of around 12,000 meters, the light pool that it creates is approximately 10,000 m^2. To be able to detect the same shower with all telescopes in an array, as is the goal with VERITAS and other current telescope arrays, this 10,000 m^2 area is thus the maximum size for a Cherenkov telescope array in this energy range. If partial images are allowed, or that a shower is not seen be all telescopes is allowed, the ground area covered can be larger.

2.6 Telescope Detection

If the telescopes are within the light pool of a shower, that is within the telescopes' energy range, the shower will likely get detected. The Cherenkov photons get reflected by the mirrors of each telescope, finally focused in via light cones and get collected by the telescopes photo-multipliers. Since most showers do not enter the atmosphere at a perpendicular angle, the Cherenkov shower will also not be perpendicular to the ground. This results in the light pool becoming ovoid-shaped. The telescopes are focused at around 12,000 meters height and thus they image a slice of the cone-shaped Cherenkov shower. Since each telescope in a telescope array is at a different position, a shower will be differently oriented and differently positioned on each image plane. This fact is very important for the localisation and reconstruction of a shower.

2.7 Signal-to-noise Ratio

Independent of the method used to reconstruct the signal, it is important to have large signal-to-noise ratio. The signal and noise estimate are generally acquired from different regions in the telescope image. These regions are called the on- and off-regions. The on-region is where the target source is, and where the wanted signal comes from. The off-region(s) is where the noise estimate is acquired. The way the on- and off-regions are chosen will be discussed in Sec. 4.6. To get the signal to noise ratio it is just a matter of dividing the On-region by the Off-region signals, making sure to scale the Off-region size to match the On-region size if the total Off-region size is different than the On-region size.

2.8 Reconstruction Methods

There are three parts to energy reconstruction, an observational part, a simulation part, and a comparison of the two.

The observational part, in the most basic and naive form, is that the intensity of the Cherenkov light collected by the camera(s) of the telescope(s) is proportional to the energy of the particle creating the shower with some numerical factor weighing in. However, this factor is not linear. It depends on the elevation, and thus the amount of atmosphere that the shower passes through.

Every shower looks slightly different. The randomness in the particle creation in the shower, the incoming angle, where the shower centre hits the ground, vary from shower to shower. It is however not so variable that it is impossible to do generalisations. If enough simulations have been studied, a simulated shower that is similar to the real shower can be found, and thus an energy acquired. Simulations of air-showers are done using sophisticated codes that calculate and trace all the subsequent particles that are created in a shower. Air showers have been simulated from very low energies to very high energies with small energy steps. The simulations have also been done for many incoming angles, in both elevation and azimuth, giving different shower images. Different atmospheres also have to be taken into account, as well as how the telescopes respond. And if the telescopes are for example upgraded or moved, the simulations have to be re-analysed for the new setup or configuration.

There are limitations to the simulations. They require a large amount of storage space. Ideally, every angle in elevation and azimuth, energy and atmospheric condition, as well as telescope setup, would be modelled multiple times to give differently shaped shower images that can be averaged over. This is, however, not reasonable. The energy steps are not infinitesimally small because they do not need to be, they just need to be smaller than the energy and angular resolution of the telescope(s) at the given energy. The simulations for VERITAS and Eventdisplay will be taken up in detail in Sec. 4.1.

Depending on the method used, data collected by telescopes, e.g. the incoming angle, shower image shape and intensity are compared with simulations to get the energy of the incoming particle. Look-up tables, image comparison and intricate calculations are all used in different methods to get the energies of the incoming particle.

2.8.1 Hillas Analysis

The main way to analyse showers within the VERITAS collaboration is using Hillas analysis. Five parameters are acquired when using Hillas analysis to characterise Cherenkov showers. In Hillas analysis, an ellipse is fitted to the shower image. Here, two parameters are calculated, the width and length of the ellipse.
The *width* is the root mean squared, RMS, angular size along the minor axis of the ellipse and is related to the lateral development of the shower.
The *length* is the RMS angular size along the major axis of the ellipse and related to the longitudinal development of the shower.
This parameter gives a measure of the parallax angle to the shower maximum, i.e. where the shower produces the most Cherenkov photons, and grows with increasing impact parameter.
The Hillas parameters can be calculated from the image of one telescope. Adding more telescopes allows for a stereo-reconstruction of the shower, which will improve the calculated results. The distance from the shower and the shower direction can also be more accurately calculated. Using trigonometry, the long axis of each image will give a point location on the ground. Adding all the images from each telescope into one image will give a point in the sky. Using the locations on the ground and in the sky, a direction of propagation and a shower origin, where the first particle interacted with the atmosphere, can be calculated. A representation of this can be seen in Fig. 2.13, and the Hillas parameters can be seen in Fig. 2.14.

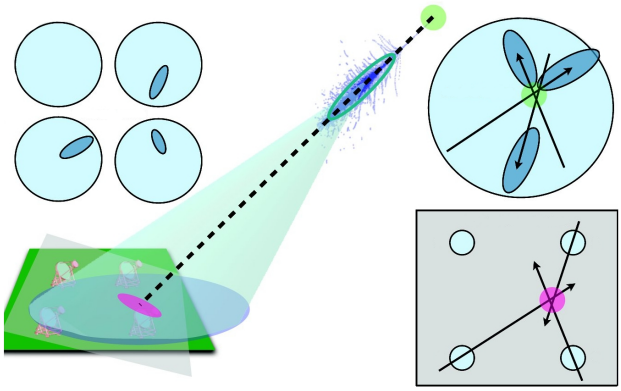

Figure 2.13: Three of four telescopes detect a shower and locate the incoming direction and the shower height. The figure is taken from "kosack isapp lecture 2" at the 2013 Paris ISAPP summer school.

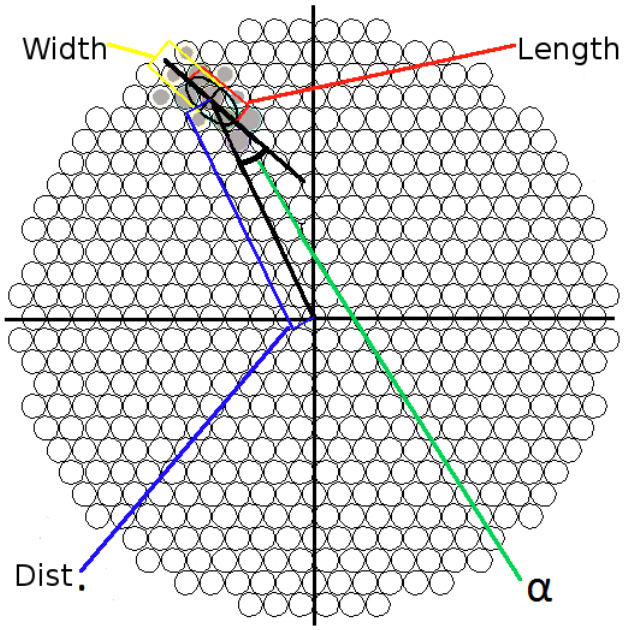

Figure 2.14: Hillas parameters related to the shower image.

For analysis using multiple telescopes, weighted combinations of the width and length parameters can be used. A favoured method is to calculate the mean-scaled-parameters, i.e. the mean-scaled-width, MSW, and mean-scaled-length, MSL, from the Hillas parameters of the individual telescopes:

$$\mathrm{MSP} = \frac{1}{N_{\mathrm{tel}}} \sum_{i=1}^{N_{\mathrm{tel}}} \frac{p^i}{\langle p^i_{\mathrm{sim}}\left(\theta, \mathrm{size}, r\right)\rangle}, \tag{2.17}$$

where p^i is the parameter (either width or length) for telescope i and p^i_{sim} (θ, size, r) is the mean value of that parameter from simulations for a given image shower size, zenith angle θ and impact distance r.
The angle, α, made between the major axis of the ellipse and the line between the source position and image centroid, is the third parameter. Showers that originate from an object at the source position should have a value of α very close to zero. For an array of telescopes, θ^2 is used rather than α. θ^2 is the square of the distance between the intersection point of the major axes of images in all pairs of telescopes and the source position.

The fourth parameter, I, is the intensity of the gathered photons within the ellipse.

The fifth parameter is the distance, D, from the centre of the field of view of the camera, which is normally the centre of the camera, to the centre of gravity of the shower image. This is equivalent to the angle between the line from the shower maximum to the telescope and the shower axis. This can be seen in Fig. 2.14.

Important to note is that it is the image of the shower that is being parametrised with Hillas analysis. This is different from the analysis method that is being used during this thesis, 3D-model analysis.

2.8.2 3D-model

The 3D-model analysis method parametrises the shower directly.

The method was developed by M. Lemoine-Goumard et. al and published in 2006, [47]. Much in this section will follow their work and any unreferenced equation in this section is from their work.

The 3D-model uses eight parameters instead of the five that are in Hillas analysis. Some of the 3D-model parameters can be seen in Fig. 2.15:

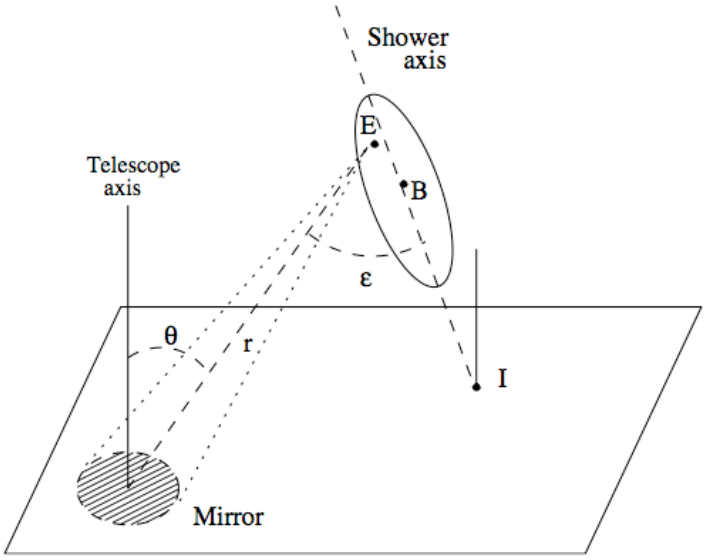

Figure 2.15: I is the centre of where the shower hits the ground. B is the barycentre of the shower core. E is the emission point of a photon in the shower. r is the distance between the telescope centre and E. θ is the angle between the incoming photon direction and the telescope pointing direction. ϵ is the angle between the shower direction and the photon direction. The figure is taken from [47].

Most of the parameters in the 3D-model are analogous to the parameters of Hillas analysis and can even be calculated back and forth if a direct comparison is wanted.

The shower core position on the ground, X_0 and Y_0, together with the polar angles of the shower axis, θ_0 and φ_0 are self-explanatory, as is the height, h, of the shower core along the shower axis. The shower core is where the Cherenkov showers produce the highest number of Cherenkov photons.

The three remaining 3D-model parameters are not self-explanatory.
The most important characteristic of electromagnetic showers is that the distributions of secondary particles are, on average, rotationally symmetric with respect to the shower axis. The 3D-model of gamma-ray showers is based on the two following simplifying assumptions.
The first simplification is that the emission points of Cherenkov photons are rotational symmetric around the shower axis and distributed according to a three-dimensional Gaussian law. Particle shower simulations of the number of electrons generated in the shower have been created and fitted with a Gaussian and is in good agreement with upto an altitude of about 12 km, thus justifying the assumption. Fig. 2.16 depicts this fit, [47].

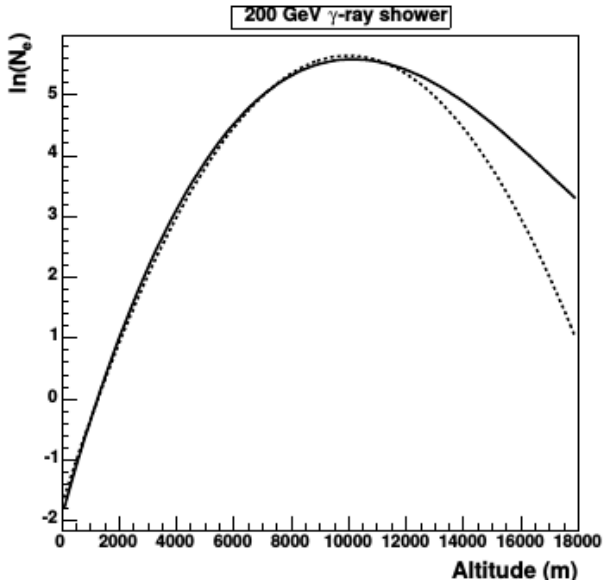

Figure 2.16: Figure shows how well a shower from 200 GeV photons follows a Gaussian shape at different altitudes. N_e is the logarithm of the number of generated electrons and positrons. The solid line is the simulation and the dotted line is the approximation. The figure is taken from [47].

The second simplification is that the angular distribution of Cherenkov photons, in relation to the shower axis, is independent of the position of the emission point and of the energy of the primary gamma-ray. This is not intuitive, but simulations show that, except for times very early on in the shower development, this is an acceptable simplification considering the resolution of today's telescopes, [47]. This is depicted in the following figure from [47].

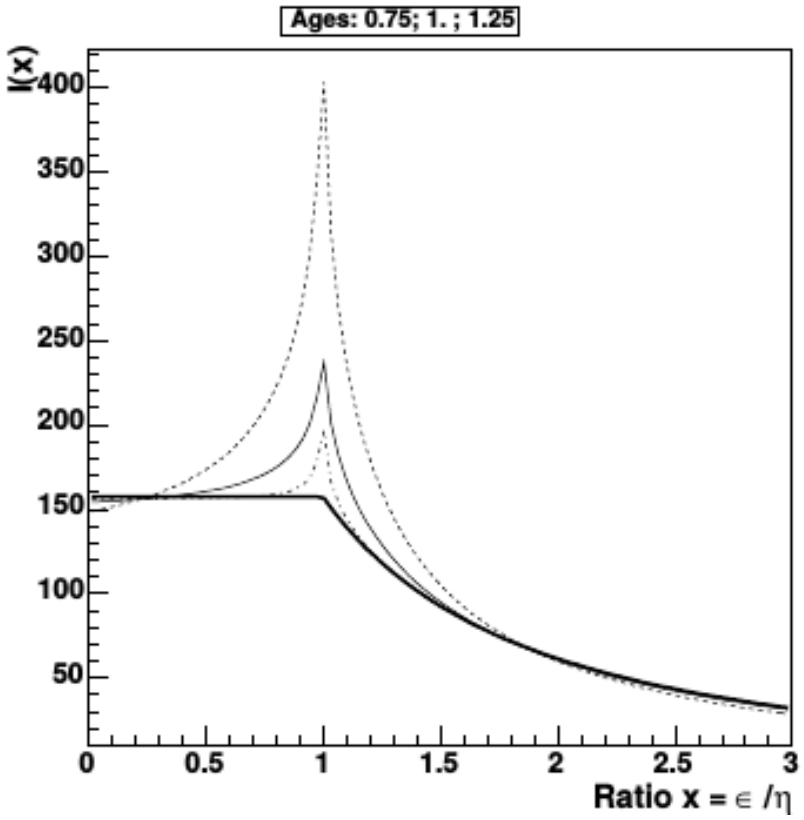

Figure 2.17: Probability distributions for a shower in the 0.5 - 1 TeV energy range for ages of 0.75, 1.0 and 1.25. Ages are different points in time in the simulations done in [47]. The probability is given for the emission per unit solid angle of Cherenkov photons as a function of the angle ϵ with respect to the shower axis. The abscissa is the ratio $x = \frac{\epsilon}{\eta}$, where μ is the maximal Cherenkov angle at the altitude considered. The figure is taken from [47].

In Fig. 2.17, the graph of the function $I(\epsilon)$ used in the reconstruction procedure is shown by the bold line. This line follows:

$$\begin{aligned} I(\epsilon) &= K \text{ if } \epsilon < \eta \\ \text{and } I(\epsilon) &= K\frac{\eta}{\epsilon}\left[-\frac{\epsilon-\eta}{4\eta}\right] \text{ if } \epsilon > \eta. \end{aligned} \tag{2.18}$$

With the simplifications, the distribution of the emission points of Cherenkov photons can be described by a three-dimensional Gaussian law with rotational symmetry around the shower axis. From this three-dimensional Gaussian, the longitudinal and two-fold degenerate transverse standard deviations, σ_L and σ_T respectively, are two of the three left over parameters. These two are also known as the $3D - Length$ and $3D - Width$.
A so-called "reduced" version of the σ_T parameter can be determined by multiplying it with the density of air at the altitude of the shower core, $z_{\max}$, where the shower produces the maximum amount of Cherenkov photons. This makes σ_T more or less independent of elevation and energy. This makes it excellent for gamma/hadron separation, because it can be used as an efficient cut for all elevations and energies.

$$\sigma_T' = \sigma_T \phi(z_{\max}), \tag{2.19}$$

with $\phi(z_{\max})$ being the elevation angle to $z_{\max}$. The final parameter is the total estimated number of Cherenkov photons emitted by the shower, N_c. In order to get that, each individual pixel's expected number of Cherenkov photons is needed. The expected Cherenkov photon amount in each pixel is q_{th} and can be described by:

$$q_{th} = \int_0^\infty n_C(r) r^2 dr \Delta\omega_{\text{pix}} I(\varepsilon) \frac{A_{\text{tel}} \cos\Theta}{r^2} = A_{\text{tel}} \Delta\omega_{\text{pix}} I(\varepsilon) \cos\Theta \int_0^\infty n_C(r) dr. \tag{2.20}$$

Some of the parameters from Eq. 2.20, I, r, ϵ and θ, are shown in Fig. 2.15. The angle ω_{pix} is the opening angle of a pixel and A_{tel} is the area of the telescope. Important to note is that $I(\varepsilon)\frac{A_{\text{tel}}\cos\theta}{r^2}$ is the fraction of photons from the emission point, E, reaching the mirror. As can be seen, the Cherenkov photon density, n_c, is integrated along the line-of-sight from the point of view of a pixel. This can be expressed as:

$$n_C(r) = \frac{N_C}{(2\pi)^{\frac{3}{2}}\sigma_L\sigma_T^2} \exp\left(-\frac{M}{2}\right), \tag{2.21}$$

where N_C is the total number of emitted Cherenkov photons, and M stands for the mathematical expression:

$$M = \frac{\xi^2}{\sigma_L^2} + \frac{\eta^2}{\sigma_T^2}, \tag{2.22}$$

with

$$\begin{gathered} \xi = (r\overrightarrow{p} - \overrightarrow{x}_B) \cdot \overrightarrow{s} = r\cos\varepsilon - \overrightarrow{x}_B \cdot \overrightarrow{s} \\ \text{and} \\ \eta^2 = (r\overrightarrow{p} - \overrightarrow{x}_B)^2 - (r\cos\varepsilon - \overrightarrow{x}_B \cdot \overrightarrow{s})^2. \end{gathered} \tag{2.23}$$

In the previous two equations, $\overrightarrow{x}_B = \overrightarrow{OB}$ is the vector defined by the telescopes optical centre, O, and the shower core, B. $\overrightarrow{p}$ and $\overrightarrow{s}$ are the unit vectors along the line-of-sight and the shower axis respectively.
Still following [47], the following definitions are independent of r:

$$\begin{gathered} B_s = \overrightarrow{x}_B \cdot \overrightarrow{s}, \\ B_p = \overrightarrow{x}_B \cdot \overrightarrow{p}, \\ u = \cos\varepsilon, \\ \Delta_B^2 = \overrightarrow{x}_B^2 - B_p^2, \\ \sigma_u^2 = \sigma_T^2 u^2 + \sigma_L^2(1-u^2) = \sigma_T^2\cos^2\varepsilon + \sigma_L^2\sin^2\varepsilon, \\ \text{and} \\ \sigma_D^2 = \sigma_L^2 - \sigma_T^2. \end{gathered} \tag{2.24}$$

Due to the stated independence, it is possible to get the total number of expected Cherenkov photons, N_c, by knowing σ_T, σ_L, $\overrightarrow{s}$, $\overrightarrow{x_B}$, which are determined by analysing observations and n_c, the number of expected Cherenkov photons in a pixel, which is taken from shower simulations.
The second-degree polynomial M in r, can be written as:

$$M = \frac{\sigma_u^2}{\sigma_L^2\sigma_T^2}\left[r - \frac{\sigma_L^2 B_p - uB_s\sigma_D^2}{\sigma_u^2}\right]^2 + R, \tag{2.25}$$

where

$$R = \frac{1}{\sigma_L^2\sigma_T^2}\left[\Delta_B^2\sigma_u^2 - \sigma_D^2(uB_p - B_s)^2\right], \tag{2.26}$$

which is also independent of r. Putting this into Eq. 2.21, n_c thus becomes:

$$n_C(r) = \frac{N_C \exp(-\frac{R}{2})}{(2\pi)^{\frac{3}{2}}\sigma_L\sigma_T^2} \exp\left\{-\frac{\sigma_u^2}{2\pi\sigma_L^2\sigma_T^2}\left[r - \frac{\sigma_L^2 B_p - uB_s\sigma_D^2}{\sigma_u^2}\right]^2\right\} \quad (2.27)$$

and the integral from Eq. 2.20 becomes:

$$\int_0^\infty n_C(r)dr = \frac{N_C C}{2\pi\sigma_u\sigma_T} \exp\left\{-\frac{1}{2}\left[\frac{\Delta_B^2}{\sigma_T^2} - \frac{\sigma_D^2}{\sigma_T^2\sigma_u^2}(uB_p - B_s)^2\right]\right\}, \quad (2.28)$$

where

$$C = 1 - \text{freq}\left(-\frac{\sigma_L^2 B_p - \sigma_D^2 uB_s}{\sigma_u\sigma_T\sigma_L}\right). \quad (2.29)$$

For this, the function, freq(x) is defined the following way:

$$\text{freq}(x) = \frac{1}{\sqrt{2\pi}}\int_{-\infty}^{x} \exp(-\frac{t^2}{2})dt. \quad (2.30)$$

Solving Eq. 2.27 for N_C gives:

$$N_C = \frac{n_C(r)(2\pi)^{\frac{3}{2}}\sigma_L\sigma_T^2}{\exp(-\frac{R}{2})\exp\left\{-\frac{\sigma_u^2}{2\pi\sigma_L^2\sigma_T^2}\left[r - \frac{\sigma_L^2 B_p - uB_s\sigma_D^2}{\sigma_u^2}\right]^2\right\}} \quad (2.31)$$

2.8.3 3D-energy

In standard Hillas analysis look-up tables are used to "look up" the energies of the showers being analysed. The look-up tables are generated by analysing simulations using Hillas analysis. In this thesis, the 3D-energy, which is the 3D-model shower energy, is found in *reference files*. The reference files are also a form of look-up tables. The change of name is there in order to differentiate them from the look-up tables of Hillas analysis in Eventdisplay.
In the reference files, averages have been calculated for which a general energy is close enough to each slightly varying shower. For each set of averaged simulation showers, all the shower parameters are known as well the energy. Each reference file contains a large list of *reference sets*. A reference set is a set of all 8 3D-model parameters. Creating large, well-spaced reference files with reference sets results in that an average energy, that should be close to the real energy, can be acquired when real data is analysed.

To find the set of parameters that best represents a shower in a list of sets, it is possible to minimise over the parameters. The minimisation equation used for the 3D-model parameters in this thesis is the following:

$$B_{\min} = min_{x \in S} \frac{1}{N} \sum_{1}^{N} |D_n - R_n|, \tag{2.32}$$

where $B_{\min}$ is smallest difference between data and reference sets and decides the reference set that is chosen. S is the set of all the values tested, D_{n} and R_{n} are the values from the data and the reference sets respectively for all the N parameters. The minimisation works because all the 3D-model parameter differences are on the same scale.

Since the best fit is seldom exactly correct, the 3D-energy acquired needs to either be scaled or interpolate between values to get the right 3D-energy. The 3D-model parameters are linear, which makes a simple linear scaling of the energy possible. Scaling the energy according to each parameter individually and then averaging that the result is adequate. However, interpolation is a better way to get a more correct energy. The equation for the interpolation used is the following:

$$E_{3D} = \frac{1}{N} \sum_{1}^{N} \left(E_{Ln} + E_{Hn} \frac{D_{Hn} - D_{Ln}}{D_{Hn}} \right), \tag{2.33}$$

where E_{3D} is the final 3D-energy. E_{Ln} is the lower 3D-energy acquired for the n'th data parameter D_{Ln}, E_{Hn} and D_{Hn} are the equivalent for the higher 3D-energy. N is the number of 3D-model parameters used.

2.8.4 Bias Correction

Even after the 3D-energy is found with the more robust method, the 3D-energy can still be biased. The bias comes from, among others reasons, systematics in the method. Knowing the actual values of the showers from simulations, and seeing what 3D-energies a 3D-model analysis of the simulations results in, it is possible to calculate the average discrepancy and apply corrections to real analysis based on that. This leads to a less biased result on average. In practise, this is done by applying corrections to the energy. For the 3D-energy a Landau correction below 0.5 TeV, and two second-degree polynomial corrections, one from 0.5-5 TeV and one above 5 TeV is used. Note that

the Landau correction curve is centred below 0, meaning that the correction only comes from the steep slope where the effective area drops off. In this low-energy-range, the energy is almost always overestimated due to the reason mentioned above as well as a drop in effective area. The Landau function in Eventdisplay is approximated as follows:

$$f(z) = a_0 \frac{1}{\sqrt{2\pi}} \exp\left(-\frac{z + \exp(-z)}{2}\right), \tag{2.34}$$

where $z = \frac{x-a_1}{a_2}$, with a_i being variables. The second degree polynomials used are of the form:

$$f(x) = b_1 + b_2 x + b_3 x^2, \tag{2.35}$$

where b_i are variables.

2.8.5 Line Search Concept

The idea of the line search for this thesis is based on what has been done in [72]. The concept of a sliding energy window approach is that each time the window is moved one energy bin, a fit to find a line is done. The best fit probability shows the location of the most likely line energy and its significance.

In [72], a sliding energy window is used to do a likelihood search for a DM line. The window width is a few times the energy resolution of the Fermi-LAT telescope. The likelihood search in the paper was done by maximising the Poissonian probability function to the number of expected photons to collected photons:

$$\prod_i P(s_i|\nu_i) \equiv \prod_i \frac{\nu_i^{s_i} e^{-\nu_i}}{s_i!}, \tag{2.36}$$

where s_i and ν_i are the measured and expected number of photons respectively for the i'th energy bin. Each bin window is centred on the assumed DM particle mass.

The same is done in this thesis, obviously using the energy resolution of VERITAS, instead of Fermi-LAT. Instead of fitting a perfect line with the delta function $S_L\delta(E - E_\gamma)$, as is done in [72], a Gaussian line profile is used in this thesis because the line is smeared out due to limited resolution and statistical fluctuations, making the total equation fitted:

$$\frac{dN_\gamma}{dE} = S_B \frac{E}{E_\gamma}^{-\Gamma} + S_L \exp\left(-\frac{(E - E_\gamma)^2}{2\sigma^2}\right), \tag{2.37}$$

where $\frac{dN_\gamma}{dE}$ is the γ-ray flux per energy, σ is the energy resolution at the DM mass, E_γ. S_B is the strength of the background, Γ is the slope of the background and S_L is the strength of the DM line signal. The strength of the DM line signal must be ≥ 0, since a negative excess makes no physical sense. In this thesis, ROOT MINUIT, which is a Chi-squared minimisation technique, is used to fit the data with Eq. 2.37. For the search done in this thesis, the on- and off-region are fitted simultaneously with the power law part of Eq. 2.37 to get the likelihood for the case where there is no signal, $\mathcal{L}_{\text{null}}$, this represents the Null hypothesis. The full version of Eq. 2.37 is then used to get the likelihood in the case of an assumed signal, $\mathcal{L}_{\text{line}}$, this represents the alternative hypothesis.
The Test Statistic, TS, of any found line is then defined as:

$$TS \equiv -2 \ln \frac{\mathcal{L}_{\text{null}}}{\mathcal{L}_{\text{line}}} \tag{2.38}$$

with the significance defined as $\sqrt{TS}$, in accordance with Wilks' theorem [73]. With enough tested DM masses, also known as trials, it is likely to find a line that is just a fluctuation in the signal flux, not an actual line signal. Thus, a trials factor needs to be calculated and used to correct for this effect.

2.8.6 Trials Factor and Significance Correction

The trials factor is the ratio between the probability of observing an excess of flux at a specific energy, to the probability of observing the excess anywhere in the energy range. Setting the energy binning of the data being analysed to be below the energy resolution of the analysis method makes the search effectively un-binned. For the sliding energy window approach, the number of bins where a line is searched for, N_{bins}, is set by dividing the energy range searched by the bin-size per energy and then subtracting the number of bins that fits in the sliding window below and above the DM mass at the low edge, W_{DML}, and high edge, W_{DMH}:

$$N_{\text{bins}} = N_{\frac{E_{\text{range}}}{E_{\text{binsize}}}} - N_{\frac{W_{\text{DML}}}{E_{\text{binsize}}}} - N_{\frac{W_{\text{DMH}}}{E_{\text{binsize}}}}. \tag{2.39}$$

N_{bins} is the number of tests for a line that is done in the energy range. It is not uncommon for this value to be used as the trials factor, this would however, overestimate it.

To get the correct trials factor a large number of analysis tests has to be done, see [40]. This is however, computationally intensive. A close approximation of the trials factor, without doing a large number of simulated tests, can be calculated for data that is log-linear over subset intervals. First, the number of independent search regions should be calculated using the following equation:

$$\#_{\text{indep.reg.}} \approx \frac{\log\left(\frac{E_{\text{High}}}{E_{\text{Low}}}\right)}{\log\left(\frac{1+\Delta E}{1-\Delta E}\right)}, \tag{2.40}$$

where E_{Low} and E_{High} are the lower and higher energy edges of the region being analysed. ΔE is the energy resolution.
Second, if the same feature is searched for in multiple targets, all values should be added together to get the full trials factor number. This is not the case if the targets are stacked, in which case the calculated value is the correct trials factor number to use.
To correct the significance value for the number of trials done, the significances has to first be converted into p-values and then solve:

$$1 - P_{True} = (1 - P_{TS})^T, \tag{2.41}$$

where P_{True} is the P-value for the trials corrected significance, P_{TS} is the P-value corresponding to the test statistic, and T is the trials factor. To get the correct line significance the P_{True} has to be converted back into significance.

2.9 Theory Summary

Assuming that ΛCDM is correct, and that WIMPs are the sought after DM particle, the annihilation in dwarf spheroidal galaxies sending out gamma-rays should be detectable with ground-based Cherenkov telescopes via the atmospheric interactions. Improved methods, such as the 3D-model analysis that assumes that Cherenkov shower photon emissions can be approximated with 3D Gaussians, should be better at correctly identifying Cherenkov showers than methods such as Hillas analysis, which is the currently used method within the VERITAS collaboration using the Eventdisplay analysis program. By doing a line search for the "smoking gun" signature of DM in the photon flux/energy regime could make it possible to identify DM.

Chapter 3

Instrumentation

3.1 VERITAS

VERITAS is located on Mt. Hopkins in Arizona, USA. During the lifetime of VERITAS, first light in 1998 and still being used, there have been two major upgrades. It was first changed in September of 2009. At that time, one of the four telescopes that the array consisted of, and still does, was moved to increase the directional reconstruction quality, [54]. The move also made the array more square in appearance. This can be seen in Fig. 3.1 and 3.2 which shows the VERITAS layout before and after the move. The second upgrade was at the end of 2012, when the photo-multipliers were upgraded, [33]. For this thesis, data has been used from before, between and after the upgrades were made. These different periods are called V4, V5 and V6 for array version 4, 5 and 6. Array versions 1, 2 and 3 were for when there was just 1, 2 and 3 telescope(s) on site. Both these upgrades did of course have benefits. The 2009 change gave a 30% improvement in the sensitivity and thus also reducing the time to detect a source by 60%. The upgrade in 2012 lowered the energy threshold of the array. The following table shows the specifications of the current VERITAS version, V6.

Table 3.1: List of the specifications of VERITAS

Parameters	Values
Number of telescopes [-]	4
Diameter per telescope [m]	12
Number of pixels per telescope [-]	499
Field of view [deg]	3.5
Resolution [deg]	0.1
Usable energy range [TeV]	∼0.1-30
True energy range [TeV]	∼0.03-50
Energy resolution at 1 TeV [%]	15-20
5 σ detection for 1% Crab [h]	26
Height above sea level [m]	1268
Annual observation time, dark time [h]	∼850
Annual observation time, moderate moon light [h]	∼200
Annual observation time, bright moon light [h]	∼250
Dead time [%]	∼10

VERITAS has three trigger levels; no. 1 at pixel level, no. 2 is a pattern trigger for when three adjacent pixels are triggered and no. 3 is when two or more telescopes are triggered within a set time-frame.
Note that the absolute limits of VERITAS are at approximately 0.030 TeV at the low energy end, and 50 TeV at the high energy end. The practical limits, where maximum sensitivity is reached, are currently at ~ 0.15 and ~ 30 TeV, for low and high energies respectively.
The energy range studied in this thesis is between 0.1-10 TeV. The energy range of highest interest is < 1 TeV, where the DM particle is most likely to be found as described in Sec. 2.2.2.

Figure 3.1: Areal view of telescope placement before the move in September of 2009. The figure is taken from [62].

Figure 3.2: Areal view of telescope placement after the move in September of 2009. The figure is taken from [59].

3.2 CTA

CTA will be, when completed, a set of two Cherenkov telescope arrays that is currently being planned by the CTA collaboration. It will have more telescopes, be able to observe a larger energy range and have a better energy resolution than any current array. This is based on different needs, recommendations and wants of various groups that are, and will be, working with CTA and the different ranges of the electromagnetic spectra that it will be able to observe.
CTA can be compared with VERITAS, as will be done in Chapter 6, to give an idea of what the future will bring.

3.2.1 CTA Requirements

In order to get to new exciting physics, CTA needs to be at least as powerful as the current generation of Cherenkov telescope arrays. A general goal has been set for CTA, which is to be at least one order of magnitude more powerful than the current generation.

The CTA will cover four orders of magnitude in energy, from a few tens of GeV to a few hundreds of TeV. This in itself is enough to do comprehensive studies of the physical processes that go on in many types of sources such as AGNs and supernovae. Together with other instruments, such as Fermi, this can be extended another three orders of magnitudes lower.

The aim is to make CTA approximately a factor of 10 more sensitive than any existing instrument. In the mid-energy range, from approximately 100 GeV to several TeV, CTA aims to reach a factor of 10^3 below the flux of any currently known steady source of very high energy gamma-rays, at 1-2% Crab. At the time when the CTA requirement documents were written in 2010 the source was PG1553+113, [6]. CTA also aims to reach a factor of 10^4 below the highest measured burst fluxes [67]. This leads to the possibility of deeper studies of known sources and will likely lead to the discovery of new phenomena.

In terms of angular resolving power, the goal for CTA is to reach a few arc-minutes resolution. This is approximately 5 times finer than VERITAS' 0.1 degrees. This should be achievable by choosing subsets of simultaneously detected gamma-ray events.

CTA aims to be able to resolve time variable emissions down to sub-minute time scales. This will be very important for AGNs and pulsars.

CTA also aims to cover the entire sky.

Even though it is not a strictly technical target goal of the CTA, as the higher resolution is, the CTA collaboration strives to make it flexible. This will be achieved by making subsets of arrays or telescopes individually controllable. This allows for individual sky patches to be observed, increasing the sky coverage, or increasing sensitivity in one or a few sky patches. The aim is to have full sky coverage with many detailed patches.

3.2.2 Two Locations:

To cover the entire sky, there will be two CTA sites, [5]. One site in the northern hemisphere and one site in the southern hemisphere, with various types of telescopes. CTA North will have around 30 telescopes. This site will focus on Active Galactic Nuclei, *AGN*, cosmological galaxies, star formation and stellar evolution. CTA South is the primary CTA site, which will consist of around 100 telescopes. This site will focus on the central region of our Galaxy.

The specific sites have finally been chosen during the very end of this thesis. The sites selected, with backup sites, can be seen in the following Fig. 3.3.

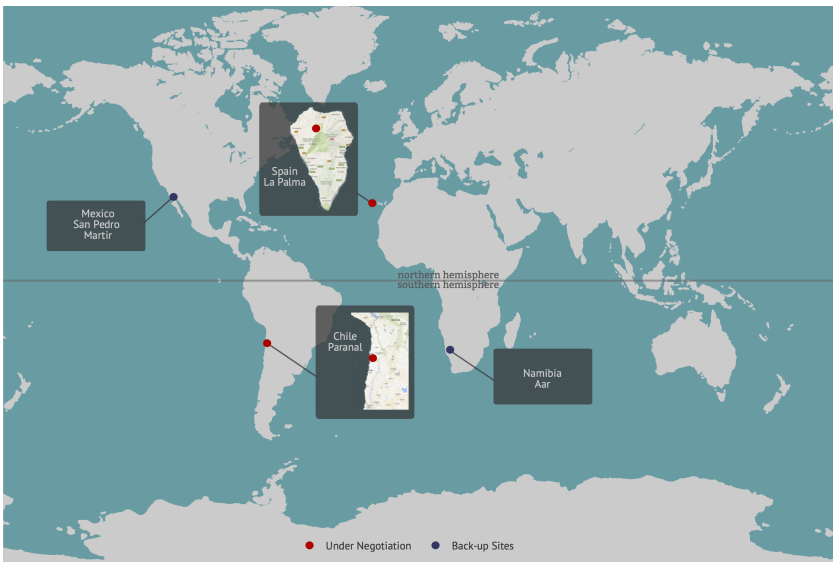

Figure 3.3: The two CTA sites. The figure is taken from the CTA press release, 26/04/2015.

3.2.3 Three Sizes of Telescopes:

CTA will consist of three sizes of telescopes, the Small Size Telescopes, $SSTs$, the Medium Size Telescopes, $MSTs$, and the Large Size Telescopes, $LSTs$, [5]. It is likely that only the southern site will have the SSTs.

SSTs:
There will likely be several types of SSTs, and thus only the general concepts will be taken up here. The SSTs will be in the 6-8 m diameter class.
The CTA SSTs domain is above a few TeV, the highest energies reachable by the CTA. In this energy range, the array needs to cover many square kilometres in order to get a high enough number of γ-rays. At these energies, the light yield from the Cherenkov shower is high and the possible detection radius is beyond the normal $\sim$100 m radius light pool.
Depending on the size of the SSTs, the number that will be implemented, and spacing of these, can vary. There will either be a larger number of telescopes with smaller mirror areas and spacing matched to the size of the light pool of 100 to 200 m, or a smaller number of telescopes with larger mirror areas and spacing of up to 500 m. A third alternative is to cluster the SSTs in a few sub-clusters. Of course, there can be a mix of the aforementioned alternatives. The decision has little consequence for the DM search at lower energies unless it affects the number of LSTs and MSTs that will be built.

MSTs:
The CTA MSTs will be built to achieve milli-Crab sensitivity in the energy range from approximately 100 GeV to a few TeV. This makes the MSTs of great interest for DM searches and because of the overlap with the energy range of VERITAS, a comparison can be made between the two arrays. The MSTs energy range overlap at the high end with the SSTs, and at the low energy end with the LSTs.
Shower detection and reconstruction in this energy range are well known from current instruments, such as VERITAS, and the current concept is to place the telescopes in a grid. The telescopes will be in the 10 to 15 m class, with spacing in the 100 m range. Improved sensitivity is obtained by the increased area covered, by the higher quality of shower reconstruction and a larger number of telescopes than for current few-telescope arrays.
One important aspect of the CTA is that, for the first time, the array sizes will be larger than the Cherenkov light pool. With the stated spacing, images will

be sampled uniformly across the light pool. A number of images will, most of the time, be recorded close to the optimum distance from the shower axis, from 70 to 150 m. At this distance, the light intensity is large and intensity fluctuations are small. Images will also be recorded where the shower axis is at a sufficiently large angle for efficient directional reconstruction.
Compared to current arrays, the event trigger threshold can be pushed down due to the relatively dense spacing and the large area of the telescopes. A telescope pair or group sufficiently close to the shower core can always be found.

LSTs:
The CTA LSTs are focused on the CTAs lowest energy region, from a few tens of GeV up to approximately 100 GeV. Just as with the MSTs, the energy range overlap with VERITAS, means that a comparison can be made.
At the opposite end of the size range with respect to the SSTs, there will only be up to 4 LSTs at each CTA site, see [5] and [4]. To detect showers down to a few tens of GeV, the detectors need to be able to sample and detect the Cherenkov light efficiently. Assuming standard photomultiplier tubes, the LSTs need to be covered by approximately 10% of a shower to be able to detect it. High event rates and systematic background uncertainties will likely limit the sensitivity that can be achieved. The total ground area covered by the LSTs can be comparatively small, just a few times 10^4 m^2, due to the small shower light pools at these energies.
The diameter will be around 24 m for the LSTs and they will be placed approximately 100 m away from each other.

The following table has the general specifications for the three types of telescopes that the CTA will consist of.

Table 3.2: Specifications for the Southern/Northern CTA sites.

Parameters	SST	MST	LST
No. of Pixels [-]	∼1296-2048	1600	1000
Diameter [m]	4-4.3	10-15	24
Resolution [deg]	0.25	0.18	0.09
Field of view [deg]	∼9.1-9.6	8	5
No. of Telescopes	70/0	25/15	4/4
Energy range [TeV]	1-300	0.1-1	0.02-0.5

A rendering of the CTA South site with all three telescope sizes can be seen below in Fig. 3.4.

Figure 3.4: A rendering of the CTA array with all three telescope sizes. The figure is taken from [35].

3.3 Fermi-LAT

Unlike CTA and VERITAS, both being ground based telescope arrays, Fermi is a satellite outside the Earth's atmosphere. The Large Area Telescope, *LAT*, is the main instrument on the Fermi Gamma-ray Space Telescope spacecraft. The spacecraft was launched on the 11th of June 2008 and was designed to run for 5 years, but is now striving for 10 years. Also unlike CTA and VERITAS, Fermi-LAT is not a Cherenkov telescope array with sizeable mirrors and pixel cameras. Gamma-rays pass through the LATs thin plastic anticoincidence detector, unlike charged cosmic rays which interact and cause a flash of light. Gamma-rays continue until they interact with atoms in one of the thin tungsten foils where pairs of electrons and positrons are created, one pair per gamma-ray. The pairs then create ions in thin silicon strip detectors where the directions are tracked. Finally, the particles are stopped in the cesium iodide calorimeter, and the total energy is measured. Thus, the energy

and direction of the gamma-rays are known.
The reason to bring up the Fermi-LAT in this thesis is because of the claims of DM line detection(s) made by independent groups, [71]. The line search method used in this thesis following what was done in that work, with a few important modifications. The importance lies in the overlap in the energy ranges, which will be discussed in Sec. 3.4. The following table shows the specification of the Fermi-LAT.

Table 3.3: Short list of the specifications of Fermi-LAT

Parameters	Values
Energy range [GeV]	0.03 - 300
Field of view [deg]	137.5 (at 1 GeV)
Resolution [deg]	3 (at 100 MeV) - 0.04 (at 100 GeV)

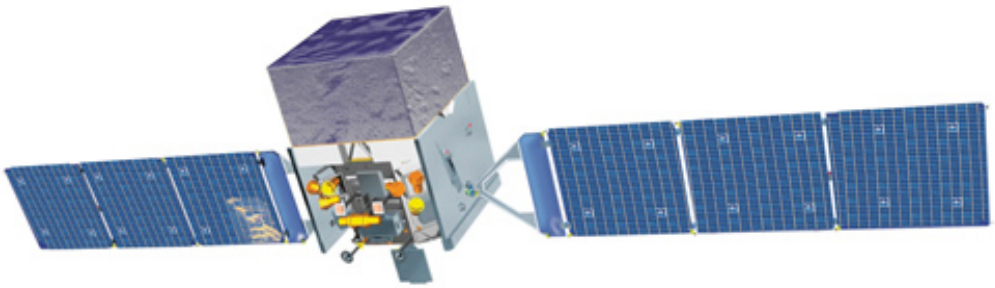

Figure 3.5: A rendering of Fermi-LAT. The figure is taken from [52].

3.4 VERITAS, CTA, and Fermi Comparison

As already stated, there are naturally many overlapping regions between the different telescopes taken up in this thesis. CTA will completely overshadow VERITAS. The energy range is going to be wider, both having a lower energy threshold, going higher in the energy range and having a finer energy resolution. The angular resolution will be higher, and it will have a wider field of view. CTA is the next big thing, both literally and figuratively, in gamma-ray astronomy.
The higher energy end of the Fermi-LAT overlaps with the lower end of

VERITAS and CTA, although the overlap with CTA will be greater. The overlapping region is approximately between 100 and 300 GeV.
Comparing the specification between the Fermi-LAT, VERITAS and CTA is not a straightforward task. Since there is a calorimeter and not a pixel camera on the Fermi-LAT, thus there is no pixel-count. There is no mirror, thus no mirror diameter to compare with. The time it takes to detect a flux of 5% Crab is not relevant for this type of detector. However, the capabilities of the three instruments can be compared.

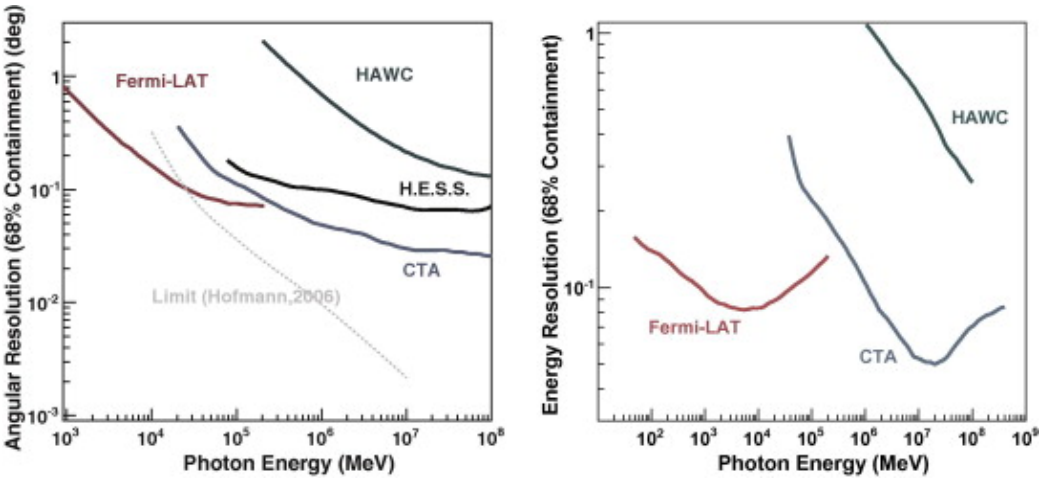

Figure 3.6: The left figure shows angular resolution vs. energy. The right figure shows energy resolution vs. energy. H.E.S.S is comparable to VERITAS. The figures were taken from [38].

As can be seen in Fig. 3.6, CTA outperforms the other ground based arrays by a factor of a few in angular resolution and a factor of ~ 10 in energy resolution. CTA overlaps well with Fermi-LAT, more or less continuing the trend in angular resolution.

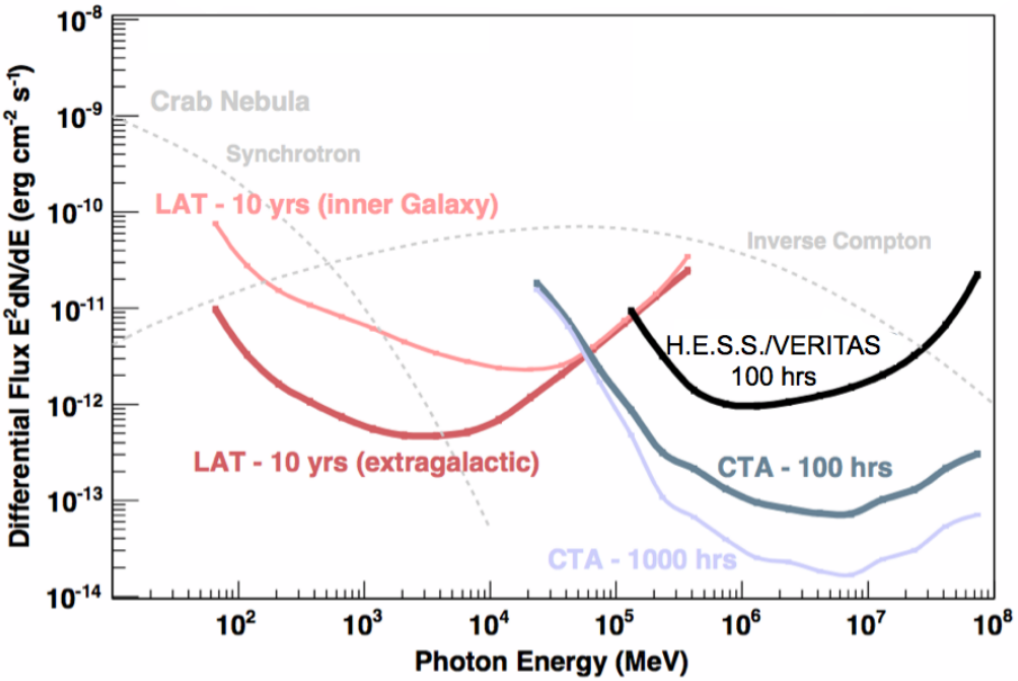

Figure 3.7: Multiple different telescope arrays and Fermi-LAT flux vs. energy comparison. The figure is taken from [38].

As can be seen in Fig. 3.7, the photon flux sensitivity of CTA out-preforms VERITAS at all energies, being between one and two orders of magnitude better. CTA also extends further down by approximately an order of magnitude in energy. Although not shown in Fig. 3.7, the energy range of CTA extends by more than one order of magnitude higher than VERITAS. The overlap is approximately half an order of magnitude between VERITAS and Fermi-LAT. The overlap is greater between CTA and Fermi-LAT.

3.5 Instrumentation Summary

The two current telescopes discussed in this Chapter, VERITAS and Fermi-LAT, are both capable telescopes within their own energy ranges. However, they might not be powerful enough to detect DM within a reasonable timespan. The next generation of telescopes, such as CTA, should significantly improve the chances of detecting DM since it is in most respects one order of magnitude more powerful than VERITAS and a significant overlap with Fermi-LAT.

Chapter 4

Method

There are several steps that needs to be done before being able to analyse the collected data and do a DM line search using the 3D-model with 3D-energy. This is what will be discussed in this chapter, as well as the analysis itself.

4.1 Simulations

As a baseline to compare the collected data against, shower simulations are created. Within the VERITAS collaboration, that uses Eventdisplay, CARE and GrISU simulation packages are used to simulate the telescope response from the output of shower simulation made with CORSIKA, [42].
CARE is the newer of the two simulation packages and is still in the testing phase, thus not all telescope and weather configurations have been simulated and analysed using CARE. As a consequence of this, it has not been officially released yet. For this thesis, CARE simulations has only been used to see what possible benefits the new software package will have on the data analysis results. The availability of simulations used for the 3D-energy was:

Table 4.1: Available simulations

	V4 21	V4 22	V5 21	V5 22	V6 21	V6 22
GrISU	Yes	Yes	Yes	Yes	Yes	Yes
CARE	No	No	No	No	Yes	No

In Tab. 4.1, V4, V5 and V6 are the different telescope configurations. 21 and 22 stands for the simulated winter and summer atmospheres respectively.

The simulations are run at several degree angles away from zenith, so-called zenith angles. The angles are 0, 20, 30, 35, 40, 45, 50, 55, 60 and 65 degrees away from zenith. The simulated telescopes are then rotated azimuthally, about the zenith axis, to get the azimuth differences in steps of one degree. For each shower that is simulated, all the useful information about the showers are stored including the incoming angle, the height of the shower core, the location where the created Cherenkov shower core hits the ground, and the energy of the primary photon. The 3D-model analysis was created as a revision control system, *svn*, branch of Eventdisplay. This branch characterises the shower but does not output any energy result. That means it is similar to the standard Eventdisplay Hillas analysis up to the point before the mean scaled width stage, where the mean scaled widths are calculated and the energy is looked up. The simulations are analysed using the 3D-model analysis. This step outputs all the parameters of the shower, plus the 3D-model parameters, σ_L, σ_T, *source elevation*, *source azimuth*, *reduced width*, *depth* and *source maximum*. Not all the 3D-model parameters are directly needed. The azimuth shows little to no correlation with the energy of the incoming particle, since the energy of the incoming particle is not connected to the direction the telescope is pointing, and can thus be ignored. The *depth* and *source maximum* are strongly correlated with each other, since both are strongly dependent on the incoming particle energy, the atmospheric density profile and the incoming angle of the primary particle. Thus the 3D-model is left with six useful parameters after choosing either *depth* or *source maximum*.

On top of the telescope configurations, weather and elevations, come noise levels. Noise is introduced when analysing shower simulations to simulate the real background noise that occurs in reality. Different levels of noise can be introduced. These are not the same when analysing CARE and GrISU simulations. For the CARE simulations, the levels are; 50, 80, 120, 170, 230, 290, 370 and 450. For the GrISU simulations, the levels are; 75, 100, 150, 200, 250, 325, 425, 550, 750 and 1000. The numbers refer to night sky background flux, i.e. photoelectrons per nanosecond per square meter per steradian.

4.2 Reference File Creation and Testing

In order to make the reference files versatile and fast, not all the simulated showers were kept. Only values with uncertainties of less than 10%, were kept. 10% was chosen because it still left a large amount of useful data and large flexibility for later analysis. The cut on 10% in uncertainty did not introduce any new biases. The next step in the minimisation of the reference sets was to create weighted averages of close-lying showers. Each multi-dimensional average shower does not overlap with any other in the parameter space. The total reduction in data file size from raw analysed simulation to finished reference set was a factor of ~ 100. The time needed to search a reference set went down approximately linear with the size. The reference sets are set up so that all the parameters of each shower are connected via a reference value. In order to speed up the search, each individual parameter is sorted according to size. When any one parameter has been acquired, going via the reference value, any other parameter belonging to the shower can be quickly acquired. This is much faster than having to search for each parameter individually. Once a reference set has been created, it must be tested to see how well it can reproduce the correct energy during test analysis. This is done by analysing other simulations using the 3D-model that uses the reference set that is being tested to get the 3D-energy. The requirement on the new set that is being analysed is that it has to be in the same parameter range as the reference set that is being tested. If the analysis reproduces the parameter values well, e.g. less than a few percent bias in energy on average, the reference set functions properly. If however, the output of the second set of analysed simulations recreates the energy of the simulated events poorly, then the reference sets are reprocessed using some other cuts or parameter combinations to discriminate from badly reconstructed events. This continues until the energy is recreated well.

The cuts in the reference sets, to remove the useless values, are optimised for DM targets. The standard analysis equivalent cuts are called "soft cuts", since these are suited for DM targets. The final reference set cut criteria can be seen in the Appendix. B.

4.3 3D-model

The 3D-model is based on the work of M. Lemoine-Goumard, [47]. First, a data/image cleaning is done. After that, a 3D-gaussian is fitted to the data.

4.3.1 Data Cleaning

Just as with other analysis methods that does not study noise, all pixels that does not fulfil the trigger criteria of the telescope system are rejected. These criteria can vary, depending on the type of analysis that is being done. For the analysis done in this thesis, the following criteria needed to be fulfilled for the shower image to be kept:

- A main pixel must have high enough electron volt count to be kept.
- Three adjacent pixels to the main pixel also need to have a high enough count. The adjacent pixels count does not need to be as high as the main pixel to be kept.
- Two or more telescopes must have seen the same shower.
- $> 70 - 80\%$ of the fitted ellipse shape needs to be within the camera image.

What a "high enough count" is in a pixel depends on the noise and season.

After the aforementioned most basic cuts have been done, the more intricate part of the 3D-model begins. The leftover pixels are fitted using Hillas analysis to get a first approximation of the 3D-model parameters. The Hillas analysis that is being done has a reduced number of iterations in comparison to what is being done in the standard analysis. Thus, it is much faster but less precise in the 3D-model. Around this fitted group of pixels, one boundary layer of pixels is added. These added pixels come from the tail of the distribution of the shower image. This extra ring is needed for the improved fitting with the 3D-model. To save computational time, only one layer of pixels is added back to the pixel image. Through testing, it was determined that adding more than one layer was not beneficial enough to the analysis accuracy to justify the huge increase in analysis time. Fig. 4.1 shows the standard analysis image cleaning and the 3D-model image cleaning:

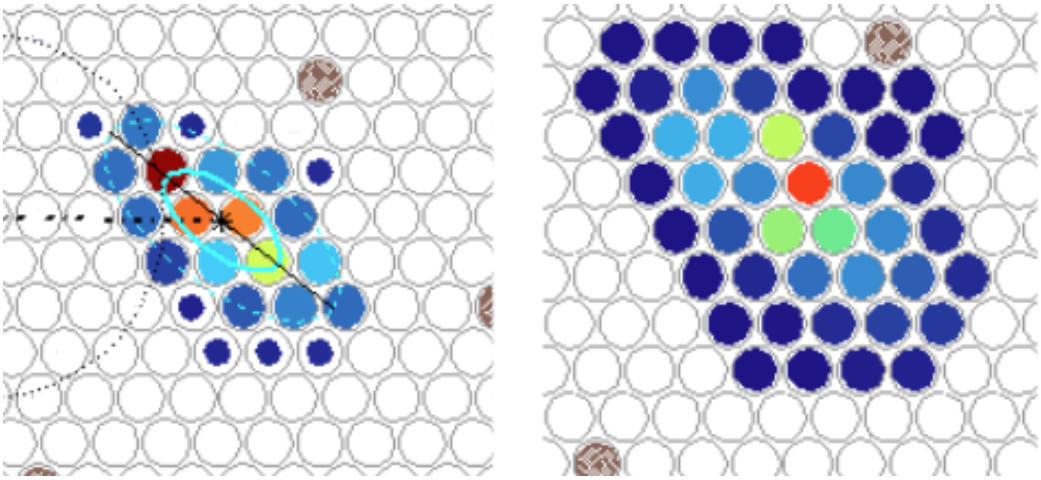

Figure 4.1: The left figure shows a standard analysis shower image after pixel cleaning. From lower too higher electron volt count is described by the colours; blue, green, orange and red. The right figure shows how it looks after the extra layer of pixels have been added back to the image to create a cleaned 3D-model image. The figures are taken from [41].

After the cleaning has been done, the fitting of the 3D-model to the shower can be preformed.

4.3.2 Data Fitting

Two parameters are simultaneously fitted to the shower photoelectrons convolved with the photomultiplier resolution. The parameters are the measured pixel intensity, s, and the 3D-model pixel intensity, μ. This is done via a Levenberg-Marquardt minimisation. The parameters are fitted over a Poissonian probability distribution, P, Eq. 4.1, of the photoelectrons, n, convolved with the photomultiplier resolution, which is approximately Gaussian for larger intensities.

$$P(s|\mu,\sigma_P,\sigma_\gamma) = \sum_n \frac{\mu^n \exp(-\mu)}{n!\sqrt{2\pi(\sigma_P^2 + n\sigma_\gamma^2)}} \exp\left(-\frac{(s-n)^2}{2(\sigma_P^2 + n\sigma_\gamma^2)}\right), \tag{4.1}$$

where the standard deviations in the pixel values and the number of photons are σ_p and σ_γ respectively. The likelihood for each telescope is:

$$\ln L_{\text{tel}} = \sum_{\text{pixel } i} \ln L_i = \sum_{\text{pixel } i} -2 \times P(s_i|\mu_i,\sigma_P,\sigma_\gamma). \tag{4.2}$$

The following figure shows the fitting principal:

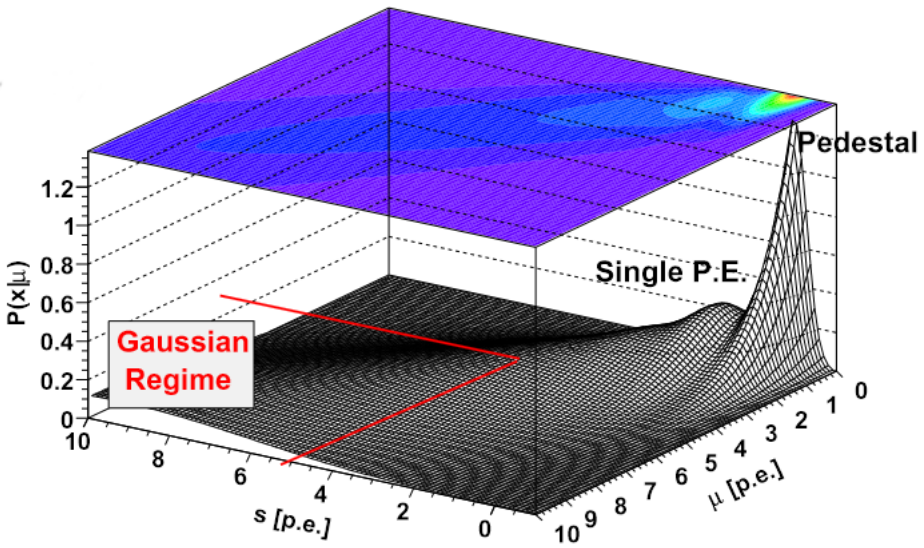

Figure 4.2: The figure shows a simultaneous Levenberg-Marquardt minimisation of measured pixel intensity, s, and 3D-model pixel intensity, μ, over Poissonian probability distribution of the photoelectrons, n, convolved with the photomultiplier resolution. The figure is taken from [41].

For the Levenberg-Marquardt minimisation, the Log-likelihood $\mathcal{L}$, is to be minimised over the probability in each pixel, p_i. The gradient $\beta_i = -\frac{\partial \mathcal{L}}{\partial p_i}$ and the Hessian $\alpha_{ij} = \frac{\partial^2 \mathcal{L}}{\partial p_i \partial p_j}$ is being used. The optimal step size is found by the steepest descent $\delta p_i = const \times \beta_i$, or by the quadratic approximation $\sum_{i=i}^{N} \alpha_{ki} \delta p_i = \beta_k$. By using a scaling parameter λ, the two methods are automatically varied by defining $\alpha'_{ii} = (1+\lambda)\alpha_{ii}$ and $\alpha'_{ij} = \alpha ij$ when $j \neq i$, which results in $\sum_{i=i}^{N} \alpha'_{ki} \delta p_i = \beta_k$. The five steps of the algorithm are;

1. Compute trial Log-likelihood solution starting with a small scaling parameter, $\lambda \sim 0.001$.

2. Compute $\mathcal{L}(p_i + \delta p_i)$ by first solving linear equations for δp_i.

3. Go back to 2 with updated parameter values and decrease λ if $\mathcal{L}$ decreases, otherwise, increase λ and go back to 2.

4. Repeat 2 and 3 until $\delta \mathcal{L}$ is below a threshold value, or a certain amount of iterations have been reached.

4.4 Energy Search

The eight 3D-model parameters are calculated by doing the aforementioned fitting and trigonometry on the shower images. This leaves the most important parameter to be able to do a line search in as a function of energy, namely the energy. The energy is found by searching reference sets using the 3D-model parameters. The search is done in the following way:

1. The appropriate reference file is chosen by noise and elevation angle.
2. The data is sorted according to the size of the expected number of Cherenkov photons, N_γ, since this parameter has the largest impact on the 3D-energy.
3. The best-fit N_γ is found in the reference sets, as well as its uncertainty.
4. The uncertainty interval is searched by minimising over the 3D-model parameters to find the best-fit reference set, i.e. the set of eight 3D-model parameters that fits the data the best.
5. The previous three steps are repeated with an additional set of criteria. The first criterion is that the same reference set can not be chosen. If the second best-fit reference set's energy is higher than that of the best-fit reference set, then the second best-fit reference set has to have higher values of N_γ and σ_{width}, and a lower value of S_{max} than the best-fit reference set. However, if the second best-fit reference set's energy is lower, then the opposite has to be valid for N_γ, σ_{width} and S_{max}.
6. (a) If a second best-fit reference set has been found, then the energy is interpolated using all the 3D-model parameters and the 3D-energy for that event is acquired.
   (b) If however, only one best-fit reference set has been found, i.e when the extra criteria is not fulfilled for any other reference set, then the energy is linearly scaled from the best-fit reference set to the input data.
7. By doing what was stated in Sec. 2.8.4, most of the bias is removed and the final energies are calculated.

Note that; in more than 95% of the searches, 6.a will be used. This is good because it recreates the energy more accurately than the simple scaling.

4.5 Line Search

Just as stated in Sec. 2.8.5, the line search has been done using a sliding-window approach. After all the cuts have been made and 3D-energy calculated, then the line search can be started.

1. The bin size is set to a value below the energy resolution, This makes the data effectively un-binned. Then the on-source and off-source fluxes are stored in two separate lists. The bin-centres are also stored in a separate list.

2. Each window is centred on a bin-centre with the width being the bin-centre energy ± 30% in logarithmic scale. The bin-centre is where any assumed DM line should be.

3. For each window, the on-region and off-region fluxes are fitted with $S_B \frac{E^{-\Gamma}}{E_\gamma}$ from Eq. 2.37. This is the Null Hypothesis in the likelihood fit.

4. For each window the entire right-hand side of Eq. 2.37 is fitted. This is the alternative hypothesis. It is required that $S_L > 0$, since a negative excess is non-physical. It is worth noting that the result is not very sensitive to the σ as long as it is on the order of the energy resolution.

5. The likelihood is calculated, after which the significance can be calculated via the Test Statistic, as described in Sec. 2.8.5 by using Eq. 2.38.

6. All values so far have been stored and are now corrected for trials by solving Eq. 2.41, taking into account that the signal strength is required to be ≥ 0.

Note for point 2: looking back at Eq. 2.39, $E_{binsize}$ in Eventdisplay is set to 0.05 in log. The lower edge is is ~ 0.3 TeV and higher edge is 10 TeV. The lower energy boundary can vary by a few bins depending on where the first non-zero bin appears. Looking at Eq. 2.40, ΔE is not constant throughout the energy interval, it changes from $\sim 24\%$ to $\sim 17\%$. From ~ 0.3 to 1 TeV the change is approximately linearly decreasing from the high to the low value, and above 1 TeV it is approximately constant at $\sim 17\%$.
Note for point 4: Taking the energy resolution values and dividing them by $2\sqrt{2ln(2)}$ converts them into widths of the Gaussian from Eq. 2.37, σ. Thus

σ is between $\sim 8.7\%$ and $\sim 12.5\%$ of the bin centre energy, E.
Note for point 6: Using an average value for the region $0.1 - 1$ TeV and the low value for $1 - 10$ TeV, leads to trials factors of $\sim 9 \pm 1.5$.

4.6 Choosing On- and Off-regions

The on- and off-regions can be chosen in different ways. Within the VERITAS collaboration, there are two standard ways used to chose the on- and off-regions. The two methods are called; *Ring Background* and *Reflected Regions Background*, [51].

In the Ring Background method, the off-region is in the shape of a ring with a thickness at some set distance from the centre where the on-region is. The size of this on-region is set with a parameter called θ^2, not related to the Cherenkov angle. This region is continuous unless there is a bright object that should be excluded. The gamma-ray and background acceptance of showers changes across the camera, this needs to be taken into account with the Ring Background method.

The Reflected Regions method uses a set number of off-regions, each with the same size as the source region, placed as close as possible, without overlapping, to the source region in the telescope image to estimate the background flux. The assumption is that there is a radial symmetry of acceptance.

The method used in this thesis is the Reflected Regions Background method because it does not need to be corrected for where in the camera the source is found.

4.7 Other Eventdisplay Methods

There are more analysis methods implemented in Eventdisplay, aside from the Hillas analyses and the 3D-model. During the time of writing of this thesis, three other advanced methods were being developed, i.e Frogs analysis, the Boosted Decision Trees, *BDTs*, Displacement, *Disp*, analysis method, and the BDT gamma/hadron separation method analysis.
The BDT Disp analysis is an improved version of the standard analysis. The standard method for angular reconstruction is based on the weighted

intersection of the major image axes. The Disp method estimates the position of the source along the major axis of each image. As a result, the Disp method provides an independent measurement of the source location for each image. BDT Disp analysis uses BDTs with the Disp method parameters to cut on. Frogs is based on template analysis. Instead of having look-up tables with values, Frogs analysis does a 2D-image comparison between the shower image and the template images. The methodology for Frogs has similarities with both Hillas analysis and 3D-model analysis. The benefit is that the Frogs method has a slightly better energy and angular resolution at higher energies than the Hillas and 3D-model methods. The Frogs method is, however, less sensitive at the lowest energies and it is much slower than the Hillas and 3D-model methods. On average the 3D-model and Frogs are on par, but computationally the 3D-model is faster. The following figure depicts the relation between Hillas, 3D-model and Frogs for a standard analysis of the Crab.

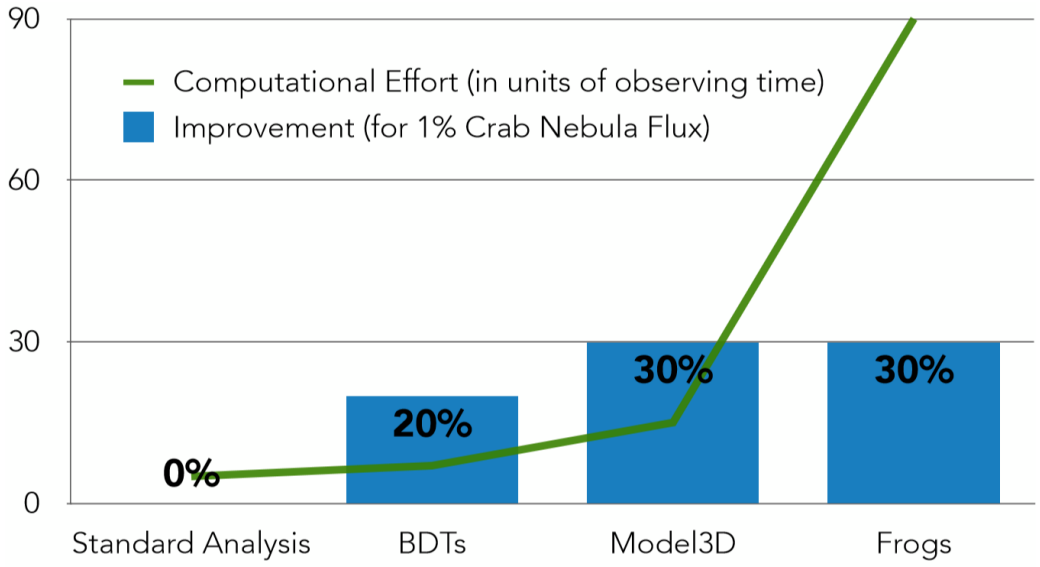

Figure 4.3: Computational increase and improvement in shower reconstruction quality for the different methods. The figure is taken from [41].

There is currently an idea to merge all the methods to automatically choose the best method for each event, which is a promising concept, but might be very hard to implement due to the differences in the methods.

4.8 Method Summary

The 3D-model method is a more advanced method to analyse Cherenkov showers than Hillas analysis. The 3D-energy with bias correction and line search are newly implemented features in Eventdisplay. How the 3D-model works by fitting a 3D-gaussian a shower has been shown as well as how the reference files are searched to get the 3D-energy and how the bias correction is done. Both the GrISU- and CARE-package where used to analyse simulations for the reference files in order to be able make a comparison of possible improvements that can be had in the future.

Chapter 5

Data

5.1 Target Selection

The targets were selected at the midpoint of the thesis work, i.e. 2013-2014. Selecting which targets that were to be used was based on the most recent knowledge about which targets would be good for DM searches. As a starting point, the target list in [22] was used. These are the standard dSph DM targets that can be seen by VERITAS. It also makes for easy comparison of the results.
As a sanity check, the Crab was also analysed. As a bit of a side project, a few runs of M87 was included as well. This was done to see how the 3D-model with 3D-energy, that had been optimised for DM searches, handles a different target type.
Comparing J-factors with different publicised works has to be done carefully because they are either shown in units of $[\mathrm{GeV}^{-2}\mathrm{cm}^{-5}\mathrm{sr}^{-1}]$ or $[\mathrm{M_o}^{-2}\mathrm{kpc}^{-5}\mathrm{sr}^{-1}]$. The conversion factor between them is $5.32 \cdot 10^{-21}[\mathrm{GeV}^{-2}\mathrm{cm}^{-5}\mathrm{sr}^{-1}] = 2.37 \cdot 10^{-14}[\mathrm{M_o}^{-2}\mathrm{kpc}^{-5}\mathrm{sr}^{-1}]$, see [21].
The full list of targets with distances, exposure time, J-factors and M/L are shown in the following table:

Table 5.1: Analysis targets. Mass-to-light ratios taken from [70] for all DM targets except for Willman 1, which was acquired from [74]. The J-factors were taken from the data of [39] for a θ^2 cut of 0.013 except for Willman 1 which was from [3]. The exposure is for GrISU/CARE.

Target	Distance [kpc]	Exposure [Min]	J_{ann} 10^x [$\text{GeV}^2\text{cm}^{-5}$]	J_{dec} 10^x [$\text{GeV}^2\text{cm}^{-5}$]	M/L [$\text{M}_\odot$/ $\text{L}_\odot$]	Comment
Boötes I	62	842.10 / 0	17.64	17.03	130	DM target
Draco	80	2007.23 / 0	18.09	17.45	440	DM target
Segue 1	23	6055.00/ 277.43	18.99	17.39	3400	DM target
Ursa Minor	66	3707.70/ 135.55	18.80	17.46	75	DM target
Willman 1	38	841.97 / 0	18.93	17.34	800	DM target
Crab	2	841.10 / 841.10	0	-	-	Sanity check
M87	16400	180.23 / 180.23	0	-	-	Function test

For DM targets, there was a total of ~ 224 hours of analysed data using GrISU-based analysis and ~ 7 hours using CARE-based analysis. For non-DM targets a total of ~ 19 hours was analysed with using both GrISU- and CARE-based analysis. The times stated are post analysis cuts.
As can be seen in the table, for the DM targets, they are all at a distance closer than 100 kpc and a M/L that is at least ~ 100 $\text{M}_\odot$/ $\text{L}_\odot$. The most promising DM targets have a $\text{M}_\odot$ / $\text{L}_\odot$ > 1000.
The annihilation J-factors was mostly from [39], except for the J-factor for Willman 1, which was from [20]. The J-factor was converted using the conversion factor of $2.25 \cdot 10^{-7}$ to get from $\text{M}^2\text{kpc}^{-5}$ to $\text{GeV}^2\text{cm}^{-5}$. These are valid for this thesis since the DM target assumptions are the same as in this thesis.
The J-factors for the Crab and M87 have been set to zero, thus the flux correction becomes equal to 1, meaning that no correction is made. Since these three are not DM targets, the $\text{M}_\odot$/ $\text{L}_\odot$ is also not of interest.

5.2 Data Reduction

There is more data available from VERITAS on the targets chosen than has been used for this thesis. The main choice to not use a certain data run is that the weather during the observations was not good. From a scale A-D, A being good quality and D being unusable, any data run labelled C or worse is discarded. Data sets do, from time to time, have anomalous spikes in the measured fluxes, from for example the telescopes being struck by the headlights of a car, or get higher fluxes and more fluctuations due to clouds moving in over the telescopes. Such events have been cut out from the analysed files. In the analysis stage where the 3D-energy is being calculated, the events are examined to see if they have been given a full set of 3D-model parameters. If that has not happened, the events are not used in the analysis, though this is less than one percent of all events per data run. Events are naturally also cut if they do not fulfil the cut criteria.
The full data run list is shown in Appendix A and the 3D-energy cut criteria can be seen in Appendix B.

5.3 Data Summary

The five chosen DM targets have been used before and thus makes for easy comparison. The Crab was chosen as a target because it is the standard choice for calibration. The last two targets were chosen to test the 3D-model with 3D-energy outside its intended DM search purpose.

Chapter 6

Method Verification and Results

Verification of the newly implemented 3D-model with 3D-energy and the results produced by using it on real data will be presented in this chapter, as well as comparisons to standard analysis.

6.1 Performance Check and Extended Source Test

The Crab was used to do a performance check on the 3D-model with 3D-energy analysis method. The Crab was chosen because it is one of the most well studied and well understood sources in ground-based gamma-ray astronomy. The following Figs. show, in flux as a function of energy, that the Crab flux and slope for the 3D-energy analysis are similar to the result from a standard analysis. The following figure shows an 3D-model analysis done of the Crab using the GrISU-based reference files:

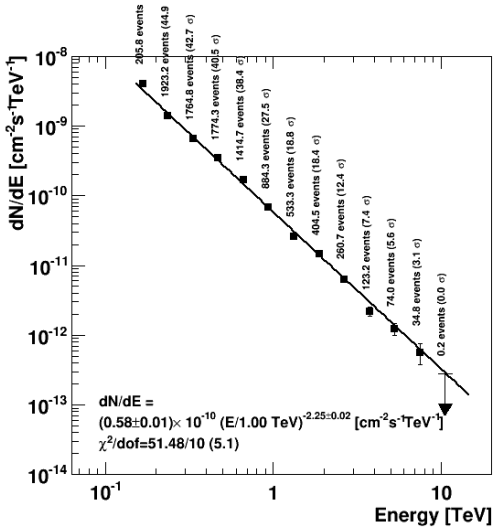

Figure 6.1: Low activity state Crab flux using GrISU-based analysis.
The normalisation is $(5.8 \pm 0.1) \cdot 10^{-11}\mathrm{TeV}^1\mathrm{cm}^{-2}\mathrm{s}^{-1}$ and the slope is -2.25 ± 0.02.

This should be compared to the following standard analysis of the Crab that shows photon flux that has been fitted with the log-parabola function $\frac{dN}{dEdAdt} = f_0 \left(\frac{E}{E_0}\right)^{\alpha+\beta\log(E/E_0)}$, where f_0 is the normalisation, α is the photon index, β is the curvature, E is the energy and E_0 is the normalisation energy. This can be seen in Fig. 6.2:

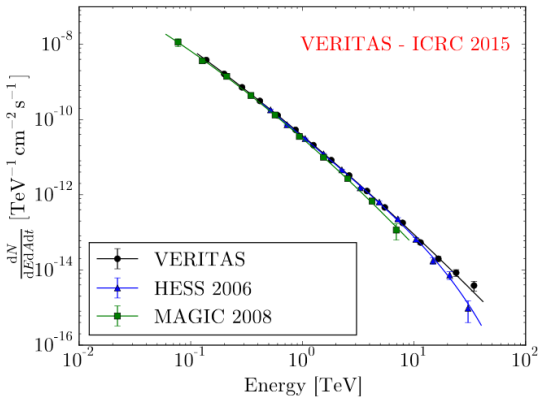

Figure 6.2: Crab flux using standard analysis. The data is fitted to a log-parabola function with the values; $f_0 = (3.75 \pm 0.003) \cdot 10^{-11}\mathrm{TeV}^1\mathrm{cm}^{-2}\mathrm{s}^{-1}$, $\alpha = -2.467 \pm 0.006$ and $\beta = -0.16 \pm 0.001$. The figure is taken from [45].

As can be seen, the 3D-energy analysis has a flux that is approximately 50% higher. The slope is less steep, even when taking into account that the 3D-energy analysis was fitted with a simple power law without curvature. From internal notes, where the Crab was fitted with a power law without a slope, the normalisation was $(3.07 \pm 0.003) \cdot 10^{-11}\text{TeV}^1\text{cm}^{-2}$ and the slope had a value of -2.48 ± 0.01.

Compared to spectra from other telescopes, the 3D-energy analysed Crab spectra is in fairly good agreement:

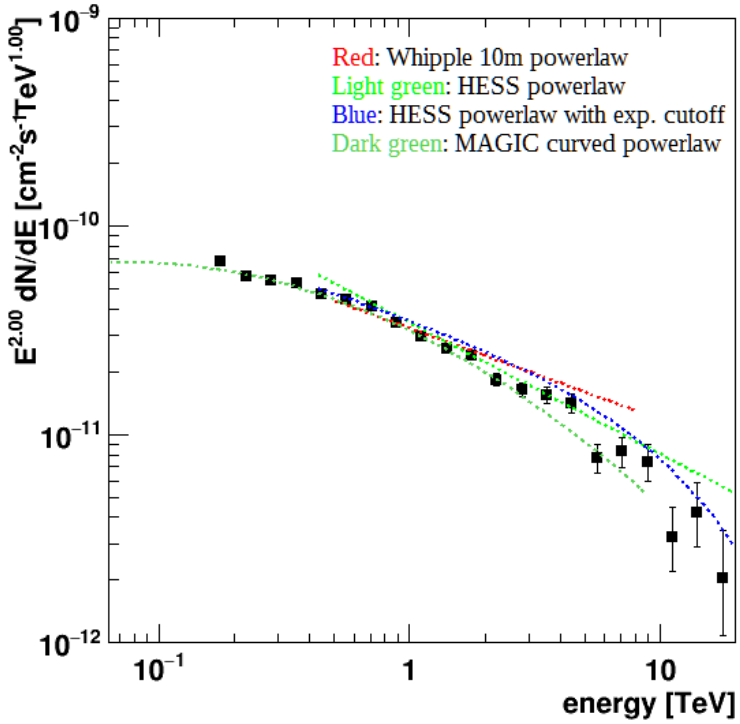

Figure 6.3: Crab fluxes from other telescopes; Red: Whipple 10m powerlaw, Light green: HESS powerlaw, Blue: HESS powerlaw with exp cutoff, and Dark green: MAGIC curved powerlaw. The figure is based on published data and taken from [30]. Note the multiplication with $E^{2.00}$.

An analysis was performed on an extended source to test the usefulness of the 3D-energy on non-DM targets, specifically, M87 was used. The resulting flux from this analysis can be seen in the following flux vs. energy figure:

Compare this to an analysis focused on M87:

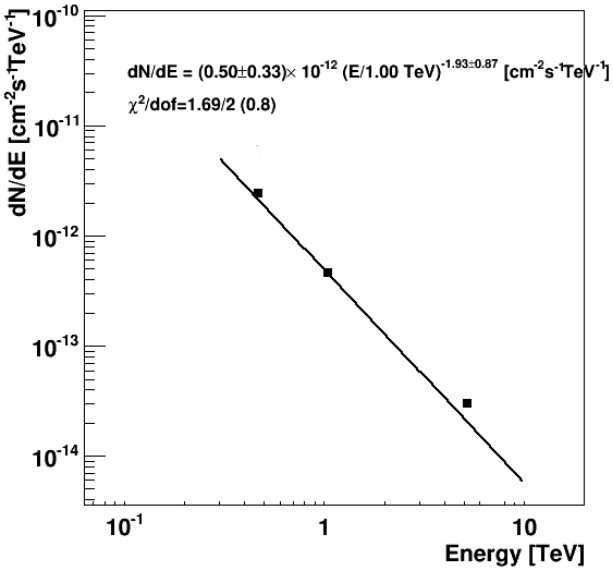

Figure 6.4: M87 flux using 3D-energy analysis. The uncertainties of each point, not shown in the figure, are approximately double that of standard analysis.

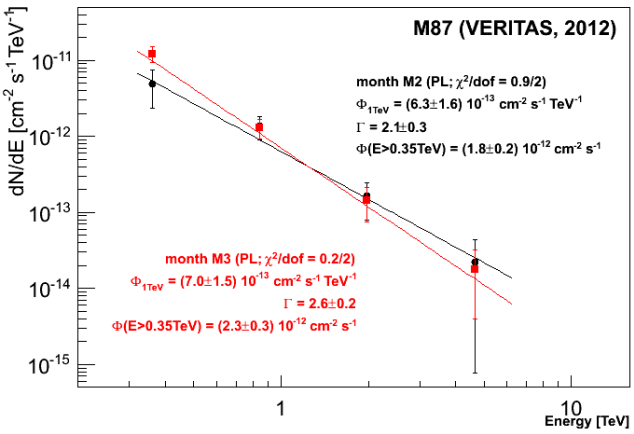

Figure 6.5: M87 flux for two different months. The figure is taken from [11].

The analysis of M87, using 3D-energy analysis, is within the uncertainty of standard analysis, i.e the black line in Fig. 6.5. The errors in the 3D-energy analysis of M87 is approximately double that of standard analysis, due to the low number of data runs used.

6.2 Performance Comparison

Comparing the 3D-model analysis to the other available analysis methods in Eventdisplay has already been partly shown in Sec. 4.8, with Fig. 4.3. The 3D-model analysis does well when comparing it to other analysis methods when looking at computational effort vs. reconstruction quality improvement for a 1% Crab flux.

6.2.1 Computational Speed

The 3D-energy adds a small amount of extra computational effort and time to the 3D-model analysis. The CARE-based analysis takes more computational effort and time, in comparison to the GrISU-based analysis. The reason for this is that the reference files contains more data, approximately a factor ~ 10. However, the analysis time increase is a factor ~ 3. The GrISU-based 3D-energy analysis takes $\sim 10\%$ of the total analysis time. This can vary a bit depending on the quality of the data that is being analysed. If the data has little variance and is clustered towards lower energies, which is preferable for the DM search in this work, the search through the 3D-energy reference set files will be faster.

Running the line search takes 45 ± 15 seconds for ~ 200 hours of data with the binsize set as described in Chapter 4. The more bins that are used the more time it takes to compute.

6.2.2 Effective Area

To get the correct effective area for the analysis, cuts have been applied to simulations. The following comparison of effective area is between the 3D-energy analysis, and the standard analysis using soft cuts. The cuts for the 3D-model effective areas are based on the standard analysis soft cut files. These files have been altered by adding the 3D-model parameters that is to be used for the parameter cuts.

It can be seen in Fig. 6.6, that the effective area between ~ 300 GeV and ~ 3 TeV is up to ~ 2 times larger for the 3D-energy analysis than for standard analysis.

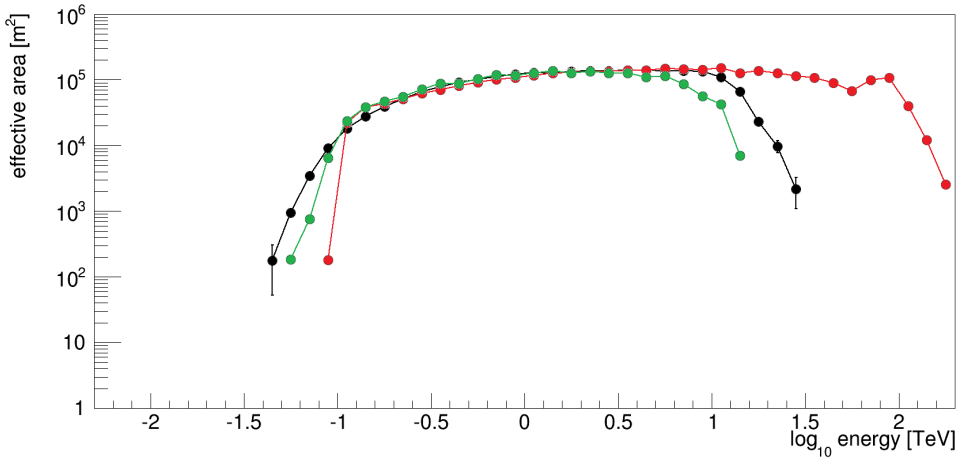

Figure 6.6: Effective areas when applying standard analysis soft cuts, cuts for CARE-and GrISU-based analysis. The colours are red, black and green respectively. All effective areas have a θ^2 cut of 0.008 steradians.

The drop-off above $\sim$ 10 TeV in the CARE- and GrISU-based effective areas is due to the cuts chosen, for example, a higher edge cut on the number of expected photons. This has no significant impact on this thesis, since that is higher than the energy region of interest, which is $0.01 - 1$ TeV. The reason that the effective area is larger on average is due different events being cut. The effective area is larger also because of the way that the 3D-model projects back the recreated event onto the image plane, thus gaining more information than standard analysis and allowing for greater ground coverage. Fig. 6.6 shows the effective area for a θ^2 cut equal to 0.08 steradians, whereas the effective areas used were for a θ^2 cut of 0.013 steradians. These effective areas are larger, as can be seen in Fig. 6.7 and 6.8.

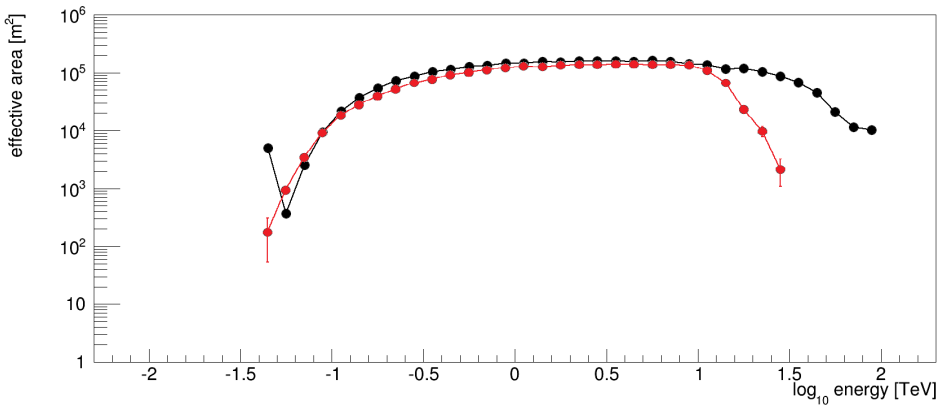

Figure 6.7: Effective area plot for the CARE-based 3D-energy. The black and red line is for a θ^2 cuts of 0.008 and 0.013 steradians respectively.

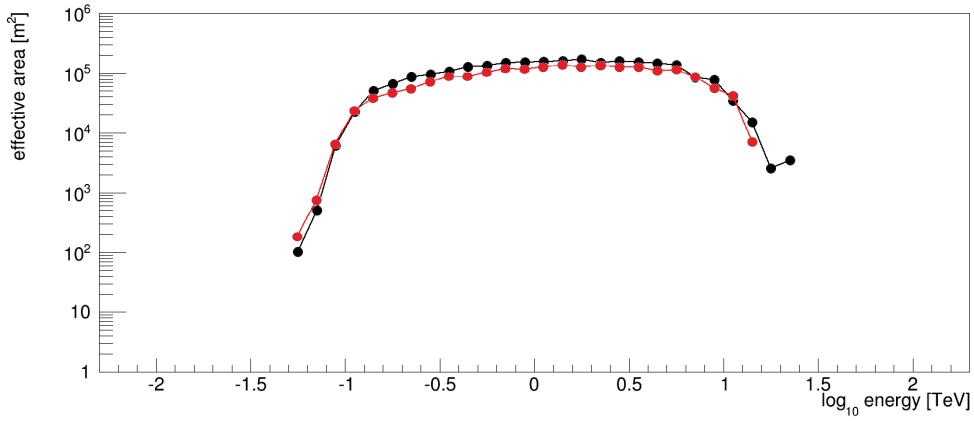

Figure 6.8: Effective area plot for the GrISU-based 3D-energy. The black and red line is for a θ^2 cuts of 0.008 and 0.013 steradians respectively.

The effective areas for the 3D-energy analysis show small improvements over standard analysis effective areas.

The effective areas based on CARE are larger than the effective areas based on GrISU, due to more a larger amount of higher quality simulation data and event reconstruction capabilities.

6.2.3 Energy Resolution

The energy resolution of the 3D-energy analysis is on average finer than the standard analysis energy resolution. The standard analysis is stated to have $13 - 18\%$ in energy resolution at 1 TeV, depending on if soft, medium or hard cuts are used. The harder the cut the finer the energy resolution, because the criteria for what is allowed to pass as a gamma-ray photon event is more constrained. As can be seen in Fig. 6.9-6.13, the difference is at most a few percent. At certain energies, depending on the elevation and energy range, the standard analysis energy resolution is finer than the 3D-energy energy resolution.

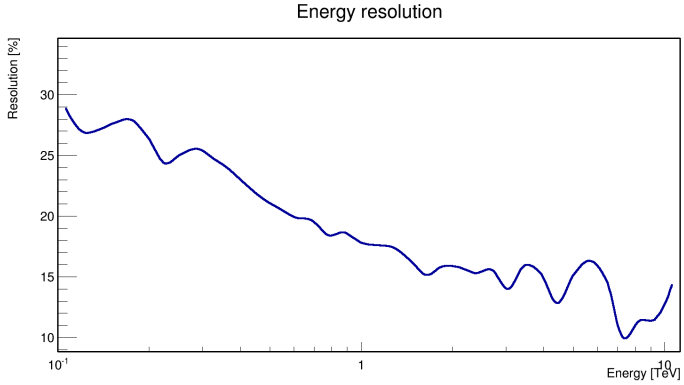

Figure 6.9: 3D-energy resolution with noise level of 75 MHz (low noise), GrISU-based, winter atmosphere, telescope configuration 6 and elevation 70 degrees.

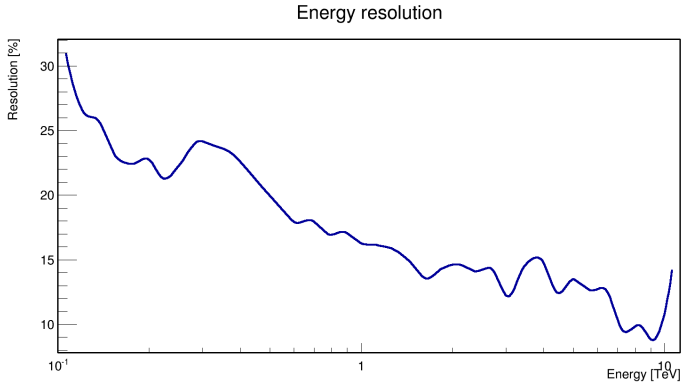

Figure 6.10: 3D-energy resolution with noise level of 75 MHz (low noise), GrISU-based, winter atmosphere, telescope configuration 6 and elevation 60 degrees

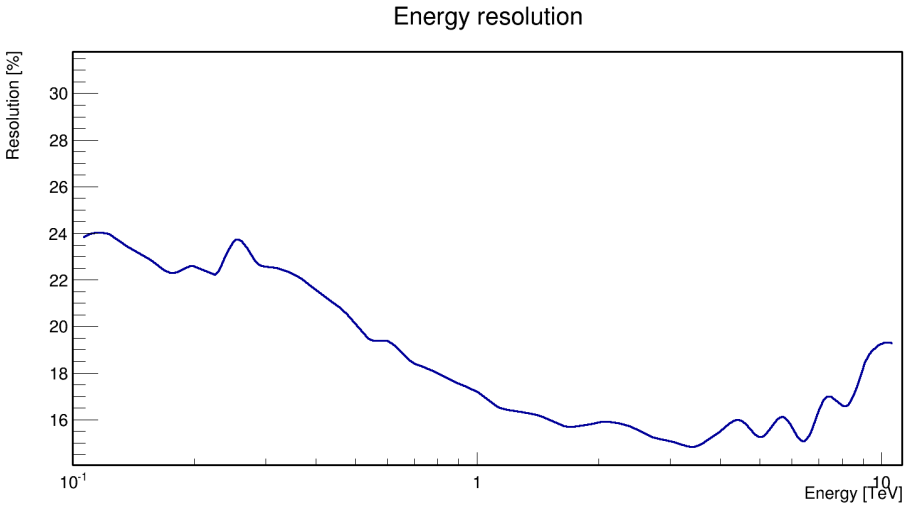

Figure 6.11: 3D-energy resolution using noise level of 50 MHz (low noise), CARE-based, winter atmosphere, telescope configuration 6 and elevation 70 degrees.

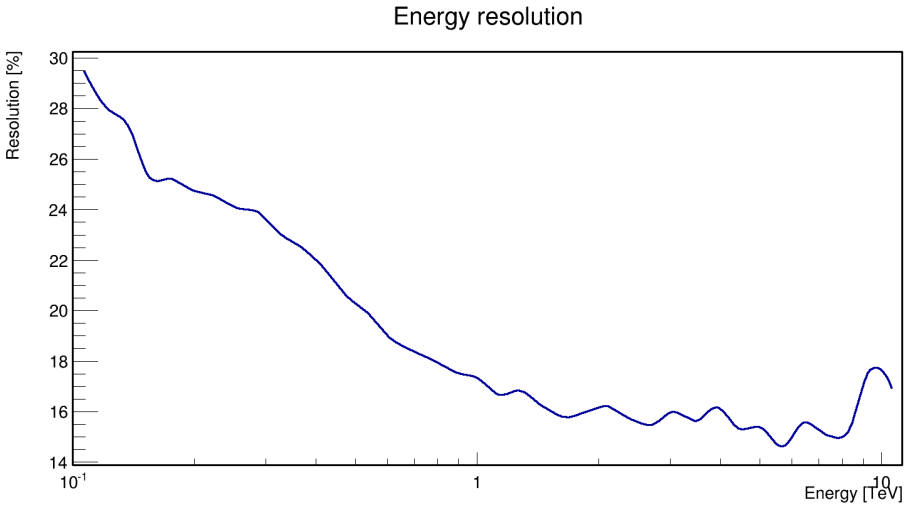

Figure 6.12: 3D-energy resolution using noise level of 50 MHz (low noise), CARE-based, winter atmosphere, telescope configuration 6 and elevation 60 degrees.

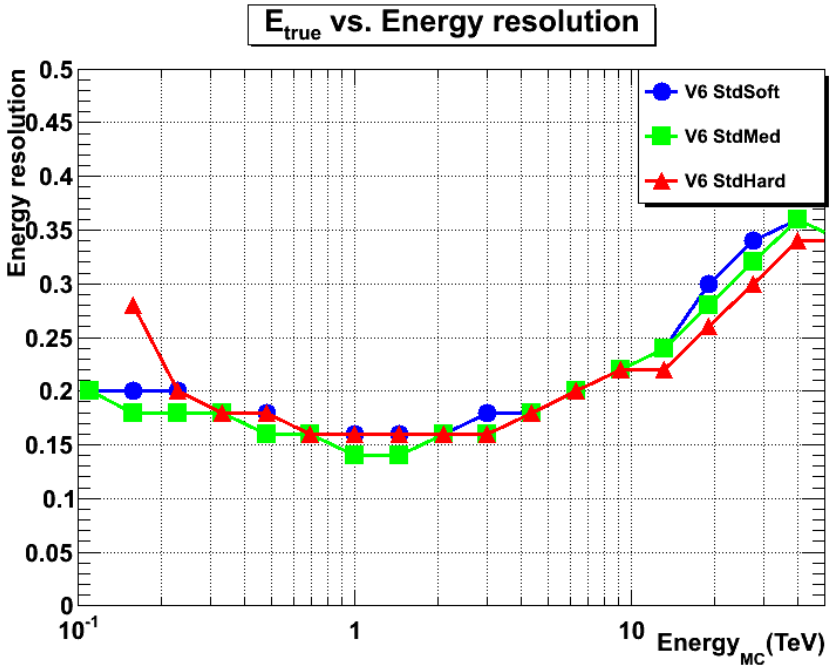

Figure 6.13: Energy resolution using standard analysis with VEGAS for V6. The figure is taken from [55].

Fig. 6.13 was created using VEGAS, but the energy resolution is within $\sim 1\%$ of the energy resolution of Eventdisplay.

6.2.4 Energy Threshold

The theoretical energy threshold limit for VERITAS has not yet been reached with any analysis method. The 3D-energy analysis has a lower energy threshold when compared to the standard analysis. From the current threshold of 300 GeV [76], or in optimistic cases 200 GeV (internal VERITAS studies), there has been an improvement of $\sim 10\%$ from the optimistic case. The lowest energy threshold calculated when using 3D-energy analysis was ~ 178 GeV.

6.2.5 Bias Correction

After the bias-correction has been applied, the average bias is less than 4% in the energy range $0.1 - 10$ TeV, and on average less than 1%. Comparing this to the standard analysis using soft cuts, it can be seen that the gain is mostly at energies below 0.4 TeV.

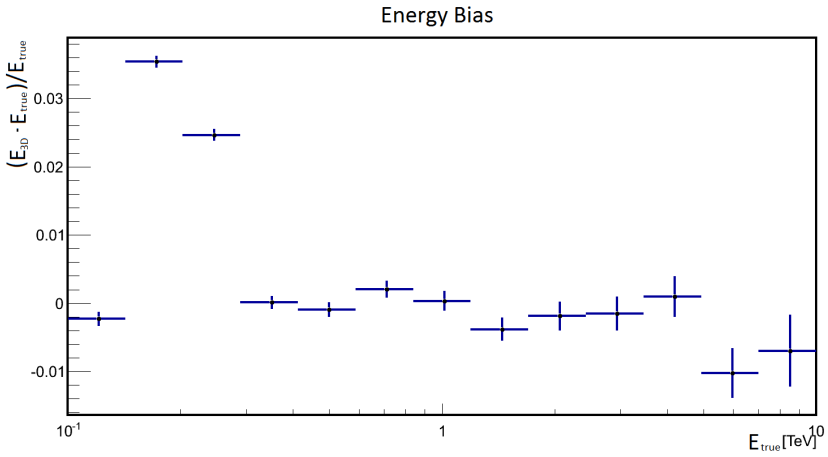

Figure 6.14: 3D-energy bias after bias-correction for V6 and 20 degrees using GrISU-based analysis.

Fig. 6.15 shows bias curves for standard analysis.

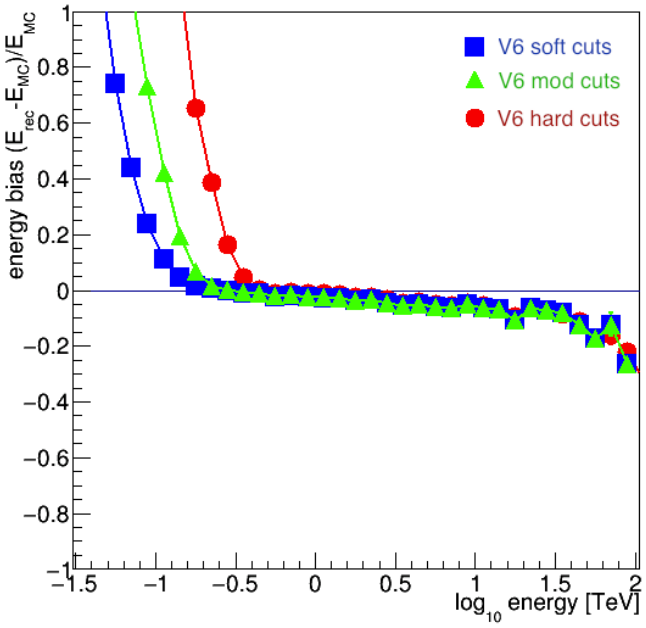

Figure 6.15: Bias curves for standard analysis in Eventdisplay for V6 and 20 degrees using GrISU-based analysis and a newer version of Eventdisplay than used for the 3D-energy. The figure is taken from [30].

6.3 Line Search Results and Upper Limits

Within the time frame of available CARE simulations, V6 winter, only data from Segue 1 and Ursa Minor were available, which prevents the upper limits from being competitive.

As was expected, due to the limits of VERITAS and the amount of data gathered and analysed, no line has been found at any significant level. In the absence of significant lines, upper limits have also been calculated. Note that the assumed spectral index for all DM targets was -2.4. This is common practise when studying DM in dSphs because it is a standard spectral indexes for astrophysical sources, [43] and references therein.

The trials correction value was calculated using Eq. 2.40 for each target. CARE-based, GrISU-based and the stacked analysis are handled separately. For the CARE targets, the trial correction values are 10.4 and 9.3 for Segue 1 and Ursa Minor respectively. The sum is the trials factor. For the targets in the CARE-based analysis, this is 19.7. The value for each GrISU target is 8.0, 8.3, 8.6, 8.3 and 7.7 for Boötes I, Draco, Segue 1, Ursa Minor and Willman 1 respectively. Thus, for targets in the GrISU-based analysis, the trials factor is 41.1. The stacked CARE-based analysis trials factor is 10.4, and 8.6 for the GrISU-based stacked analysis.

None of the upper limit cross section figures show the uncertainty. This is to make the figures easier to understand. The dominant part of the uncertainty comes from the uncertainty in the J-factor, [39] as seen in Fig. 6.16:

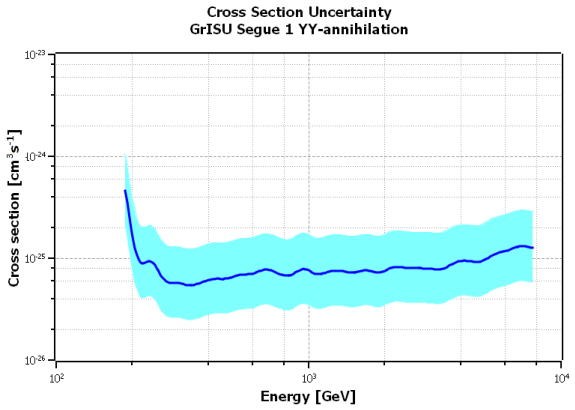

Figure 6.16: Cross section uncertainty due to large uncertainties in the J-factor. The dark blue line shows the $\gamma\gamma$-annihilation upper limit cross section and the light blue area is the uncertainty.

6.3.1 CARE-based Lines and Upper Limits

Tab. 6.1 shows the energies of the most prominent line signals, E_{Line}, along with their upper limit cross sections and significances for CARE-based analysis:

Table 6.1: This table contains the energy of the most prominent line signal, E_{Line}, its upper limit cross section and significances before/after trials correction for the CARE runlist targets.

Target	E_{Line} [GeV]	Cross section [$\mathrm{cm^3 s^{-1}}$]	Significance [σ]
Segue 1	749	$2.98 \cdot 10^{-24}$	2.22 / 0.83
Ursa Minor	422	$8.10 \cdot 10^{-24}$	2.73 / 1.56

The location of the lowest limits on the upper limit cross section, as well as their values for each target and particle outcome is displayed in Tab. 6.2.

Table 6.2: This table shows the value of the best upper limit cross sections and underneath those are the energies. This is shown for each of the particle outcomes of the CARE targets. The locations are in the units of [GeV] and the cross sections are in units of [$\mathrm{cm^3 s^{-1}}$].

Target	$\gamma\gamma$	$\tau^+\tau^-$	$b\bar{b}$	W^+W^-	Z^0Z^0
Segue 1	$2.60 \cdot 10^{-24}$	$2.56 \cdot 10^{-22}$	$7.18 \cdot 10^{-21}$	$3.77 \cdot 10^{-21}$	$4.88 \cdot 10^{-21}$
	266	944	1884	1189	1334
Ursa Minor	$3.51 \cdot 10^{-24}$	$5.10 \cdot 10^{-22}$	$6.55 \cdot 10^{-21}$	$3.87 \cdot 10^{-21}$	$4.80 \cdot 10^{-21}$
	7499	944	2113	1334	1334

The three following figures are a line significance plot, Fig. 6.17, and upper limit cross section plots, Fig. 6.18-6.19. These are the corresponding figures to Tab. 6.1 and 6.2.

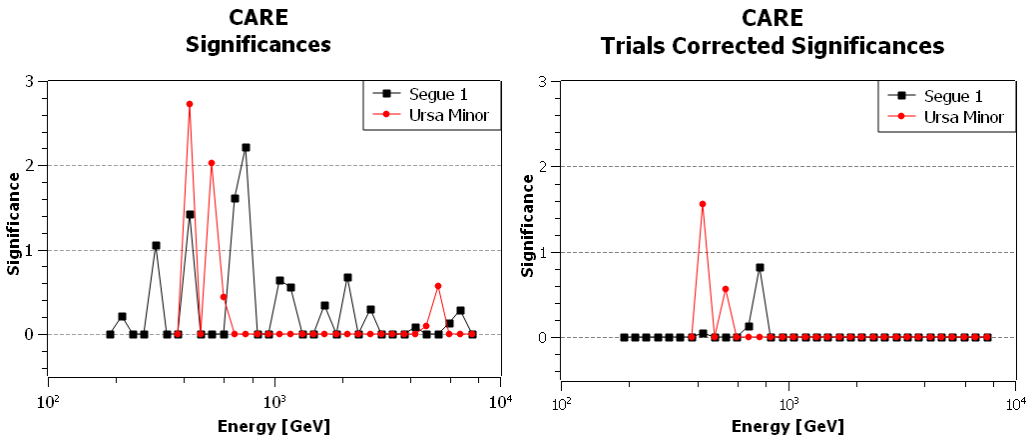

Figure 6.17: Line significances using CARE-based analysis for Segue 1 and Ursa Minor. Before and after trials correction, left and right figure respectively.

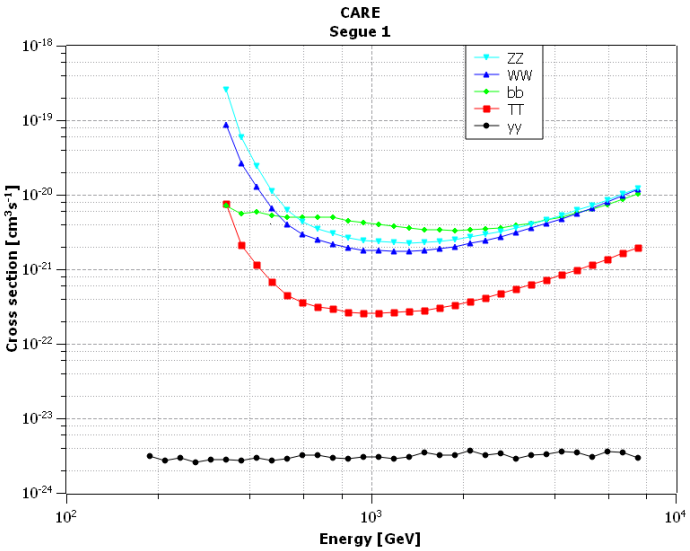

Figure 6.18: Segue 1 upper limit cross sections using CARE-based analysis.

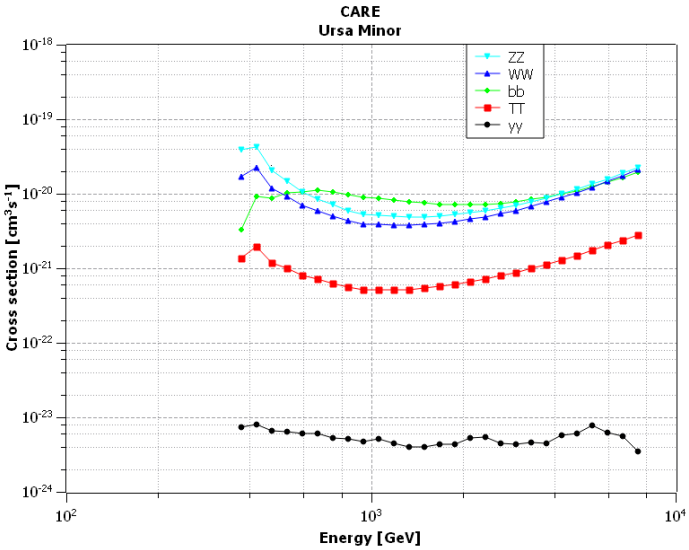

Figure 6.19: Ursa Minor upper limit cross sections using CARE-based analysis.

Low number statistics for the $\gamma\gamma$ flux resulted in that there are no data points below approximately 300 GeV for the CARE-based analysis of Ursa Minor. This is not the case for the CARE-based analysis of Segue 1.

6.3.2 GrISU-based Lines and Upper Limits

Tab. 6.3 contains the energy of the most competitive upper limit cross sections and their values for each target and particle outcome for GrISU-based analysis.

Table 6.3: This table contains the energy of the most prominent line signal, E_{Line}, its upper limit cross section and significance before/after trials correction for the GrISU-based analysis. Note: significance values below $1 \cdot 10^{-5}$ is set to 0.00.

Target	E_{Line} [GeV]	Cross section [$\mathrm{cm^3 s^{-1}}$]	Significance [σ]
Boötes I	668	$2.12 \cdot 10^{-23}$	0.63 / 0.00
Draco	841	$2.88 \cdot 10^{-24}$	0.49 / 0.00
Segue 1	473	$1.34 \cdot 10^{-25}$	1.43 / $1.30 \cdot 10^{-3}$
Ursa Minor	5308	$2.93 \cdot 10^{-25}$	0.19 / 0.00
Wilman 1	1679	$1.33 \cdot 10^{-24}$	0.86 / 0.00

The lowest upper limit cross section and energy for each target and particle outcome are displayed in Tab. 6.4.

Table 6.4: This table shows the value of the best upper limit cross sections and its energy for each of the particle outcomes of the GrISU targets. The energies are in the units of [GeV] and the cross sections are in units of $[\mathrm{cm}^3\mathrm{s}^{-1}]$.

Target	$\gamma\gamma$	$\tau^+\tau^-$	$b\bar{b}$	W^+W^-	Z^0Z^0
Boötes I	$9.73 \cdot 10^{-24}$	$6.46 \cdot 10^{-22}$	$5.57 \cdot 10^{-21}$	$4.42 \cdot 10^{-21}$	$5.76 \cdot 10^{-20}$
	299	841	376	1059	1189
Draco	$2.23 \cdot 10^{-24}$	$1.31 \cdot 10^{-22}$	$1.92 \cdot 10^{-21}$	$9.53 \cdot 10^{-22}$	$1.24 \cdot 10^{-21}$
	531	1059	1679	1189	1334
Segue 1	$8.56 \cdot 10^{-26}$	$4.93 \cdot 10^{-24}$	$6.61 \cdot 10^{-23}$	$3.51 \cdot 10^{-23}$	$4.61 \cdot 10^{-23}$
	211	944	376	944	1189
Ursa Minor	$2.51 \cdot 10^{-25}$	$1.08 \cdot 10^{-23}$	$1.61 \cdot 10^{-22}$	$7.88 \cdot 10^{-23}$	$1.04 \cdot 10^{-22}$
	473	944	1884	1059	1059
Willman 1	$1.16 \cdot 10^{-24}$	$3.89 \cdot 10^{-23}$	$4.54 \cdot 10^{-22}$	$2.68 \cdot 10^{-22}$	$3.53 \cdot 10^{-22}$
	2661	1059	473	1059	1059

The following six figures are a line significance plot, Fig. 6.20, and upper limit cross section plots, Fig. 6.21-6.25. These are the corresponding figures to the Tab. 6.3 and 6.4.

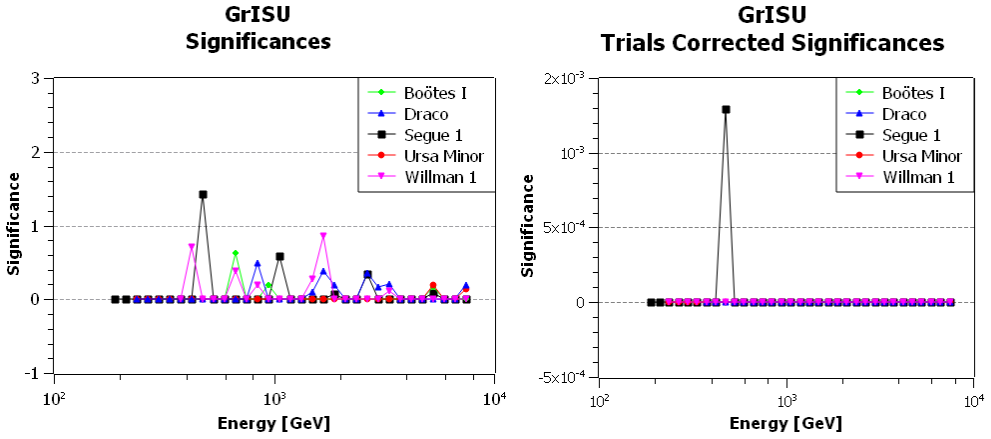

Figure 6.20: Line significances using GrISU-based analysis for Boötes I, Draco, Segue 1, Ursa Minor and Willman 1. Before and after trials correction, left and right figure respectively.

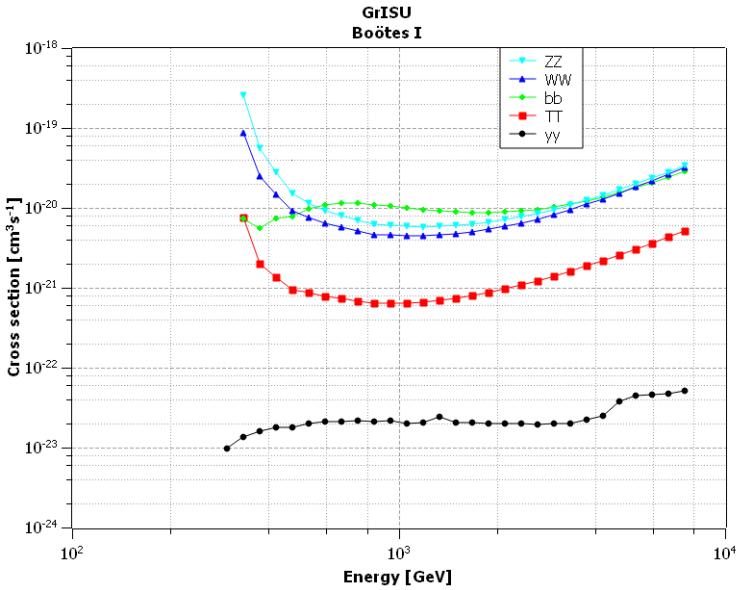

Figure 6.21: Boötes I upper limit cross sections using GrISU-based analysis.

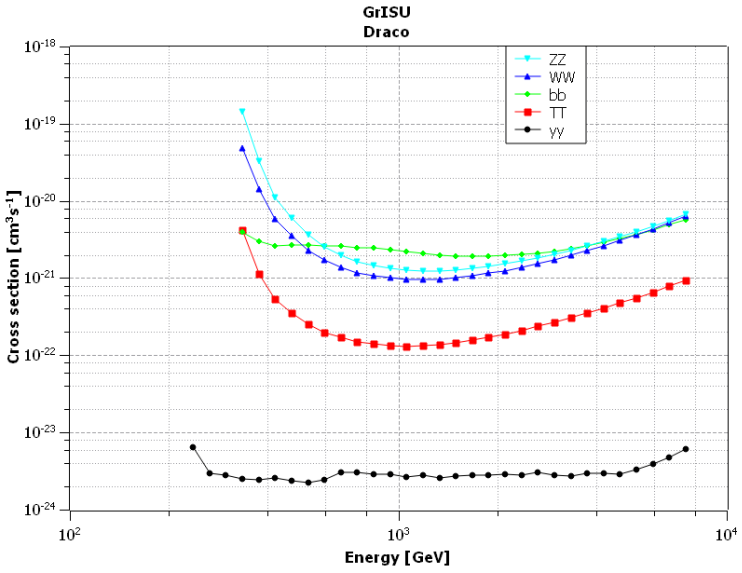

Figure 6.22: Draco upper limit cross sections using GrISU-based analysis.

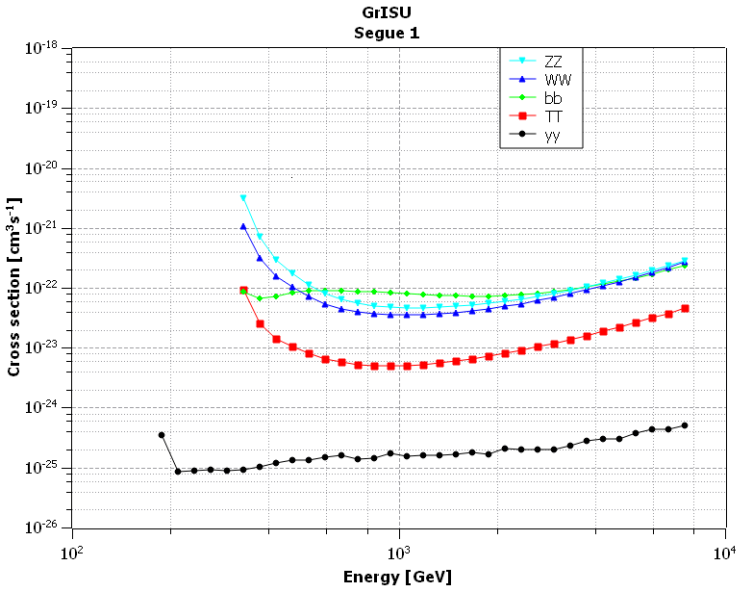

Figure 6.23: Segue 1 upper limit cross sections using GrISU-based analysis.

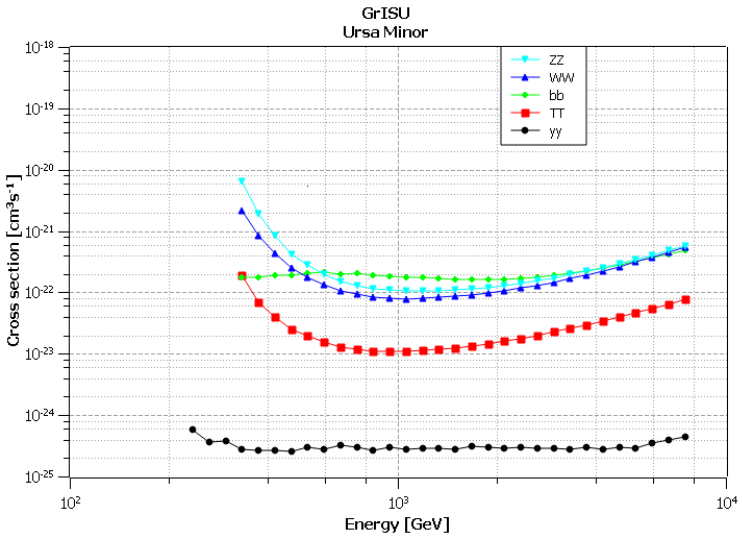

Figure 6.24: Ursa Minor upper limit cross sections using GrISU-based analysis.

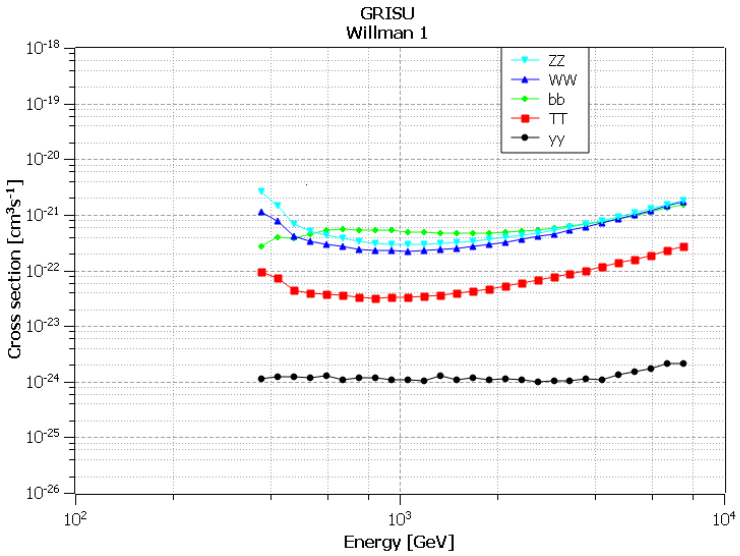

Figure 6.25: Willman 1 upper limit cross sections using GrISU-based analysis.

There are no data points below approximately 300 GeV for the GrISU-based analysis of Willman 1, due to low number statistics for the $\gamma\gamma$ flux. This is not the case for the other GrISU-based analysis targets.

6.3.3 Stacked Analysis Lines and Upper Limits

"Stacked analysis" refers to when all targets are analysed as one set, taking care that each targets effective area and J-factor is correctly applied.

Tab. 6.5 shows the energy of the most prominent line signals, E_{Line}, their upper limit cross sections and significances for stacked CARE- and GrISU-based analysis:

Table 6.5: This table contains the energy of the most prominent line signal, E_{Line}, its upper limit cross section and significance before/after trials correction for stacked CARE- and GrISU-based analysis.

Sim. base	E_{Line} [GeV]	Cross section [$\mathrm{cm^3 s^{-1}}$]	Significance [σ]
CARE	422	$2.92 \cdot 10^{-24}$	1.66 / 0.55
GrISU	473	$6.11 \cdot 10^{-26}$	0.72 / $1.66 \cdot 10^{-3}$

Tab. 6.6 contains the energies and the most competitive upper limit cross section for each target and particle outcome for CARE- and GrISU-based analysis:

Table 6.6: This table shows the best upper limit cross sections values and underneath those are the energies. This is shown for each of the outcomes of the stacked CARE- and GrISU-based analysis. The energies and cross sections are in units of [GeV] and [$\mathrm{cm}^3\mathrm{s}^{-1}$] respectively.

Sim. base	$\gamma\gamma$	$\tau^+\tau^-$	$b\bar{b}$	W^+W^-	Z^0Z^0
CARE	$2.20 \cdot 10^{-24}$	$2.03 \cdot 10^{-22}$	$2.62 \cdot 10^{-21}$	$1.40 \cdot 10^{-21}$	$1.80 \cdot 10^{-21}$
	7499	1059	2113	1334	1334
GrISU	$5.21 \cdot 10^{-26}$	$3.34 \cdot 10^{-24}$	$4.86 \cdot 10^{-23}$	$2.38 \cdot 10^{-23}$	$3.13 \cdot 10^{-23}$
	335	944	1884	1059	1189

The following three figures are a line significance plot, Fig. 6.26, and upper limit cross section plots, Fig. 6.27-6.28. The figures correspond to the tables 6.5 and 6.5.

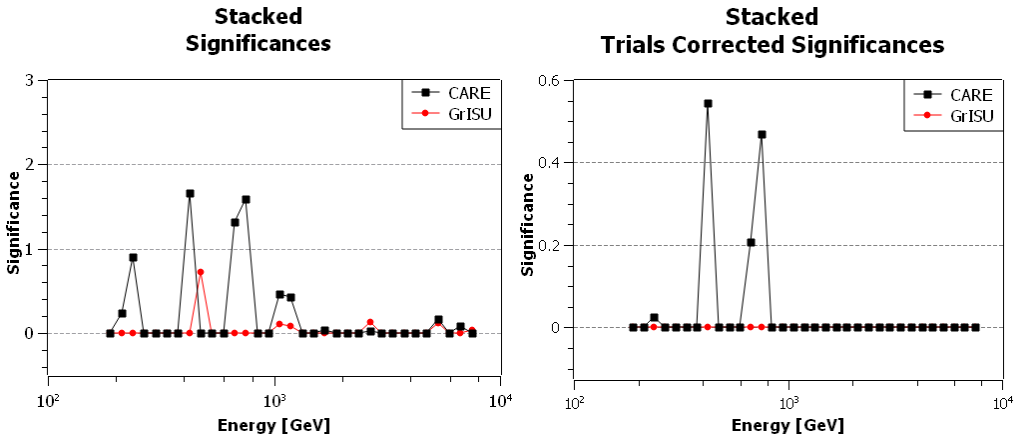

Figure 6.26: Line significances for the CARE- and GrISU-based stacked analysis. Before and after trials correction, left and right figure respectively.

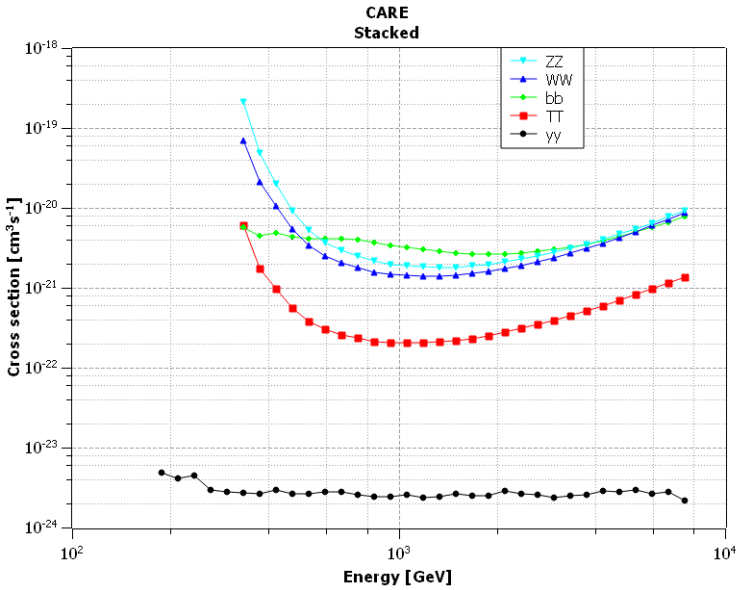

Figure 6.27: Upper limit cross sections for CARE-based stacked analysis.

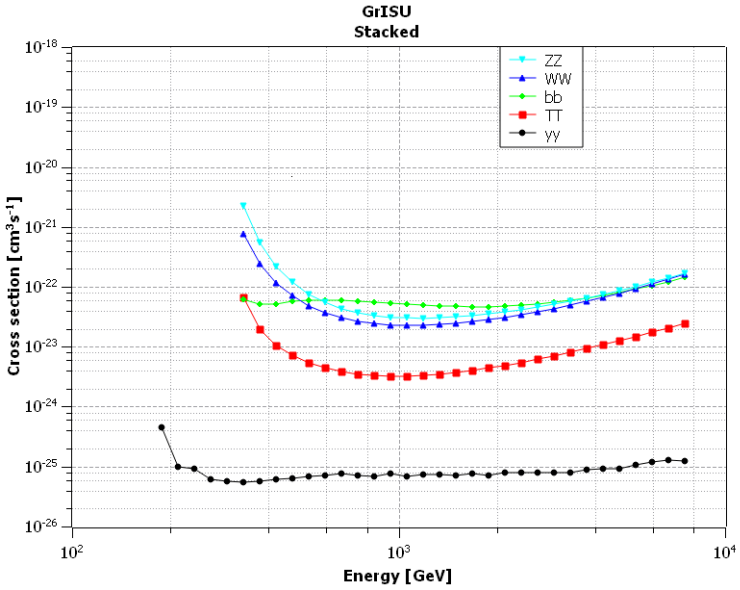

Figure 6.28: Upper limit cross sections for GrISU-based stacked analysis.

6.3.4 Comparison Between CARE and GrISU

A comparison was done between CARE- and GrISU-based analysis by taking the same data runs that were used for the analysis based on CARE simulations and performing an analysis based on GrISU simulations. The following table shows a comparison of the most prominent line signals between CARE- and GrISU-based analysis.

Table 6.7: In the first column are the target names. In the second column, for each target, is the upper limit cross section of the most prominent line signal using GrISU-based simulations during analysis. Underneath the cross section is the line energy, and below that the significance before/after trials correction. The third column contains the upper limit cross section at the same energy but with analysis based on CARE simulations. The final column has the upper-limit cross section and energy for the search at the same energy of the most prominent line with the CARE-based analysis, but using analysis based on GrISU simulations. The units of the energies, cross sections and significances are in [GeV], [$\mathrm{cm^3 s^{-1}}$] and [σ] respectively.

Target	GrISU line	CARE equiv.	CARE line GrISU equiv.
Segue 1	$4.00 \cdot 10^{-24}$	$2.69 \cdot 10^{-24}$	$4.50 \cdot 10^{-24}$
	376	376	749
	2.66/1.84	0.00/0.00	0.00/0.00
Ursa Minor	$7.83 \cdot 10^{-24}$	$7.44 \cdot 10^{-24}$	$6.72 \cdot 10^{-24}$
	376	376	422
	3.68/3.10	0.00/0.00	2.10/1.12
Stacked	$2.80 \cdot 10^{-24}$	$2.63 \cdot 10^{-24}$	$3.04 \cdot 10^{-24}$
	376	376	422
	2.70/1.89	0.00/0.00	$1.66/4.46 \cdot 10^{-1}$

Tab. 6.7 contains the lowest upper limit cross sections and their energies for the analysis based on GrISU simulations, but using the CARE runlist. The table content should be directly compared to Tab. 6.2 and the CARE-based data of Tab. 6.6.

Table 6.8: The value of the best upper limit cross section is shown, and underneath that is the energy for GrISU-based analysis with the CARE runlist. The energies are in the units of [GeV] and the cross sections are in units of $[\mathrm{cm}^3\mathrm{s}^{-1}]$. This table should be compared to Tab. 6.2 and the CARE data in Tab. 6.6.

Target	$\gamma\gamma$	$\tau^+\tau^-$	$b\bar{b}$	W^+W^-	Z^0Z^0
Segue 1	$2.94 \cdot 10^{-24}$	$3.51 \cdot 10^{-22}$	$4.69 \cdot 10^{-21}$	$2.42 \cdot 10^{-21}$	$3.16 \cdot 10^{-21}$
	266	1059	2113	1059	1189
Ursa Minor	$4.74 \cdot 10^{-24}$	$6.79 \cdot 10^{-22}$	$9.32 \cdot 10^{-21}$	$1.58 \cdot 10^{-21}$	$6.29 \cdot 10^{-21}$
	3350	1059	1884	1189	1189
Stacked	$2.02 \cdot 10^{-24}$	$2.27 \cdot 10^{-22}$	$3.24 \cdot 10^{-21}$	$1.55 \cdot 10^{-21}$	$2.05 \cdot 10^{-21}$
	237	1059	1884	1189	1189

Tab. 6.7 and 6.8 show that the new CARE-based analysis is preferable to GrISU-based analysis. This can also be seen in Fig. 6.29-6.33. The first three figures are for single targets and should be compared to Fig. 6.1-6.19.

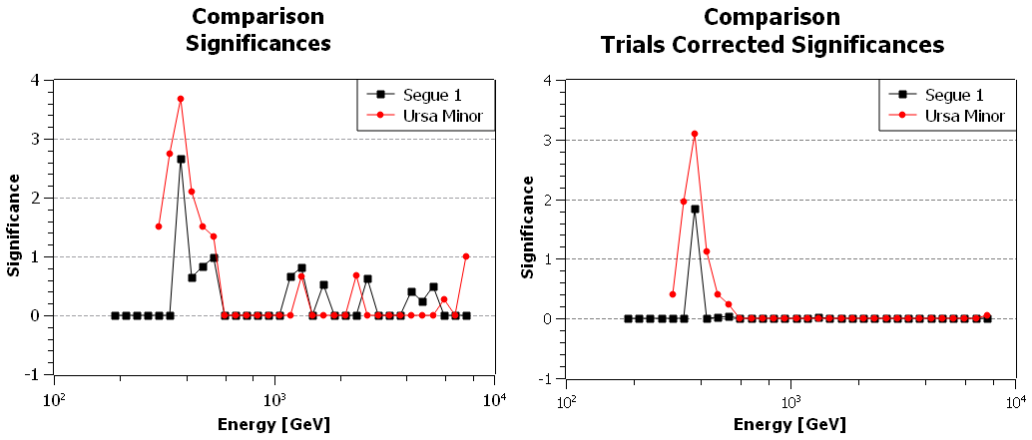

Figure 6.29: Line significances using GrISU-based analysis with the CARE runlist for Segue 1 and Ursa Minor. Before and after trials correction, left and right figure respectively.

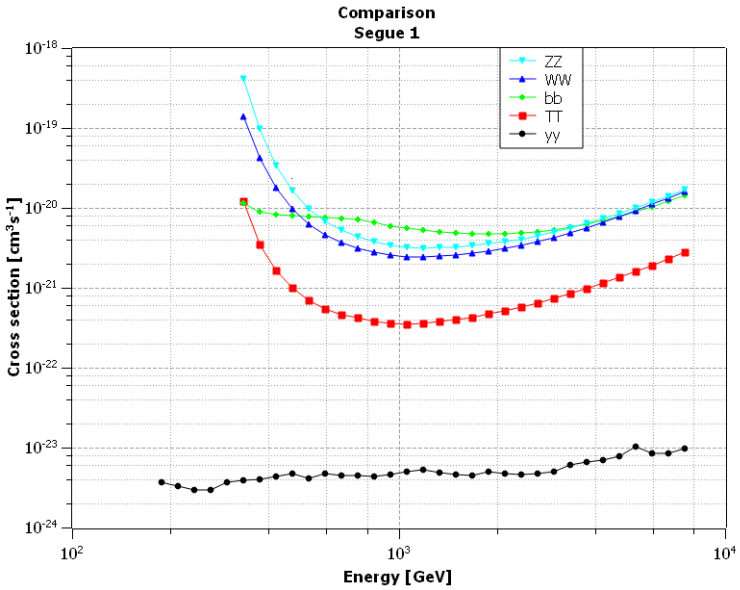

Figure 6.30: Segue 1 upper limit cross sections using GrISU-based analysis with the CARE runlist.

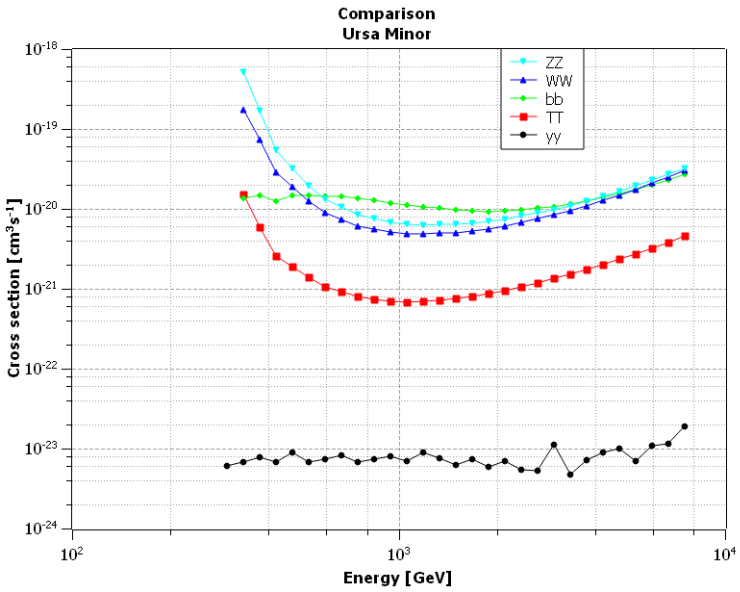

Figure 6.31: Ursa Minor upper limit cross sections using GrISU-based analysis with the CARE runlist.

Fig. 6.32-6.33, are for the comparison between CARE- and GrISU-based stacked analysis.

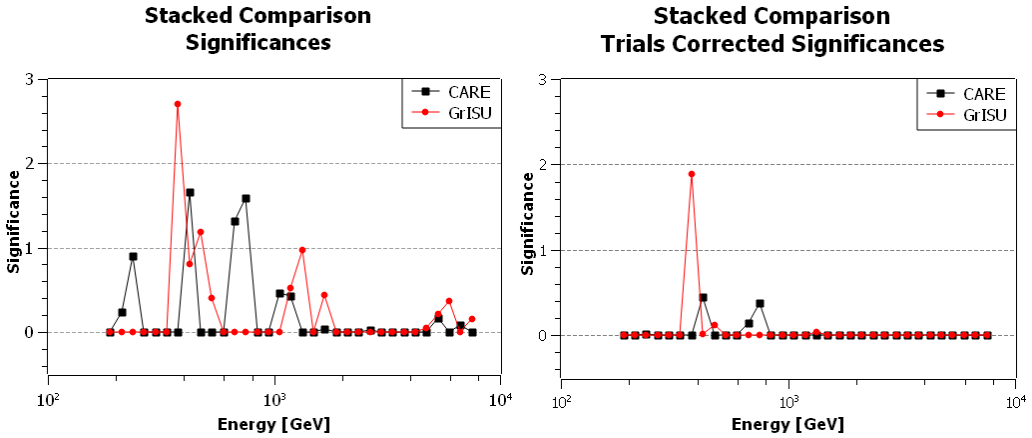

Figure 6.32: Line significances when using CARE- and GrISU-based stacked analysis with the CARE runlist. Before and after trials correction, left and right figure respectively.

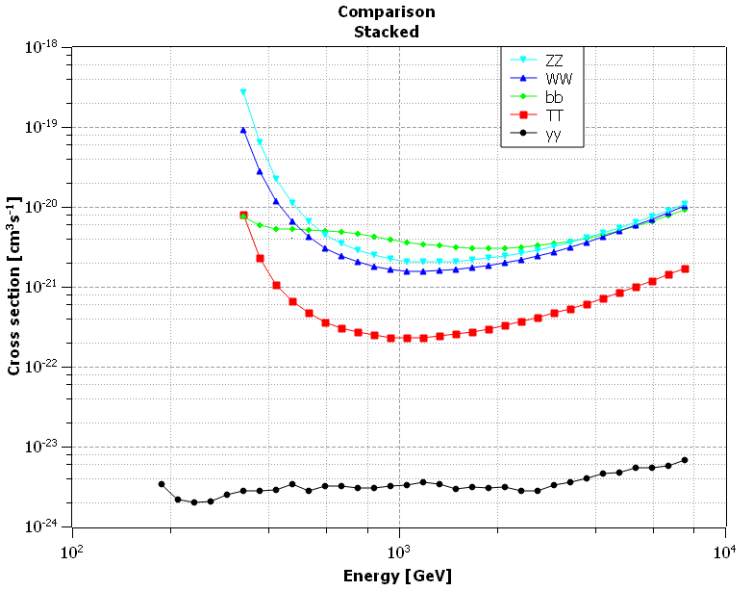

Figure 6.33: Stacked upper limit cross sections using GrISU-based analysis with the CARE runlist.

6.4 Results Summary

The speed to computational effort ratio of the 3D-model method with 3D-energy is better than that of the standard analysis. The energy threshold, effective area and bias correction have also all been improved. The energy resolution has not been improved and is comparable to standard analysis. CARE performs better than GrISU taking into account the amount of data available. Stacking the data shows an improvement in analysis outcome. The line search clearly functions although the significance of the lines does not allow for any positive detection claim. It is also clear that the 3D-model with 3D-energy is optimised for DM searches. Neither the Crab nor M87 are DM targets, which can be seen in the results when analysing them.

Chapter 7

Conclusions and Discussion

In this chapter, the conclusions made from the results will be presented and discussed.

7.1 3D-energy vs. Standard Analysis

The differences seen in the Crab flux, in Sec. 6.1, can be explained with the focus that has been placed on improving energy resolution and bias below 10 TeV. The cuts made effectively cut out most of the flux from higher energies. For the GrISU-based analysis, this resulted in a decline in the effective area that starts slightly below 10 TeV, as seen in Fig. 6.8. The bias-correction done at the lowest energies, lowers the energy below where the fit is performed. There will thus be proportionally less flux at the lowest fitted energies with the 3D-energy in comparison to standard analysis. This flattens the power law fit, making the slope less negative. It is important to keep in mind that the analysis used in Fig. 6.2 was done with standard cuts. These cuts are made for Crab-like spectra. The cuts made for the 3D-energy, which are the equivalent of soft cuts, are not made for Crab-like spectra.

7.2 CARE or GrISU

CARE-based analysis has been shown to be better in every important way in comparison to GrISU-based analysis, i.e effective area, energy bias, energy resolution, energy threshold and shower recreation capabilities. This is because there is more higher quality CARE-based simulations available, which results in larger effective areas and finer energy resolution. This leads to improved upper limit cross sections. Thus, the CARE-based analysis is preferred for future use.

7.3 Implications of the Line Search Results

As was shown in the previous chapter, no significant DM line signature has been found. As such, the words "line/lines" will be used when referring to heightened significance values over at most two energy bins.

The line with the highest significance for a single target was found in the Ursa Minor CARE-based analysis. It is at an energy of 422 GeV with an upper limit cross section of $8.10 \cdot 10^{-24}\text{cm}^3\text{s}^{-1}$ and has a significance of 2.73σ before trials correction and 1.56σ after. A line was also found at 422 GeV in the CARE-based stacked analysis. It has an upper limit cross section of $2.92 \cdot 10^{-24}\text{cm}^3\text{s}^{-1}$ and a significance of 1.66σ before trials correction and 0.55σ after.

For GrISU-based analysis on single targets, the highest significance was found in Segue 1 at 473 GeV with $1.43\sigma/1.30 \cdot 10^{-3}\sigma$ before and after trials correction respectively. The upper limit cross section for that energy was $1.34 \cdot 10^{-25}\text{cm}^3\text{s}^{-1}$. The strongest line in the GrISU-based stacked analysis was at the same energy. The significance was $0.72\sigma/1.66 \cdot 10^{-3}\sigma$ before and after trials correction respectively, with an upper limit cross section of $6.11 \cdot 10^{-26}\text{cm}^3\text{s}^{-1}$.

Lines are seen in two adjacent energy bins for the two closest DM sources, i.e. Segue 1 and Willman 1. These are the sources with the highest mass to light ratios. The line in Willman 1 is at 376 GeV.

The line with the highest significance was seen in the GrISU-based analysis using the CARE data set analysing Ursa Minor, at 376 GeV. The significance was $3.68\sigma/3.10\sigma$ before and after trials correction respectively. The highest significance lines that were found in the comparison analysis of Segue 1 and the stacked data were also at 376 GeV.

The strongest line significances are all within the range $422 \pm 15\%$ GeV, where the energy resolution is $\sim 20\%$. There is, however, no indication of a line in this energy range in the full GrISU-based analysis of Boötes, Draco or Ursa Minor. In this range in the stacked GrISU-based analysis, with the lowest upper limit cross section of $6.11 \cdot 10^{-26}\text{cm}^3\text{s}^{-1}$, it is the strongest indication of a line signal. However, no positive detection of a line can be claimed, due to the low significance. This was expected since the analysis bottleneck is almost completely due to computational limits and the amount of data analysed.
The fact that no significant line was seen, but 1-3 were expected, is an indication that the uncertainty was overestimated. With the number of independent search regions per target being ~ 10, it was expected to see roughly one line that has a significance $> 1\sigma$ caused by random chance after trial correction. This was only seen in the stacked analysis and comparison analysis. Even though the GrISU-based analysis of the CARE runlist gave higher significances to the lines, the cross sections were lower, seen in Fig. 6.29 in comparison to Fig. 6.17 and Fig. 6.18-6.19 in comparison to Fig. 6.30-6.31, implying that the lines were just random fluctuations.

Internal VERITAS work, [76], suggested that only slight improvements to the upper limit cross sections and line significances were possibly achievable.

7.4 Understanding the Upper Limit Results

Comparing the results in this thesis with published results from VERITAS, specifically [76], the results are in line with the current limits. Most results are within one sigma. The differences can be accounted for by the choice of θ^2 and that the parameter cuts were different.

As expected, the upper limits improved with larger quantities of data. However, internal VERITAS notes have shown that this is not always the case, where 96 hours of data have generated stronger limits than 216 hours of data during analysis. This might be due to how the data is handled in the different methods. The data is almost on the same level as the noise fluctuations in the data, which can introduce more noise than useful data when introducing more data, thus the upper limits become worse. Also allowing that lower quality data be included in the analysis in a larger data set, can reduce the final result quality. For the 3D-energy the J-factor is weighted in on an event-by-event basis which is not the case for the standard analysis. Another possible reason

can be small variations in what is cut. In the search for DM, even a small improvement in what gets cut is important, due to the on-source data photon flux being on a similar level as the off-source background photon flux.

The GrISU-based stacked analysis has already crossed into the $10^{-26}\text{cm}^3\text{s}^{-1}$ cross section range with the value $6.11 \cdot 10^{-26}\text{cm}^3\text{s}^{-1}$ for $\gamma\gamma$ annihilation. The CARE-based analysis shows on average $\sim 30\%$ lower cross section values than that of GrISU-based analysis. Thus, naively, just switching to CARE-based analysis with the same amount of data should reduce the upper limit to $\sim 4.37 \cdot 10^{-26}\text{cm}^3\text{s}^{-1}$. Under the standard assumption that the upper limit follows the root of the amount of data, to reach cross sections below $\sim 3 \cdot 10^{-26}\text{cm}^3\text{s}^{-1}$, 2-3 times the data amount is needed. One possible option to get below $\sim 3 \cdot 10^{-26}\text{cm}^3\text{s}^{-1}$ is to combine data with other telescopes arrays, e.g. MAGIC and HESS, assuming they have the same amount of clean data as VERITAS. Another option is that CTA could observe the needed amount of data within just a few years, based on the specifications of CTA and the amount of quality observing time of VERITAS.

7.5 Implications to General Physics

No new part of WIMP parameter space has been excluded, only confirmation of what is already excluded by other studies. With more data, a DM line will likely be found. Finding a DM line, that is generated by one of the theorised WIMPs, will bring new insights into which extended particle physics model more accurately describes reality. Knowing the energy of one WIMP will give a general scale of where other possible WIMPs can be found. Particle accelerators, e.g. the Large Hadron Collider, can confirm the findings, since the WIMPs should be detectable to it. DM theories need to be re-evaluated if no DM line is found when cross sections below $\sim 3 \cdot 10^{-26}\text{cm}^3\text{s}^{-1}$ are reached.

New technologies and methods have been created and advanced during the development of CTA, e.g. the cameras that will be used. These technologies and methods will reach other parts of society and the general public, and will in some way, enhance everyday life.

7.6 Improvements to the 3D-energy

Improvements have been made to the analysis. There are however still other possible improvements that could be added.

7.6.1 Effective Areas

Removing the upper edge cuts on parameters, e.g. the number of expected Cherenkov photons, could increase the effective area and extend analysis range above 10 TeV.
Another possible improvement is to have individually chosen θ^2 cuts, which are optimised for each individual target. In comparison to the chosen θ^2 cut of 0.013 steradians, most of the targets have a larger angular size. This would result in a higher number of photons in the on- and off-regions, larger effective areas and larger J-factors. Looking at Eq. 2.9, the results should improve, because the ratio of photons in the on- versus off-regions should grow slower than the J-factors multiplied with the integrated effective area and the simulated photon count. An even better way would be to completely remove the θ^2 box cut in favour of dynamically computing a cut during analysis, which however results in a much different way of calculating the effective area files, as these are dependent on the θ^2 cut.

7.6.2 On- and Off-regions

Another improvement that can be made is to use another method for choosing the on- and off-regions. The reflected-regions method that has been used during this work is not optimised for DM searches. A more suitable way to choose the on- and off-regions is to use the crescent moon method, see [76]. Considering that this method, when using the standard energy reconstruction, produces similar results to the 3D-energy reconstruction, it is a likely that using the 3D-energy together with the crescent moon method would further improve current results since each method is an improvement on different parts of the DM analysis previously used.

7.6.3 Box Cuts

The chosen box cuts for the 3D-energy are dependent on elevation, noise, time of year, and which telescope configuration is being used. These have all been tested and the current cuts, which have been rigorously tested, seem to be close to optimal. This is corroborated by the fact that even small changes to the cuts reduces the overall quality. This could, however, likely be improved slightly using BDTs. As BDT analysis is now being implemented as an advanced analysis method in Eventdisplay, it should only be a matter of implementing the 3D-model parameters to that method. This can, however, a very time-consuming process.

A different approach of getting the energy from shower parameters is to use neural networks for learning which energy belongs to which set of shower parameters. The understanding of how neural network can be used has advanced considerably the last few years and might provide other useful techniques than the direct application as well. Using neural networks has been discussed within VERITAS.

7.7 Dark Matter with CTA and Other Arrays

7.7.1 CTA

One of the early layouts for the southern CTA site included 5 LSTs. This would have been the most optimal outcome for DM searches. Now 4 LSTs are planned, which is still going to contribute greatly to DM searches. The low energy search, where a DM line is most likely, would have greatly benefited from the improved effective area granted by a fifth LST.

A rough estimate of future possibilities with CTA in a DM search, based on the results of this, is of some interest. Assuming that the same type of data which was used in this thesis gets captured with CTA, it is possible to estimate what type of upper limits would be reached. Fig. 7.1 shows the expected effective area of CTA for 0.5, 5, and 50 hours of data:

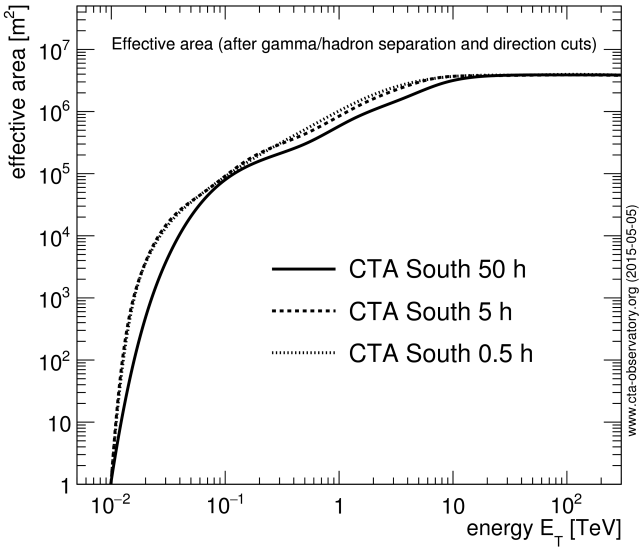

Figure 7.1: Effective area plot for CTA South after gamma/hadron separation and directional cuts. The figure is taken from [31].

This is on average 10-15 times larger than the effective area used to get the 3D-energy in this thesis. The same concept can be seen in Fig. 3.7, that CTA has a flux sensitivity that will be approximately 10-15 times better than VERITAS. Fig. 3.7 and 7.1 represent analysis that uses cuts equivalent to standard cuts with VERITAS. With the slight improvements that have been made, scaling with the lowest value is not directly representable, but in making a conservative estimate, a factor 10 will be used. The most competitive single target upper limits were achieved when analysing Segue 1. Dividing the upper limit cross sections with the factor 10 shows that $\gamma\gamma$ crosses the $3 \cdot 10^{-}26$ cm^{3}s^{-1} level and becomes $8.56 \cdot 10^{-27}$ cm^{3}s^{-1}, and that $\tau^+\tau^-$ not yet close at $4.93 \cdot 10^{-25}$ cm^{3}s^{-1}.

For the stacked analysis, the values for $\gamma\gamma$ and $\tau^+\tau^-$ becomes $5.21 \cdot 10^{-27}$ cm^{3}s^{-1} and $3.34 \cdot 10^{-25}$ cm^{3}s^{-1} respectively. Even with the $\sim 30\%$ improvement going from GrISU- to CARE-based analysis, the $\tau^+\tau^-$ would not get below the $3 \cdot 10^{-}26$ cm^{3}s^{-1} level. To bring $\tau^+\tau^-$ down below the $3 \cdot 10^{-}26$ cm^{3}s^{-1} level, would require approximately 8-16 times the existing data volume. This is somewhere between 1800-3600 hours of DM search oriented data, which would be 2-5 years if CTA only focused on DM.

7.7.2 Dark Matter Array

It has been hinted at, during collaboration meetings and astrophysical summer schools, that a DM array is being considered, possibly if CTA performs well on the DM front. The current baseline concept is an array of some tens of telescopes approximately of LST size. This would naturally continue to push any upper limit down from where CTA is competitive. Alternatively, the DM array should be able to give more precise and detailed data to improve the analysis quality of DM searches than CTA. Speculating on the possible results of a DM array is meaningless with data from VERITAS, as the system and analysis will most likely be completely different.

7.7.3 Final Remarks and Summary

The 3D-energy performs well compared to the current best analysis methods within VERITAS. The bias correction and effective areas have been slightly improved upon in comparison to standard analysis. WIMP upper limit cross sections are within the error margins of previous analysis. No DM line has been seen at any significant level. It has been shown that the CARE package is preferable to the GrISU package, because it improves on all the important points such as effective area and energy resolution. For further DM searches, the 3D-model with 3D-energy will be a good tool. However, improvements can still be made. With more work, the 3D-model with the 3D-energy will also be a useful tool for non-DM searches. Given enough data, it should be possible, even likely, for the CTA to detect DM due to its improved capabilities in comparison to current telescopes.

Chapter 8

Acknowledgements

I give thanks to the following people for all the help, hints, tips and support I have gotten throughout my PhD-work. First, to my professor for giving me the chance to do my PhD and sending me around the world to attend many fascinating meetings. Thanks to Gareth Hughes and Roman Welsing at DESY Zeuthen, for helping me understand the analysis system. Thanks to Jens Ruppel and Volkmar Wieland at the university of Potsdam, for general help with getting everything to work with living in Germany. Also at Potsdam university, Clemens Hoischen, thanks for the help with ROOT. Big thanks to the people in Gernot Maiers group, for helping with all sorts of problems, both small and large, Henrike Fleischhack, Maria Krause, Moritz Hütten and especially Nathan Kelley-Hoskins. For making the long days a bit more fun at work, thank you Kathrin Mallot. Thanks across the pond to Jeff Grube and Bret McArthur for working on the 3D-model and ideas regarding 3D-energy. Thanks also across the pond to Benjamin Zitzer, for general knowledge on DM searches. Gratitude also goes to Alina Wilhelm and Karsten Berger for making observations at VERITAS really fun. Last, and most importantly, I would like to thank Anne Fox and my father, Gert Håkansson, for all the support shown.
If anyone was forgotten, as I always say "You know I am not good with remembering names!".

Bibliography

[1] G. Aad, T. Abajyan, B. Abbott, J. Abdallah, S. Abdel Khalek, A. A. Abdelalim, O. Abdinov, R. Aben, B. Abi, M. Abolins, and et al. Observation of a new particle in the search for the Standard Model Higgs boson with the ATLAS detector at the LHC. *Physics Letters B*, 716: 1–29, September 2012. doi: 10.1016/j.physletb.2012.08.020.

[2] A. A. Abdo, M. Ackermann, M. Ajello, W. B. Atwood, L. Baldini, J. Ballet, G. Barbiellini, D. Bastieri, K. Bechtol, R. Bellazzini, B. Berenji, E. D. Bloom, E. Bonamente, A. W. Borgland, A. Bouvier, J. Bregeon, A. Brez, M. Brigida, P. Bruel, T. H. Burnett, S. Buson, G. A. Caliandro, R. A. Cameron, P. A. Caraveo, S. Carrigan, J. M. Casandjian, C. Cecchi, Ö. Çelik, A. Chekhtman, J. Chiang, S. Ciprini, R. Claus, J. Cohen-Tanugi, J. Conrad, C. D. Dermer, A. de Angelis, F. de Palma, S. W. Digel, E. Do Couto E Silva, P. S. Drell, A. Drlica-Wagner, R. Dubois, D. Dumora, Y. Edmonds, R. Essig, C. Farnier, C. Favuzzi, S. J. Fegan, W. B. Focke, P. Fortin, M. Frailis, Y. Fukazawa, S. Funk, P. Fusco, F. Gargano, D. Gasparrini, N. Gehrels, S. Germani, N. Giglietto, F. Giordano, T. Glanzman, G. Godfrey, I. A. Grenier, J. E. Grove, L. Guillemot, S. Guiriec, M. Gustafsson, D. Hadasch, A. K. Harding, D. Horan, R. E. Hughes, M. S. Jackson, G. Jóhannesson, A. S. Johnson, R. P. Johnson, W. N. Johnson, T. Kamae, H. Katagiri, J. Kataoka, N. Kawai, M. Kerr, J. Knödlseder, M. Kuss, J. Lande, L. Latronico, M. Llena Garde, F. Longo, F. Loparco, B. Lott, M. N. Lovellette, P. Lubrano, A. Makeev, M. N. Mazziotta, J. E. McEnery, C. Meurer, P. F. Michelson, W. Mitthumsiri, T. Mizuno, A. A. Moiseev, C. Monte, M. E. Monzani, A. Morselli, I. V. Moskalenko, S. Murgia, P. L. Nolan, J. P. Norris, E. Nuss, T. Ohsugi, N. Omodei, E. Orlando, J. F. Ormes, M. Ozaki, D. Paneque, J. H. Panetta, D. Parent, V. Pelassa, M. Pepe, M. Pesce-Rollins, F. Piron, S. Rainò, R. Rando, M. Razzano, A. Reimer, O. Reimer, T. Reposeur, J. Ripken, S. Ritz,

A. Y. Rodriguez, M. Roth, H. F.-W. Sadrozinski, A. Sander, P. M. S. Parkinson, J. D. Scargle, T. L. Schalk, A. Sellerholm, C. Sgrò, E. J. Siskind, D. A. Smith, P. D. Smith, G. Spandre, P. Spinelli, J.-L. Starck, M. S. Strickman, D. J. Suson, H. Tajima, H. Takahashi, T. Tanaka, J. B. Thayer, J. G. Thayer, L. Tibaldo, D. F. Torres, Y. Uchiyama, T. L. Usher, V. Vasileiou, N. Vilchez, V. Vitale, A. P. Waite, P. Wang, B. L. Winer, K. S. Wood, T. Ylinen, M. Ziegler, and Fermi LAT Collaboration. Fermi Large Area Telescope Search for Photon Lines from 30 to 200 GeV and Dark Matter Implications. *Physical Review Letters*, 104(9):091302, March 2010. doi: 10.1103/PhysRevLett.104.091302.

[3] V. A. Acciari, T. Arlen, T. Aune, M. Beilicke, W. Benbow, D. Boltuch, S. M. Bradbury, J. H. Buckley, V. Bugaev, K. Byrum, A. Cannon, A. Cesarini, J. L. Christiansen, L. Ciupik, W. Cui, R. Dickherber, C. Duke, J. P. Finley, G. Finnegan, A. Furniss, N. Galante, S. Godambe, J. Grube, R. Guenette, G. Gyuk, D. Hanna, J. Holder, C. M. Hui, T. B. Humensky, A. Imran, P. Kaaret, N. Karlsson, M. Kertzman, D. Kieda, A. Konopelko, H. Krawczynski, F. Krennrich, G. Maier, S. McArthur, A. McCann, M. McCutcheon, P. Moriarty, R. A. Ong, A. N. Otte, D. Pandel, J. S. Perkins, M. Pohl, J. Quinn, K. Ragan, L. C. Reyes, P. T. Reynolds, E. Roache, H. J. Rose, M. Schroedter, G. H. Sembroski, G. D. Senturk, A. W. Smith, D. Steele, S. P. Swordy, G. Tešić, M. Theiling, S. Thibadeau, A. Varlotta, V. V. Vassiliev, S. Vincent, R. G. Wagner, S. P. Wakely, J. E. Ward, T. C. Weekes, A. Weinstein, T. Weisgarber, D. A. Williams, S. Wissel, B. Zitzer, and VERITAS Collaboration. VERITAS Search for VHE Gamma-ray Emission from Dwarf Spheroidal Galaxies. *ApJ*, 720:1174–1180, September 2010. doi: 10.1088/0004-637X/720/2/1174.

[4] B. S. Acharya, M. Actis, T. Aghajani, G. Agnetta, J. Aguilar, F. Aharonian, M. Ajello, A. Akhperjanian, M. Alcubierre, J. Aleksić, and et al. Introducing the CTA concept. *Astroparticle Physics*, 43:3–18, March 2013. doi: 10.1016/j.astropartphys.2013.01.007.

[5] M. Actis, G. Agnetta, F. Aharonian, A. Akhperjanian, J. Aleksić, E. Aliu, D. Allan, I. Allekotte, F. Antico, L. A. Antonelli, and et al. Design concepts for the Cherenkov Telescope Array CTA: an advanced facility for ground-based high-energy gamma-ray astronomy. *Experimental Astronomy*, 32:193–316, December 2011. doi: 10.1007/s10686-011-9247-0.

[6] F. Aharonian, A. G. Akhperjanian, A. R. Bazer-Bachi, M. Beilicke, W. Benbow, D. Berge, K. Bernlöhr, C. Boisson, O. Bolz, V. Borrel, I. Braun, F. Breitling, A. M. Brown, R. Bühler, S. Carrigan, P. M. Chadwick, L.-M. Chounet, R. Cornils, L. Costamante, B. Degrange, H. J. Dickinson, A. Djannati-Ataï, L. O'C. Drury, G. Dubus, K. Egberts, D. Emmanoulopoulos, P. Espigat, F. Feinstein, G. Fontaine, S. Funk, Y. A. Gallant, B. Giebels, J. F. Glicenstein, P. Goret, C. Hadjichristidis, D. Hauser, M. Hauser, G. Heinzelmann, G. Henri, G. Hermann, J. A. Hinton, W. Hofmann, M. Holleran, D. Horns, A. Jacholkowska, O. C. de Jager, B. Khélifi, N. Komin, A. Konopelko, I. J. Latham, R. Le Gallou, A. Lemière, M. Lemoine-Goumard, T. Lohse, J. M. Martin, O. Martineau-Huynh, A. Marcowith, C. Masterson, T. J. L. McComb, M. de Naurois, D. Nedbal, S. J. Nolan, A. Noutsos, K. J. Orford, J. L. Osborne, M. Ouchrif, M. Panter, G. Pelletier, S. Pita, G. Pühlhofer, M. Punch, B. C. Raubenheimer, M. Raue, S. M. Rayner, A. Reimer, O. Reimer, J. Ripken, L. Rob, L. Rolland, G. Rowell, V. Sahakian, L. Saugé, S. Schlenker, R. Schlickeiser, C. Schuster, U. Schwanke, M. Siewert, H. Sol, D. Spangler, R. Steenkamp, C. Stegmann, G. Superina, J.-P. Tavernet, R. Terrier, C. G. Théoret, M. Tluczykont, C. van Eldik, G. Vasileiadis, C. Venter, P. Vincent, H. J. Völk, S. J. Wagner, and M. Ward. Evidence for VHE γ-ray emission from the distant BL Lac PG 1553+113. *A&A*, 448:L19–L23, March 2006. doi: 10.1051/0004-6361:200600010.

[7] E. Aliu, S. Archambault, T. Arlen, T. Aune, M. Beilicke, W. Benbow, A. Bouvier, S. M. Bradbury, J. H. Buckley, V. Bugaev, K. Byrum, A. Cannon, A. Cesarini, J. L. Christiansen, L. Ciupik, E. Collins-Hughes, M. P. Connolly, W. Cui, G. Decerprit, R. Dickherber, J. Dumm, M. Errando, A. Falcone, Q. Feng, F. Ferrer, J. P. Finley, G. Finnegan, L. Fortson, A. Furniss, N. Galante, D. Gall, S. Godambe, S. Griffin, J. Grube, G. Gyuk, D. Hanna, J. Holder, H. Huan, G. Hughes, T. B. Humensky, P. Kaaret, N. Karlsson, M. Kertzman, Y. Khassen, D. Kieda, H. Krawczynski, F. Krennrich, K. Lee, A. S. Madhavan, G. Maier, P. Majumdar, S. McArthur, A. McCann, P. Moriarty, R. Mukherjee, R. A. Ong, M. Orr, A. N. Otte, N. Park, J. S. Perkins, M. Pohl, H. Prokoph, J. Quinn, K. Ragan, L. C. Reyes, P. T. Reynolds, E. Roache, H. J. Rose, J. Ruppel, D. B. Saxon, M. Schroedter, G. H. Sembroski, G. D. Şentürk, C. Skole, A. W. Smith, D. Staszak, I. Telezhinsky, G. Tešić, M. Theiling, S. Thibadeau, K. Tsurusaki, A. Varlotta, V. V. Vassiliev, S. Vincent,

M. Vivier, R. G. Wagner, S. P. Wakely, J. E. Ward, T. C. Weekes, A. Weinstein, T. Weisgarber, D. A. Williams, and B. Zitzer. VERITAS deep observations of the dwarf spheroidal galaxy Segue 1. *PRD*, 85(6): 062001, March 2012. doi: 10.1103/PhysRevD.85.062001.

[8] S. Ando. Gamma-ray background anisotropy from Galactic dark matter substructure. *PRD*, 80(2):023520, July 2009. doi: 10.1103/PhysRevD.80.023520.

[9] CTA Argentina. About Cherenkov radiation, 2010. URL `http://astrum.frm.utn.edu.ar/CTA-Argentina/?p=1001`. Visited on 01.03.2014.

[10] A. N. Baushev, S. Federici, and M. Pohl. Spectral analysis of the gamma-ray background near the dwarf Milky Way satellite Segue 1: Improved limits on the cross section of neutralino dark matter annihilation. *PRD*, 86(6):063521, September 2012. doi: 10.1103/PhysRevD.86.063521.

[11] M. Beilicke and VERITAS Collaboration. VERITAS observations of M87 in 2011/2012. In F. A. Aharonian, W. Hofmann, and F. M. Rieger, editors, *American Institute of Physics Conference Series*, volume 1505 of *American Institute of Physics Conference Series*, pages 586–589, December 2012. doi: 10.1063/1.4772328.

[12] L. Bergström. Dark matter evidence, particle physics candidates and detection methods. *Annalen der Physik*, 524:479–496, October 2012. doi: 10.1002/andp.201200116.

[13] L. Bergstrom. Saas-Fee Lecture Notes: Multi-messenger Astronomy and Dark Matter. *ArXiv e-prints*, February 2012.

[14] L. Bergström. Multi-Messenger Astronomy and Dark Matter. *Astrophysics at Very High Energies, Saas-Fee Advanced Course, Volume 40. ISBN 978-3-642-36133-3. Springer-Verlag Berlin Heidelberg, 2013, p. 123*, 40: 123, 2013. doi: 10.1007/978-3-642-36134-0_2.

[15] L. Bergström and H. Snellman. Observable monochromatic photons from cosmic photino annihilation. *PRD*, 37:3737–3741, June 1988. doi: 10.1103/PhysRevD.37.3737.

[16] L. Bergström, P. Ullio, and J. H. Buckley. Observability of γ rays from dark matter neutralino annihilations in the Milky Way halo. *Astroparticle Physics*, 9:137–162, August 1998. doi: 10.1016/S0927-6505(98)00015-2.

[17] K. Bernlöhr. Atmospheric Cherenkov light. URL `https://www.mpi-hd.mpg.de/hfm/CosmicRay/ChLight/Cherenkov.html`. Visited on 02.08.2014.

[18] G. Bertone, D. Hooper, and J. Silk. Particle dark matter: evidence, candidates and constraints. *PhysRep*, 405:279–390, January 2005. doi: 10.1016/j.physrep.2004.08.031.

[19] I. I. Bigi and A. I. Sanda. *Basics of CP violation*, page 269. Cambridge University Press, 2009.

[20] V. Bonnivard, C. Combet, M. Daniel, S. Funk, A. Geringer-Sameth, J. A. Hinton, D. Maurin, J. I. Read, S. Sarkar, M. G. Walker, and M. I. Wilkinson. Dark matter annihilation and decay in dwarf spheroidal galaxies: The classical and ultrafaint dSphs. *ArXiv e-prints*, April 2015.

[21] T. Bringmann, M. Doro, and M. Fornasa. Dark matter signals from Draco and Willman 1: prospects for MAGIC II and CTA. *JCAP*, 1:016, January 2009. doi: 10.1088/1475-7516/2009/01/016.

[22] T. Bringmann, X. Huang, A. Ibarra, S. Vogl, and C. Weniger. Fermi LAT search for internal bremsstrahlung signatures from dark matter annihilation. *JCAP*, 7:054, July 2012. doi: 10.1088/1475-7516/2012/07/054.

[23] J. A. R. Cembranos, A. de La Cruz-Dombriz, A. Dobado, R. A. Lineros, and A. L. Maroto. Photon spectra from WIMP annihilation. *PRD*, 83 (8):083507, April 2011. doi: 10.1103/PhysRevD.83.083507.

[24] A. Charbonnier, C. Combet, M. Daniel, S. Funk, J. A. Hinton, D. Maurin, C. Power, J. I. Read, S. Sarkar, M. G. Walker, and M. I. Wilkinson. Dark matter profiles and annihilation in dwarf spheroidal galaxies: prospectives for present and future γ-ray observatories - I. The classical dwarf spheroidal galaxies. *MNRAS*, 418:1526–1556, December 2011. doi: 10.1111/j.1365-2966.2011.19387.x.

[25] S. Chatrchyan, V. Khachatryan, A. M. Sirunyan, A. Tumasyan, W. Adam, E. Aguilo, T. Bergauer, M. Dragicevic, J. Erö, C. Fabjan, and et al. Observation of a new boson at a mass of 125 GeV with the CMS experiment at the LHC. *Physics Letters B*, 716:30–61, September 2012. doi: 10.1016/j.physletb.2012.08.021.

[26] V. R. Chitnis and P. N. Bhat. Čerenkov photon density fluctuations in extensive air showers. *Astroparticle Physics*, 9:45–63, June 1998. doi: 10.1016/S0927-6505(98)00007-3.

[27] David B. Cline. *Proceedings of the 1st International Symposium on Sources of Dark Matter in the Universe : 16-18 February 1994, Bel Air, California*. World Scientific Pub Co Inc, March 1995.

[28] D. Clowe, M. Bradač, A. H. Gonzalez, M. Markevitch, S. W. Randall, C. Jones, and D. Zaritsky. A Direct Empirical Proof of the Existence of Dark Matter. *ApjL*, 648:L109–L113, September 2006. doi: 10.1086/508162.

[29] VERITAS Collaboration. About VERITAS, 2011. URL `http://veritas.sao.arizona.edu/about-veritas-mainmenu-81/veritas-specifications-mainmenu-111`. Visited on 14.05.2016.

[30] VERITAS Collaboration. VERITAS preformance, internal pages, 2015. URL `https://veritas.sao.arizona.edu/wiki/index.php/Performance_Paper#ED`. Visited on 03.03.2016.

[31] CTA community. CTA Preformance, 2014. URL `https://portal.cta-observatory.org/Pages/CTA-Performance.aspx`. Visited on 02.05.2016.

[32] A. Coogan, S. Profumo, and W. Shepherd. Monochromatic gamma rays from dark matter annihilation to leptons. *Journal of High Energy Physics*, 8:74, August 2015. doi: 10.1007/JHEP08(2015)074.

[33] D. B. Kieda for the VERITAS Collaboration. The Gamma Ray Detection sensitivity of the upgraded VERITAS Observatory. *ArXiv e-prints*, August 2013.

[34] D. Das, U. Ellwanger, and P. Mitropoulos. A 130 GeV photon line from dark matter annihilation in the NMSSM. *JCAP*, 8:003, August 2012. doi: 10.1088/1475-7516/2012/08/003.

[35] DESY. Graphics, Animation and FAQ Video Clips of the CTA Project, 2015. URL `http://astro.desy.de/gamma_astronomy/cta/media/about_cta/index_eng.htm`. Visited on 07.09.2015.

[36] L. D. Duffy and K. van Bibber. Axions as dark matter particles. *New Journal of Physics*, 11(10):105008, October 2009. doi: 10.1088/1367-2630/11/10/105008.

[37] C. Amsler et al. (Particle Data Group). . *Physics Letters B667*, 2008.

[38] S. Funk, J. A. Hinton, and CTA Consortium. Comparison of Fermi-LAT and CTA in the region between 10-100 GeV. *Astroparticle Physics*, 43: 348–355, March 2013. doi: 10.1016/j.astropartphys.2012.05.018.

[39] A. Geringer-Sameth, S. M. Koushiappas, and M. Walker. Dwarf Galaxy Annihilation and Decay Emission Profiles for Dark Matter Experiments. *ApJ*, 801:74, March 2015. doi: 10.1088/0004-637X/801/2/74.

[40] E. Gross and O. Vitells. Trial factors for the look elsewhere effect in high energy physics. *European Physical Journal C*, 70:525–530, November 2010. doi: 10.1140/epjc/s10052-010-1470-8.

[41] J. Grube and B. McArthur. Model 3D Analysis, January 2015.

[42] D. Heck, J. Knapp, J. N. Capdevielle, G. Schatz, and T. Thouw. *CORSIKA: a Monte Carlo code to simulate extensive air showers.* February 1998.

[43] H.E.S.S. Collaboration, A. Abramowski, F. Acero, F. Aharonian, A. G. Akhperjanian, G. Anton, A. Barnacka, U. Barres de Almeida, A. R. Bazer-Bachi, Y. Becherini, J. Becker, B. Behera, K. Bernlöhr, A. Bochow, C. Boisson, J. Bolmont, P. Bordas, V. Borrel, J. Brucker, F. Brun, P. Brun, T. Bulik, I. Büsching, S. Carrigan, S. Casanova, M. Cerruti, P. M. Chadwick, A. Charbonnier, R. C. G. Chaves, A. Cheesebrough, L.-M. Chounet, A. C. Clapson, G. Coignet, J. Conrad, M. Dalton, M. K. Daniel, I. D. Davids, B. Degrange, C. Deil, H. J. Dickinson, A. Djannati-Ataï, W. Domainko, L. O. C. Drury, F. Dubois, G. Dubus, J. Dyks, M. Dyrda,

K. Egberts, P. Eger, P. Espigat, L. Fallon, C. Farnier, S. Fegan, F. Feinstein, M. V. Fernandes, A. Fiasson, G. Fontaine, A. Förster, M. Füßling, Y. A. Gallant, H. Gast, L. Gérard, D. Gerbig, B. Giebels, J. F. Glicenstein, B. Glück, P. Goret, D. Göring, J. D. Hague, D. Hampf, M. Hauser, S. Heinz, G. Heinzelmann, G. Henri, G. Hermann, J. A. Hinton, A. Hoffmann, W. Hofmann, P. Hofverberg, D. Horns, A. Jacholkowska, O. C. de Jager, C. Jahn, M. Jamrozy, I. Jung, M. A. Kastendieck, K. Katarzyński, U. Katz, S. Kaufmann, D. Keogh, M. Kerschhaggl, D. Khangulyan, B. Khélifi, D. Klochkov, W. Kluźniak, T. Kneiske, N. Komin, K. Kosack, R. Kossakowski, H. Laffon, G. Lamanna, D. Lennarz, T. Lohse, A. Lopatin, C.-C. Lu, V. Marandon, A. Marcowith, J. Masbou, D. Maurin, N. Maxted, T. J. L. McComb, M. C. Medina, J. Méhault, R. Moderski, E. Moulin, C. L. Naumann, M. Naumann-Godo, M. de Naurois, D. Nedbal, D. Nekrassov, N. Nguyen, B. Nicholas, J. Niemiec, S. J. Nolan, S. Ohm, J.-F. Olive, E. de Oña Wilhelmi, B. Opitz, M. Ostrowski, M. Panter, M. Paz Arribas, G. Pedaletti, G. Pelletier, P.-O. Petrucci, S. Pita, G. Pühlhofer, M. Punch, A. Quirrenbach, M. Raue, S. M. Rayner, A. Reimer, O. Reimer, M. Renaud, R. de Los Reyes, F. Rieger, J. Ripken, L. Rob, S. Rosier-Lees, G. Rowell, B. Rudak, C. B. Rulten, J. Ruppel, F. Ryde, V. Sahakian, A. Santangelo, R. Schlickeiser, F. M. Schöck, A. Schönwald, U. Schwanke, S. Schwarzburg, S. Schwemmer, A. Shalchi, M. Sikora, J. L. Skilton, H. Sol, G. Spengler, Ł. Stawarz, R. Steenkamp, C. Stegmann, F. Stinzing, I. Sushch, A. Szostek, J.-P. Tavernet, R. Terrier, O. Tibolla, M. Tluczykont, K. Valerius, C. van Eldik, G. Vasileiadis, C. Venter, J. P. Vialle, A. Viana, P. Vincent, M. Vivier, H. J. Völk, F. Volpe, S. Vorobiov, M. Vorster, S. J. Wagner, M. Ward, A. Wierzcholska, A. Zajczyk, A. A. Zdziarski, A. Zech, H.-S. Zechlin, and H.E.S.S. Collaboration. H.E.S.S. constraints on dark matter annihilations towards the sculptor and carina dwarf galaxies. *Astroparticle Physics*, 34:608–616, March 2011. doi: 10.1016/j.astropartphys.2010.12.006.

[44] A. M. Hillas. Cerenkov light images of EAS produced by primary gamma. *International Cosmic Ray Conference*, 3:445–448, August 1985.

[45] Kevin Meagher for the VERITAS Collaboration. Six years of VERITAS observations of the Crab Nebula. *ArXiv e-prints*, August 2015.

[46] E. Komatsu, K. M. Smith, J. Dunkley, C. L. Bennett, B. Gold, G. Hinshaw, N. Jarosik, D. Larson, M. R. Nolta, L. Page, D. N.

Spergel, M. Halpern, R. S. Hill, A. Kogut, M. Limon, S. S. Meyer, N. Odegard, G. S. Tucker, J. L. Weiland, E. Wollack, and E. L. Wright. Seven-year Wilkinson Microwave Anisotropy Probe (WMAP) Observations: Cosmological Interpretation. *ApJS*, 192:18, February 2011. doi: 10.1088/0067-0049/192/2/18.

[47] M. Lemoine-Goumard, B. Degrange, and M. Tluczykont. Selection and 3D-reconstruction of gamma-ray-induced air showers with a stereoscopic system of atmospheric Cherenkov telescopes. *Astroparticle Physics*, 25: 195–211, April 2006. doi: 10.1016/j.astropartphys.2006.01.005.

[48] G. Lemson and t. Virgo Consortium. Halo and Galaxy Formation Histories from the Millennium Simulation: Public release of a VO-oriented and SQL-queryable database for studying the evolution of galaxies in the LambdaCDM cosmogony. *ArXiv Astrophysics e-prints*, August 2006.

[49] J. D. Lykken. Beyond the Standard Model. *ArXiv e-prints*, May 2010.

[50] G. D. Mack, T. D. Jacques, J. F. Beacom, N. F. Bell, and H. Yüksel. Conservative constraints on dark matter annihilation into gamma rays. *PRD*, 78(6):063542, September 2008. doi: 10.1103/PhysRevD.78.063542.

[51] G. Maier. Methods and Implementation 5: Background models and sky maps, January 2014.

[52] NASA. FERMI, 2008. URL `http://www.nasa.gov/mission_pages/GLAST/multimedia/glast_rendering.html`. Visited on 16.05.2014.

[53] R. J. Nemiroff and B. Patla. Adventures in Friedmann cosmology: A detailed expansion of the cosmological Friedmann equations. *American Journal of Physics*, 76:265–276, March 2008. doi: 10.1119/1.2830536.

[54] A. Nepomuk Otte and for the VERITAS collaboration. Upgrade of the VERITAS Cherenkov Telescope Array. *ArXiv e-prints*, July 2009.

[55] N. Park and for the VERITAS Collaboration. Performance of the VERITAS experiment. *ArXiv e-prints*, August 2015.

[56] L. Pieri, J. Lavalle, G. Bertone, and E. Branchini. Implications of high-resolution simulations on indirect dark matter searches. *PRD*, 83(2): 023518, January 2011. doi: 10.1103/PhysRevD.83.023518.

[57] N. P. Pitjev and E. V. Pitjeva. Constraints on dark matter in the solar system. *Astronomy Letters*, 39:141–149, March 2013. doi: 10.1134/S1063773713020060.

[58] Z. Qi. Reflector Simulation program for an imaging air Cherenkov telescope, 2007. ISRN: LTU-PB-EX–08/079–SE (2008:079).

[59] K. Ragan. VERITAS areal view after 2009 move, 2011. URL `http://www.physics.mcgill.ca/gallery/ken2`. Visited on 04.06.2013.

[60] M. Regis and P. Ullio. Testing the dark matter interpretation of the PAMELA excess through measurements of the galactic diffuse emission. *PRD*, 80(4):043525, August 2009. doi: 10.1103/PhysRevD.80.043525.

[61] Brant E. Robertson and Andrew R. Zentner. Dark matter annihilation rates with velocity-dependent annihilation cross sections. *Phys. Rev. D*, 79:083525, Apr 2009. doi: 10.1103/PhysRevD.79.083525. URL `http://link.aps.org/doi/10.1103/PhysRevD.79.083525`.

[62] ScienceDaily. VERITAS areal view before 2009 move, 2007. URL `https://www.sciencedaily.com/releases/2007/05/070501142342.htm`. Visited on 04.06.2013.

[63] Scitechdaily. Supersymmetry, 1998. URL `http://scitechdaily.com/images/Susy-particles.jpg`. Visited on 05.06.2015.

[64] J. M. Siegal-Gaskins. Revealing dark matter substructure with anisotropies in the diffuse gamma-ray background. *JCAP*, 10:040, October 2008. doi: 10.1088/1475-7516/2008/10/040.

[65] D. N. Spergel, L. Verde, H. V. Peiris, E. Komatsu, M. R. Nolta, C. L. Bennett, M. Halpern, G. Hinshaw, N. Jarosik, A. Kogut, M. Limon, S. S. Meyer, L. Page, G. S. Tucker, J. L. Weiland, E. Wollack, and E. L. Wright. First-Year Wilkinson Microwave Anisotropy Probe (WMAP) Observations: Determination of Cosmological Parameters. *ApJS*, 148:175–194, September 2003. doi: 10.1086/377226.

[66] M. Su and D. P. Finkbeiner. Strong Evidence for Gamma-ray Line Emission from the Inner Galaxy. *ArXiv e-prints*, June 2012.

[67] H. Tajima, f. t. Fermi LAT, and Fermi GBM collaborations. Fermi Observations of high-energy gamma-ray emissions from GRB 080916C. *ArXiv e-prints*, July 2009.

[68] P. Ullio, L. Bergström, J. Edsjö, and C. Lacey. Cosmological dark matter annihilations into γ rays: A closer look. *PRD*, 66(12):123502, December 2002. doi: 10.1103/PhysRevD.66.123502.

[69] M. Vivier. *TeV gamma ray Spectra from Dark Matter Particle Annihilation and Decay*. Bartol Research Institute, University of Delaware, March 2011. Internal VERITAS note.

[70] M. Walker. *Dark Matter in the Galactic Dwarf Spheroidal Satellites*, page 1039. 2013. doi: 10.1007/978-94-007-5612-0_20.

[71] C. Weniger. Tentative observation of a gamma-ray line at the Fermi LAT. In F. A. Aharonian, W. Hofmann, and F. M. Rieger, editors, *American Institute of Physics Conference Series*, volume 1505 of *American Institute of Physics Conference Series*, pages 470–473, December 2012. doi: 10.1063/1.4772299.

[72] C. Weniger. A tentative gamma-ray line from Dark Matter annihilation at the Fermi Large Area Telescope. *JCAP*, 8:007, August 2012. doi: 10.1088/1475-7516/2012/08/007.

[73] S. S. Wilks. The large-sample distribution of the likelihood ratio for testing composite hypotheses. *Ann. Math. Statist.*, 9(1):60–62, 03 1938. doi: 10.1214/aoms/1177732360. URL `http://dx.doi.org/10.1214/aoms/1177732360`.

[74] B. Willman, M. Geha, J. Strader, L. E. Strigari, J. D. Simon, E. Kirby, N. Ho, and A. Warres. Willman 1—A Probable Dwarf Galaxy with an Irregular Kinematic Distribution. *AJ*, 142:128, October 2011. doi: 10.1088/0004-6256/142/4/128.

[75] M. Wood, J. Buckley, S. Digel, S. Funk, D. Nieto, and M. A. Sanchez-Conde. Prospects for Indirect Detection of Dark Matter with CTA. *ArXiv e-prints*, May 2013.

[76] B. Zitzer and for the VERITAS Collaboration. Search for Dark Matter from Dwarf Galaxies using VERITAS. *ArXiv e-prints*, September 2015.

Appendix A

Data lists

Table A.1: DM targets data list

Date	Run #	Tel.ver./Atm.	Simtype	Cuts [Min]
Boötes I				
20090301	44796	4/21	GrISU	
20090301	44797	4/21	GrISU	
20090302	44828	4/21	GrISU	
20090303	44845	4/21	GrISU	
20090303	44846	4/21	GrISU	
20090303	44847	4/21	GrISU	
20090319	44966	4/21	GrISU	
20090319	44967	4/21	GrISU	
20090319	44968	4/21	GrISU	
20090324	45096	4/21	GrISU	
20090326	45154	4/21	GrISU	
20090326	45155	4/21	GrISU	
20090326	45156	4/21	GrISU	
20090326	45157	4/21	GrISU	
20090327	45185	4/21	GrISU	
20090327	45186	4/21	GrISU	
20090327	45187	4/21	GrISU	
20090328	45212	4/21	GrISU	
20090328	45213	4/21	GrISU	

20090328	45214	4/21	GrISU
20090328	45215	4/21	GrISU
20090328	45216	4/21	GrISU
20090328	45217	4/21	GrISU
20090331	45281	4/21	GrISU
20090331	45282	4/21	GrISU
20090331	45283	4/21	GrISU
20090331	45284	4/21	GrISU
20090331	45285	4/21	GrISU
20090401	45321	4/21	GrISU
20090401	45322	4/21	GrISU
20090402	45363	4/21	GrISU
20090402	45364	4/21	GrISU
20090402	45365	4/21	GrISU
20090403	45382	4/21	GrISU
20090403	45383	4/21	GrISU
20090403	45384	4/21	GrISU
20090417	45534	4/21	GrISU
20090418	45566	4/21	GrISU
20090418	45567	4/21	GrISU
20090419	45592	4/21	GrISU
20090419	45593	4/21	GrISU
20090419	45594	4/21	GrISU

Draco

20120513	62486	5/22	GrISU
20120513	62487	5/22	GrISU
20120513	62488	5/22	GrISU
20120513	62489	5/22	GrISU
20120513	62490	5/22	GrISU
20120513	62491	5/22	GrISU
20120513	62492	5/22	GrISU
20120514	62515	5/22	GrISU
20120514	62516	5/22	GrISU
20120514	62519	5/22	GrISU
20120516	62571	5/22	GrISU
20120516	62572	5/22	GrISU

20120519	62637	5/22	GrISU	
20120520	62662	5/22	GrISU	
20120520	62663	5/22	GrISU	
20120520	62664	5/22	GrISU	
20120520	62665	5/22	GrISU	
20120521	62692	5/22	GrISU	
20120521	62693	5/22	GrISU	
20120521	62694	5/22	GrISU	
20120522	62710	5/22	GrISU	
20120522	62711	5/22	GrISU	
20120522	62712	5/22	GrISU	
20120522	62713	5/22	GrISU	
20120523	62741	5/22	GrISU	
20120523	62744	5/22	GrISU	
20120523	62745	5/22	GrISU	X>6
20120524	62766	5/22	GrISU	
20120524	62767	5/22	GrISU	
20120524	62768	5/22	GrISU	
20120524	62769	5/22	GrISU	
20120530	62963	5/22	GrISU	
20120614	63119	5/22	GrISU	X<14
20120614	63120	5/22	GrISU	X<7
20120614	63121	5/22	GrISU	
20120614	63125	5/22	GrISU	
20120614	63128	5/22	GrISU	3<X<7
20120616	63160	5/22	GrISU	X<14
20120616	63161	5/22	GrISU	X<11
20120616	63163	5/22	GrISU	
20120616	63164	5/22	GrISU	9.5<X<13
20120616	63165	5/22	GrISU	
20120617	63182	5/22	GrISU	
20120617	63183	5/22	GrISU	
20120618	63202	5/22	GrISU	
20120618	63204	5/22	GrISU	
20120618	63205	5/22	GrISU	12<X<13.5
20120619	63237	5/22	GrISU	
20120619	63238	5/22	GrISU	
20120619	63239	5/22	GrISU	

20120620	63257	5/22	GrISU	
20120620	63258	5/22	GrISU	
20120620	63259	5/22	GrISU	
20120621	63284	5/22	GrISU	
20120621	63286	5/22	GrISU	
20120621	63287	5/22	GrISU	
20120622	63305	5/22	GrISU	
20120622	63306	5/22	GrISU	
20120623	63327	5/22	GrISU	
20120623	63328	5/22	GrISU	
20120623	63329	5/22	GrISU	
20130507	68349	6/22	GrISU	
20130511	68644	6/22	GrISU	
20130511	68645	6/22	GrISU	
20130513	68682	6/22	GrISU	
20130513	68683	6/22	GrISU	
20130515	68724	6/22	GrISU	
20130515	68725	6/22	GrISU	
20130515	68726	6/22	GrISU	
20130516	68744	6/22	GrISU	
20130519	68803	6/22	GrISU	
20130519	68804	6/22	GrISU	
20130520	68817	6/22	GrISU	
20130520	68819	6/22	GrISU	
20130521	68833	6/22	GrISU	
20130521	68834	6/22	GrISU	
20130601	68921	6/22	GrISU	
20130602	68940	6/22	GrISU	
20130607	69032	6/22	GrISU	
20130607	69033	6/22	GrISU	
20130608	69048	6/22	GrISU	0<X<3
				13<X<15
				27<X<30
20130609	69064	6/22	GrISU	
20130611	69095	6/22	GrISU	
20130611	69096	6/22	GrISU	
20130611	69097	6/22	GrISU	
20130615	69163	6/22	GrISU	X<3

20130615	69165	6/22	GrISU	
20130616	69184	6/22	GrISU	

Segue 1

20091211	48865	5/21	GrISU	
20091211	48866	5/21	GrISU	X>4
20091225	49201	5/21	GrISU	
20091225	49202	5/21	GrISU	X>8
20091226	49215	5/21	GrISU	
20091226	49216	5/21	GrISU	
20091226	49218	5/21	GrISU	
20100110	49413	5/21	GrISU	X<1
20100112	49482	5/21	GrISU	
20100112	49483	5/21	GrISU	
20100112	49484	5/21	GrISU	
20100112	49485	5/21	GrISU	
20100112	49486	5/21	GrISU	
20100112	49487	5/21	GrISU	
20100115	49579	5/21	GrISU	
20100115	49581	5/21	GrISU	
20100115	49582	5/21	GrISU	
20100115	49583	5/21	GrISU	
20100115	49584	5/21	GrISU	
20100115	49585	5/21	GrISU	
20100115	49586	5/21	GrISU	
20100117	49651	5/21	GrISU	X<9
20100117	49652	5/21	GrISU	X>12
20100117	49653	5/21	GrISU	X>10
20100117	49654	5/21	GrISU	X>16
20100117	49655	5/21	GrISU	
20100117	49656	5/21	GrISU	X>10
20100124	49726	5/21	GrISU	
20100124	49727	5/21	GrISU	
20100125	49739	5/21	GrISU	X<10
20100125	49740	5/21	GrISU	
20100208	49854	5/21	GrISU	
20100208	49855	5/21	GrISU	X<8

20100208	49862	5/21	GrISU	
20100209	49881	5/21	GrISU	
20100209	49882	5/21	GrISU	
20100209	49883	5/21	GrISU	X<1
20100209	49884	5/21	GrISU	
20100209	49885	5/21	GrISU	
20100210	49918	5/21	GrISU	
20100210	49920	5/21	GrISU	
20100210	49921	5/21	GrISU	
20100210	49922	5/21	GrISU	
20100210	49923	5/21	GrISU	
20100210	49924	5/21	GrISU	
20100210	49925	5/21	GrISU	X>14
20100210	49926	5/21	GrISU	
20100214	50007	5/21	GrISU	
20100214	50008	5/21	GrISU	
20100214	50009	5/21	GrISU	
20100215	50036	5/21	GrISU	
20100215	50037	5/21	GrISU	
20100215	50038	5/21	GrISU	
20100215	50039	5/21	GrISU	
20100216	50068	5/21	GrISU	
20100216	50069	5/21	GrISU	
20100216	50070	5/21	GrISU	
20100216	50071	5/21	GrISU	
20100219	50150	5/21	GrISU	
20100219	50151	5/21	GrISU	
20100219	50152	5/21	GrISU	
20100220	50182	5/21	GrISU	
20100305	50229	5/21	GrISU	
20100310	50263	5/21	GrISU	
20100310	50264	5/21	GrISU	
20100312	50317	5/21	GrISU	
20100312	50323	5/21	GrISU	
20100312	50324	5/21	GrISU	
20100313	50355	5/21	GrISU	
20100313	50356	5/21	GrISU	
20100314	50387	5/21	GrISU	

20100315	50414	5/21	GrISU	
20100315	50415	5/21	GrISU	
20100316	50465	5/21	GrISU	
20100317	50490	5/21	GrISU	
20100317	50491	5/21	GrISU	
20100317	50492	5/21	GrISU	X<10
				X>17
20100317	50493	5/21	GrISU	X<3
				X>13
20100317	50494	5/21	GrISU	
20100317	50495	5/21	GrISU	13<X<16
20100317	50496	5/21	GrISU	
20100318	50536	5/21	GrISU	
20100318	50537	5/21	GrISU	
20100318	50538	5/21	GrISU	
20100318	50539	5/21	GrISU	
20110130	54696	5/21	GrISU	
20110130	54697	5/21	GrISU	
20110130	54698	5/21	GrISU	
20110212	55064	5/21	GrISU	
20110212	55065	5/21	GrISU	
20110226	55204	5/21	GrISU	
20110226	55205	5/21	GrISU	X<10
20110226	55206	5/21	GrISU	X<13
20110228	55225	5/21	GrISU	
20110228	55226	5/21	GrISU	
20110228	55227	5/21	GrISU	
20110228	55228	5/21	GrISU	
20110228	55229	5/21	GrISU	
20110301	55251	5/21	GrISU	
20110302	55280	5/21	GrISU	
20110302	55281	5/21	GrISU	
20110302	55282	5/21	GrISU	
20110304	55339	5/21	GrISU	
20110304	55341	5/21	GrISU	
20110304	55342	5/21	GrISU	
20110304	55343	5/21	GrISU	
20110305	55368	5/21	GrISU	

20110305	55369	5/21	GrISU	
20110305	55370	5/21	GrISU	11<X<13
20110305	55371	5/21	GrISU	
20110305	55372	5/21	GrISU	
20110305	55373	5/21	GrISU	
20110305	55374	5/21	GrISU	
20110305	55375	5/21	GrISU	
20110309	55474	5/21	GrISU	
20110309	55475	5/21	GrISU	
20110311	55529	5/21	GrISU	
20110311	55530	5/21	GrISU	
20110311	55531	5/21	GrISU	
20110401	55891	5/21	GrISU	
20110401	55892	5/21	GrISU	
20110401	55893	5/21	GrISU	
20110401	55894	5/21	GrISU	
20110401	55895	5/21	GrISU	
20110401	55896	5/21	GrISU	
20110403	55972	5/21	GrISU	8<X<14
20110403	55973	5/21	GrISU	X<1 X>12
20110404	55997	5/21	GrISU	
20110404	56000	5/21	GrISU	
20110405	56025	5/21	GrISU	
20110405	56026	5/21	GrISU	
20110405	56028	5/21	GrISU	
20110405	56029	5/21	GrISU	
20110424	56250	5/22	GrISU	
20110426	56287	5/22	GrISU	
20110426	56288	5/22	GrISU	
20110426	56289	5/22	GrISU	
20110427	56316	5/22	GrISU	
20110428	56354	5/22	GrISU	
20110428	56355	5/22	GrISU	
20110428	56356	5/22	GrISU	
20110429	56379	5/22	GrISU	
20110429	56382	5/22	GrISU	
20110501	56472	5/22	GrISU	

20110501	56473	5/22	GrISU	
20110502	56504	5/22	GrISU	
20110502	56505	5/22	GrISU	
20110502	56506	5/22	GrISU	
20110503	56529	5/22	GrISU	
20110503	56530	5/22	GrISU	
20110522	56730	5/22	GrISU	
20111221	59272	5/21	GrISU	
20111221	59273	5/21	GrISU	
20111222	59299	5/21	GrISU	
20111222	59300	5/21	GrISU	
20111223	59328	5/21	GrISU	X>12
20111224	59352	5/21	GrISU	
20111224	59359	5/21	GrISU	
20111224	59360	5/21	GrISU	
20111225	59394	5/21	GrISU	
20111225	59395	5/21	GrISU	X>18
20111226	59428	5/21	GrISU	
20111226	59429	5/21	GrISU	
20111226	59430	5/21	GrISU	X>12
20111227	59462	5/21	GrISU	
20111227	59465	5/21	GrISU	
20111228	59498	5/21	GrISU	
20111228	59501	5/21	GrISU	
20111228	59502	5/21	GrISU	
20111228	59503	5/21	GrISU	
20111228	59504	5/21	GrISU	
20111229	59535	5/21	GrISU	
20111229	59537	5/21	GrISU	
20111229	59538	5/21	GrISU	
20111229	59539	5/21	GrISU	
20111229	59540	5/21	GrISU	
20111230	59575	5/21	GrISU	
20111230	59576	5/21	GrISU	
20111230	59577	5/21	GrISU	
20111230	59578	5/21	GrISU	
20111231	59605	5/21	GrISU	
20111231	59606	5/21	GrISU	

20111231	59607	5/21	GrISU	
20111231	59608	5/21	GrISU	
20111231	59609	5/21	GrISU	
20111231	59610	5/21	GrISU	
20120104	59685	5/21	GrISU	
20120104	59686	5/21	GrISU	
20120104	59687	5/21	GrISU	
20120104	59688	5/21	GrISU	
20120104	59689	5/21	GrISU	
20120104	59690	5/21	GrISU	X>10
20120118	59838	5/21	GrISU	
20120118	59839	5/21	GrISU	
20120118	59840	5/21	GrISU	
20120119	59865	5/21	GrISU	
20120119	59866	5/21	GrISU	
20120119	59867	5/21	GrISU	
20120119	59870	5/21	GrISU	
20120119	59871	5/21	GrISU	
20120120	59901	5/21	GrISU	
20120120	59902	5/21	GrISU	
20120120	59903	5/21	GrISU	
20120120	59904	5/21	GrISU	
20120121	59935	5/21	GrISU	
20120121	59936	5/21	GrISU	
20120121	59937	5/21	GrISU	
20120122	59959	5/21	GrISU	
20120122	59960	5/21	GrISU	4<X<8
20120122	59961	5/21	GrISU	
20120123	59984	5/21	GrISU	
20120123	59985	5/21	GrISU	
20120123	59986	5/21	GrISU	
20120125	60024	5/21	GrISU	
20120125	60025	5/21	GrISU	
20120125	60026	5/21	GrISU	
20120125	60028	5/21	GrISU	X<3 X>9
20120125	60029	5/21	GrISU	X>16
20120126	60062	5/21	GrISU	

20120126	60063	5/21	GrISU	
20120126	60064	5/21	GrISU	
20120126	60065	5/21	GrISU	
20120126	60068	5/21	GrISU	
20120127	60095	5/21	GrISU	X<1
20120127	60096	5/21	GrISU	
20120127	60101	5/21	GrISU	
20120127	60102	5/21	GrISU	
20120127	60103	5/21	GrISU	
20120129	60170	5/21	GrISU	
20120130	60188	5/21	GrISU	
20120130	60189	5/21	GrISU	
20120130	60194	5/21	GrISU	
20120130	60195	5/21	GrISU	
20120131	60214	5/21	GrISU	X>17
20120131	60215	5/21	GrISU	3<X<5
				X>11
20120131	60216	5/21	GrISU	X<12
20120131	60217	5/21	GrISU	
20120131	60218	5/21	GrISU	4.5<X<7.5
20120201	60233	5/21	GrISU	
20120201	60234	5/21	GrISU	
20120201	60235	5/21	GrISU	
20120202	60251	5/21	GrISU	
20120215	60399	5/21	GrISU	
20120215	60400	5/21	GrISU	
20120221	60495	5/21	GrISU	
20120221	60496	5/21	GrISU	
20120221	60497	5/21	GrISU	X>6
20120321	61341	5/21	GrISU	
20120321	61342	5/21	GrISU	
20120328	61533	5/21	GrISU	
20121210	65381	5/21	GrISU	
20121210	65382	5/21	GrISU	
20121210	65383	5/21	GrISU	
20121211	65415	5/21	GrISU	
20121211	65416	5/21	GrISU	
20121212	65459	5/21	GrISU	

20121212	65460	5/21	GrISU
20121213	65486	5/21	GrISU
20121213	65487	5/21	GrISU
20130110	65962	5/21	GrISU
20130112	65989	5/21	GrISU
20130112	65990	5/21	GrISU
20130112	65991	5/21	GrISU
20130114	66057	5/21	GrISU
20130114	66058	5/21	GrISU
20130116	66125	5/21	GrISU
20130116	66126	5/21	GrISU
20130118	66185	5/21	GrISU
20130119	66204	5/21	GrISU
20130119	66205	5/21	GrISU
20130205	66565	5/21	GrISU
20130205	66566	5/21	GrISU
20130205	66567	5/21	GrISU
20130206	66586	5/21	GrISU
20130208	66632	5/21	GrISU
20130209	66649	5/21	GrISU
20130210	66668	5/21	GrISU
20130210	66669	5/21	GrISU
20130210	66670	5/21	GrISU
20130214	66799	5/21	GrISU
20130214	66800	5/21	GrISU
20130214	66801	5/21	GrISU
20130217	66903	5/21	GrISU
20130311	67259	5/21	GrISU
20130311	67260	5/21	GrISU
20130313	67298	5/21	GrISU
20130313	67301	5/21	GrISU
20130314	67338	6/21	CARE/GrISU
20130316	67424	6/21	CARE/GrISU
20130318	67468	6/21	CARE/GrISU
20130402	67650	6/21	CARE/GrISU
20130403	67672	6/21	CARE/GrISU
20130404	67720	6/21	CARE/GrISU
20130404	67721	6/21	CARE/GrISU

20130404	67722	6/21	CARE/GrISU	
20130407	67828	6/21	CARE/GrISU	
20130407	67829	6/21	CARE/GrISU	
20130410	67917	6/21	CARE/GrISU	
20130502	68244	6/22	GrISU	
20130503	68259	6/22	GrISU	
20130508	68376	6/22	GrISU	

Ursa Minor

20120223	60571	5/21	GrISU	
20120223	60572	5/21	GrISU	
20120223	60573	5/21	GrISU	
20120224	60599	5/21	GrISU	
20120224	60600	5/21	GrISU	
20120224	60601	5/21	GrISU	
20120225	60631	5/21	GrISU	
20120225	60632	5/21	GrISU	
20120225	60633	5/21	GrISU	
20120227	60695	5/21	GrISU	
20120227	60696	5/21	GrISU	
20120227	60697	5/21	GrISU	
20120227	60698	5/21	GrISU	
20120301	60808	5/21	GrISU	
20120301	60809	5/21	GrISU	
20120301	60810	5/21	GrISU	
20120301	60811	5/21	GrISU	
20120302	60861	5/21	GrISU	
20120302	60862	5/21	GrISU	
20120302	60863	5/21	GrISU	
20120302	60864	5/21	GrISU	7.5<X<9
20120303	60897	5/21	GrISU	
20120303	60898	5/21	GrISU	
20120303	60899	5/21	GrISU	
20120303	60900	5/21	GrISU	
20120316	61277	5/21	GrISU	
20120316	61278	5/21	GrISU	
20120316	61279	5/21	GrISU	

20120317	61310	5/21	GrISU
20120317	61311	5/21	GrISU
20120322	61380	5/21	GrISU
20120322	61381	5/21	GrISU
20120322	61382	5/21	GrISU
20120322	61383	5/21	GrISU
20120323	61410	5/21	GrISU
20120323	61411	5/21	GrISU
20120323	61413	5/21	GrISU
20120324	61444	5/21	GrISU
20120324	61445	5/21	GrISU
20120324	61446	5/21	GrISU
20120327	61523	5/21	GrISU
20120327	61524	5/21	GrISU
20120327	61525	5/21	GrISU
20120328	61552	5/21	GrISU
20120328	61553	5/21	GrISU
20120328	61554	5/21	GrISU
20120328	61555	5/21	GrISU
20120329	61580	5/21	GrISU
20120329	61581	5/21	GrISU
20120329	61582	5/21	GrISU
20120329	61583	5/21	GrISU
20120329	61584	5/21	GrISU
20120330	61609	5/21	GrISU
20120330	61610	5/21	GrISU
20120331	61636	5/21	GrISU
20120401	61666	5/21	GrISU
20120401	61667	5/21	GrISU
20120401	61668	5/21	GrISU
20120402	61692	5/21	GrISU
20120402	61693	5/21	GrISU
20120403	61730	5/21	GrISU
20120403	61731	5/21	GrISU
20120427	62238	5/21	GrISU
20120427	62239	5/21	GrISU
20120427	62240	5/21	GrISU
20120428	62265	5/21	GrISU

20120428	62266	5/21	GrISU	
20120428	62267	5/21	GrISU	
20120429	62290	5/21	GrISU	
20120429	62291	5/21	GrISU	
20120429	62292	5/21	GrISU	
20120430	62316	5/21	GrISU	
20120430	62317	5/21	GrISU	
20120512	62462	5/22	GrISU	
20120512	62463	5/22	GrISU	
20120512	62464	5/22	GrISU	
20120513	62480	5/22	GrISU	X>18.5
20120513	62481	5/22	GrISU	
20120513	62482	5/22	GrISU	
20120513	62483	5/22	GrISU	
20120513	62484	5/22	GrISU	
20120513	62485	5/22	GrISU	
20120514	62509	5/22	GrISU	
20120514	62510	5/22	GrISU	
20120514	62514	5/22	GrISU	X<11
20120515	62528	5/22	GrISU	
20120515	62529	5/22	GrISU	
20120515	62530	5/22	GrISU	
20120515	62532	5/22	GrISU	
20120516	62557	5/22	GrISU	
20120516	62558	5/22	GrISU	
20120516	62559	5/22	GrISU	
20120516	62560	5/22	GrISU	X>18.5
20120516	62561	5/22	GrISU	
20120516	62562	5/22	GrISU	
20120516	62563	5/22	GrISU	
20120517	62588	5/22	GrISU	
20120517	62590	5/22	GrISU	
20120518	62612	5/22	GrISU	
20120518	62613	5/22	GrISU	
20120518	62614	5/22	GrISU	
20120518	62615	5/22	GrISU	
20120518	62616	5/22	GrISU	
20130207	66617	5/21	GrISU	

20130207	66618	5/21	GrISU	
20130207	66619	5/21	GrISU	
20130317	67458	6/21	CARE/GrISU	
20130319	67499	6/21	CARE/GrISU	X>10
20130320	67518	6/21	CARE/GrISU	0<X<6
				18<X<25
20130323	67573	6/21	CARE/GrISU	
20130323	67574	6/21	CARE/GrISU	
20130324	67592	6/21	CARE/GrISU	
20130324	67593	6/21	CARE/GrISU	X>8
20130502	68252	6/22	GrISU	
20130502	68253	6/22	GrISU	
20130509	68584	6/22	GrISU	X>8
20130510	68618	6/22	GrISU	
20130512	68662	6/22	GrISU	
20130512	68663	6/22	GrISU	
20130512	68664	6/22	GrISU	
20130513	68679	6/22	GrISU	
20130513	68680	6/22	GrISU	
20130514	68696	6/22	GrISU	7<X<10
20130515	68721	6/22	GrISU	
20130516	68739	6/22	GrISU	
20130517	68762	6/22	GrISU	X>13
20130517	68763	6/22	GrISU	
20130529	68856	6/22	GrISU	
20130529	68857	6/22	GrISU	
20130530	68876	6/22	GrISU	
20130530	68877	6/22	GrISU	
20130531	68889	6/22	GrISU	
20130531	68890	6/22	GrISU	
20130531	68891	6/22	GrISU	
20130531	68892	6/22	GrISU	
20130601	68923	6/22	GrISU	
20130601	68924	6/22	GrISU	
20130602	68938	6/22	GrISU	
20130602	68939	6/22	GrISU	
20130603	68953	6/22	GrISU	
20130603	68954	6/22	GrISU	

20130604	68972	6/22	GrISU	
20130604	68973	6/22	GrISU	
20130604	68974	6/22	GrISU	
20130605	68999	6/22	GrISU	
20130605	69000	6/22	GrISU	
20130605	69001	6/22	GrISU	
20130607	69030	6/22	GrISU	
20130607	69031	6/22	GrISU	
20130608	69045	6/22	GrISU	
20130608	69047	6/22	GrISU	
20130609	69060	6/22	GrISU	
20130609	69061	6/22	GrISU	
20130609	69062	6/22	GrISU	
20130610	69079	6/22	GrISU	
20130611	69093	6/22	GrISU	
20130611	69094	6/22	GrISU	
20130613	69129	6/22	GrISU	
20130614	69145	6/22	GrISU	
20130614	69146	6/22	GrISU	
20130614	69147	6/22	GrISU	
20130614	69148	6/22	GrISU	
20130615	69162	6/22	GrISU	
20130627	69332	6/22	GrISU	X<5
20130627	69333	6/22	GrISU	

Willman 1

20071218	38468	4/21	GrISU	
20071218	38469	4/21	GrISU	
20071218	38470	4/21	GrISU	
20071218	38471	4/21	GrISU	
20071218	38472	4/21	GrISU	
20071219	38478	4/21	GrISU	
20071219	38479	4/21	GrISU	
20071219	38480	4/21	GrISU	
20071219	38481	4/21	GrISU	
20071220	38490	4/21	GrISU	
20071220	38491	4/21	GrISU	

20071220	38492	4/21	GrISU
20071220	38493	4/21	GrISU
20071220	38494	4/21	GrISU
20080110	38697	4/21	GrISU
20080110	38698	4/21	GrISU
20080110	38699	4/21	GrISU
20080111	38732	4/21	GrISU
20080111	38733	4/21	GrISU
20080111	38734	4/21	GrISU
20080111	38735	4/21	GrISU
20080111	38736	4/21	GrISU
20080112	38777	4/21	GrISU
20080114	38842	4/21	GrISU
20080114	38843	4/21	GrISU
20080114	38844	4/21	GrISU
20080114	38845	4/21	GrISU
20080114	38846	4/21	GrISU
20080115	38857	4/21	GrISU
20080115	38858	4/21	GrISU
20080115	38860	4/21	GrISU
20080131	39001	4/21	GrISU
20080131	39002	4/21	GrISU
20080131	39004	4/21	GrISU
20080202	39051	4/21	GrISU
20080202	39052	4/21	GrISU
20080203	39083	4/21	GrISU
20080203	39084	4/21	GrISU
20080203	39085	4/21	GrISU
20080207	39152	4/21	GrISU
20080207	39154	4/21	GrISU
20080207	39155	4/21	GrISU

Table A.2: Non-DM targets data list

Date	Run #	Tel.ver.	Simfile
Crab			
20131028	70314	6/22	GrISU
20131030	70351	6/22	GrISU
20131031	70373	6/22	GrISU
20131102	70458	6/22	GrISU
20131104	70482	6/21	GrISU
20131106	70530	6/22	GrISU
20131109	70604	6/22	GrISU
20131207	70997	6/21/22	CARE/GrISU
20131225	71223	6/21/22	CARE/GrISU
20140126	71802	6/21/22	CARE/GrISU
20141001	74386	6/22	GrISU
20141002	74413	6/22	GrISU
20141023	74780	6/22	GrISU
20141023	74781	6/22	GrISU
20141024	74805	6/22	GrISU
20141024	74806	6/22	GrISU
20141024	74807	6/22	GrISU
20141024	74808	6/21	GrISU
20141024	74809	6/21	GrISU
20141024	74810	6/22	GrISU
20141025	74829	6/22	GrISU
20141025	74830	6/22	GrISU
20141025	74831	6/22	GrISU
20141025	74832	6/22	GrISU
20141025	74833	6/22	GrISU
20141025	74834	6/22	GrISU
20141025	74835	6/22	GrISU
20141029	74915	6/22	GrISU

M87

20140429	73196	6/21	CARE/GrISU
20140429	73197	6/21	CARE/GrISU
20140429	73200	6/21	CARE/GrISU
20140429	73201	6/21	CARE/GrISU
20140430	73223	6/21	CARE/GrISU
20140430	73225	6/21	CARE/GrISU
20140504	73305	6/21	CARE/GrISU
20140504	73323	6/21	CARE/GrISU
20140527	73616	6/21/22	CARE/GrISU
20140527	73617	6/21/22	CARE/GrISU
20140527	73618	6/22	GrISU
20140531	73674	6/22	GrISU
20140531	73675	6/22	GrISU
20150217	76416	6/21	GrISU
20150217	76417	6/21	GrISU

Appendix B

Reference cut criteria

The cut criteria for the reference sets are dependent on the elevation. In the table *RW.* stands for reduced with, SM stands for Source Max, Nc is the number of expected Cherenkov photons in, D is Depth, Xo is the offset in X, Yo is the equivalent for Y. RWp is a term stating how much the offset was in percent from RW during the acquisition of the 3D-energy. RWe is the error in RW calculated during the 3D-model analysis. As can be seen in the table, the 80-90 degree elevation is odd. This is due to the 3D-model having problems converging when pointing toward Zenith, in practise as soon as it is more than a few degrees way it works fine. Below an elevation of 30 degrees, the 3D-model becomes less reliable, just like the other analysis methods. These are in principle box cuts that are elevation dependent. The noise in the data has very little influence, for data that is considered useful to use. Due to the nature of thesis, DM search, all the data was selected to have low noise level, thus being a non-issue for the cuts.

Table B.1: The cut values used for 3D-energy analysis.

Elevation [deg]	σ_L	σ_T	SM	Nc	RW	D	Xo	Yo	RWp	RWe
80-90	0-10	10-30	5-20	10-21	1-6	0-1000	-0.2-0.2	0-1	0.003	0.1
65-80	0-10	10-30	5-15	12-19	1-6	100-600	-1-1	-1-1	0.004	0.1
57.5-65	0-10	10-30	5-15	12-19	1-6	100-500	-1-1	-1-1	0.005	0.1
52.5-57.5	0-10	10-30	5-20	12-19	1-6	100-500	-1-1	-1-1	0.005	0.15
47.5-52.5	0-10	10-30	5-20	12-19	1-6	100-500	-1-1	-1-1	0.006	0.15
42.5-47.5	0-10	10-40	5-25	12-19	1-6	100-500	-1-1	-1-1	0.007	0.25
37.5-42.5	0-10	10-40	10-25	12-19	1.5-7	100-500	-1-1	-1-1	0.008	0.25
32.5-37.5	0-10	15-50	10-30	12-19	2-8	100-400	-1-1	-1-1	0.010	0.26
27.5-32.5	0-12	20-60	15-35	12-19	3-10	100-400	-1-1	-1-1	0.012	0.35
00-27.5	0-16	20-70	18-50	12-19	3-12	100-400	-1-1	-2-2	0.015	0.5

Appendix C

Plot values

Table C.1: DM upper-limit values for CARE-based analysis that are displayed in Fig. 6.17 and 6.19. The energy is in units of GeV and the cross sections are in units of $cm^3 s^{-1}$.

Energy	$\gamma\gamma$	$\tau\tau$	bb	WW	ZZ
Segue 1					
188.365	$3.15282 \cdot 10^{-24}$	0	0	0	0
211.349	$2.67819 \cdot 10^{-24}$	0	0	0	0
237.137	$2.97327 \cdot 10^{-24}$	0	0	0	0
266.073	$2.60202 \cdot 10^{-24}$	0	0	0	0
298.538	$2.81187 \cdot 10^{-24}$	0	0	0	0
334.965	$2.78007 \cdot 10^{-24}$	$7.54436 \cdot 10^{-21}$	$7.07872 \cdot 10^{-21}$	$8.66555 \cdot 10^{-20}$	$2.57136 \cdot 10^{-19}$
375.837	$2.68524 \cdot 10^{-24}$	$2.11713 \cdot 10^{-21}$	$5.5728 \cdot 10^{-21}$	$2.61036 \cdot 10^{-20}$	$5.97941 \cdot 10^{-20}$
421.697	$2.9904 \cdot 10^{-24}$	$1.15383 \cdot 10^{-21}$	$5.82943 \cdot 10^{-21}$	$1.27015 \cdot 10^{-20}$	$2.42316 \cdot 10^{-20}$
473.151	$2.75074 \cdot 10^{-24}$	$6.69172 \cdot 10^{-22}$	$5.35663 \cdot 10^{-21}$	$6.53924 \cdot 10^{-21}$	$1.10428 \cdot 10^{-20}$
530.884	$2.89438 \cdot 10^{-24}$	$4.52949 \cdot 10^{-22}$	$5.02435 \cdot 10^{-21}$	$4.02635 \cdot 10^{-21}$	$6.27297 \cdot 10^{-21}$
595.662	$3.18636 \cdot 10^{-24}$	$3.59801 \cdot 10^{-22}$	$4.97692 \cdot 10^{-21}$	$2.98074 \cdot 10^{-21}$	$4.401 \cdot 10^{-21}$
668.344	$3.22515 \cdot 10^{-24}$	$3.13984 \cdot 10^{-22}$	$4.9725 \cdot 10^{-21}$	$2.46823 \cdot 10^{-21}$	$3.51281 \cdot 10^{-21}$
749.894	$2.97586 \cdot 10^{-24}$	$2.91349 \cdot 10^{-22}$	$4.93311 \cdot 10^{-21}$	$2.19899 \cdot 10^{-21}$	$3.04854 \cdot 10^{-21}$
841.395	$2.83115 \cdot 10^{-24}$	$2.63093 \cdot 10^{-22}$	$4.51344 \cdot 10^{-21}$	$1.91992 \cdot 10^{-21}$	$2.60898 \cdot 10^{-21}$
944.061	$3.07242 \cdot 10^{-24}$	$2.56014 \cdot 10^{-22}$	$4.27036 \cdot 10^{-21}$	$1.81328 \cdot 10^{-21}$	$2.42387 \cdot 10^{-21}$
1,059.25	$3.04685 \cdot 10^{-24}$	$2.56932 \cdot 10^{-22}$	$4.04373 \cdot 10^{-21}$	$1.76994 \cdot 10^{-21}$	$2.33159 \cdot 10^{-21}$
1,188.50	$2.89187 \cdot 10^{-24}$	$2.62459 \cdot 10^{-22}$	$3.81992 \cdot 10^{-21}$	$1.76074 \cdot 10^{-21}$	$2.28762 \cdot 10^{-21}$
1,333.52	$2.99782 \cdot 10^{-24}$	$2.69614 \cdot 10^{-22}$	$3.58477 \cdot 10^{-21}$	$1.76328 \cdot 10^{-21}$	$2.25991 \cdot 10^{-21}$

1,496.24	$3.51669 \cdot 10^{-24}$	$2.8171 \cdot 10^{-22}$	$3.40094 \cdot 10^{-21}$	$1.79815 \cdot 10^{-21}$	$2.27316 \cdot 10^{-21}$
1,678.80	$3.22032 \cdot 10^{-24}$	$3.05619 \cdot 10^{-22}$	$3.34501 \cdot 10^{-21}$	$1.90669 \cdot 10^{-21}$	$2.37693 \cdot 10^{-21}$
1,883.65	$3.24241 \cdot 10^{-24}$	$3.31268 \cdot 10^{-22}$	$3.29317 \cdot 10^{-21}$	$2.02374 \cdot 10^{-21}$	$2.48725 \cdot 10^{-21}$
2,113.49	$3.72021 \cdot 10^{-24}$	$3.72838 \cdot 10^{-22}$	$3.38058 \cdot 10^{-21}$	$2.23533 \cdot 10^{-21}$	$2.70805 \cdot 10^{-21}$
2,371.37	$3.20255 \cdot 10^{-24}$	$4.16136 \cdot 10^{-22}$	$3.46151 \cdot 10^{-21}$	$2.4549 \cdot 10^{-21}$	$2.93133 \cdot 10^{-21}$
2,660.73	$3.43014 \cdot 10^{-24}$	$4.71872 \cdot 10^{-22}$	$3.62568 \cdot 10^{-21}$	$2.74706 \cdot 10^{-21}$	$3.23316 \cdot 10^{-21}$
2,985.38	$2.88662 \cdot 10^{-24}$	$5.38042 \cdot 10^{-22}$	$3.84735 \cdot 10^{-21}$	$3.10083 \cdot 10^{-21}$	$3.59769 \cdot 10^{-21}$
3,349.65	$3.22132 \cdot 10^{-24}$	$6.1827 \cdot 10^{-22}$	$4.14636 \cdot 10^{-21}$	$3.53916 \cdot 10^{-21}$	$4.04882 \cdot 10^{-21}$
3,758.37	$3.28924 \cdot 10^{-24}$	$7.16623 \cdot 10^{-22}$	$4.54248 \cdot 10^{-21}$	$4.08823 \cdot 10^{-21}$	$4.61298 \cdot 10^{-21}$
4,216.97	$3.54227 \cdot 10^{-24}$	$8.35694 \cdot 10^{-22}$	$5.04492 \cdot 10^{-21}$	$4.76725 \cdot 10^{-21}$	$5.30749 \cdot 10^{-21}$
4,731.51	$3.44341 \cdot 10^{-24}$	$9.78573 \cdot 10^{-22}$	$5.6673 \cdot 10^{-21}$	$5.60037 \cdot 10^{-21}$	$6.15451 \cdot 10^{-21}$
5,308.84	$3.07414 \cdot 10^{-24}$	$1.1531 \cdot 10^{-21}$	$6.45163 \cdot 10^{-21}$	$6.64212 \cdot 10^{-21}$	$7.20825 \cdot 10^{-21}$
5,956.62	$3.54467 \cdot 10^{-24}$	$1.36897 \cdot 10^{-21}$	$7.449 \cdot 10^{-21}$	$7.96213 \cdot 10^{-21}$	$8.53689 \cdot 10^{-21}$
6,683.44	$3.51519 \cdot 10^{-24}$	$1.63287 \cdot 10^{-21}$	$8.695 \cdot 10^{-21}$	$9.61796 \cdot 10^{-21}$	$1.0193 \cdot 10^{-20}$
7,498.94	$2.96038 \cdot 10^{-24}$	$1.95259 \cdot 10^{-21}$	$1.02352 \cdot 10^{-20}$	$1.16818 \cdot 10^{-20}$	$1.22428 \cdot 10^{-20}$

Ursa Minor

375.837	$7.44 \cdot 10^{-24}$	$1.36 \cdot 10^{-21}$	$3.34 \cdot 10^{-21}$	$1.69 \cdot 10^{-20}$	$3.92 \cdot 10^{-20}$
421.697	$8.1 \cdot 10^{-24}$	$1.96 \cdot 10^{-21}$	$9.14 \cdot 10^{-21}$	$2.21 \cdot 10^{-20}$	$4.27 \cdot 10^{-20}$
473.151	$6.67 \cdot 10^{-24}$	$1.18 \cdot 10^{-21}$	$8.73 \cdot 10^{-21}$	$1.19 \cdot 10^{-20}$	$2.04 \cdot 10^{-20}$
530.884	$6.45 \cdot 10^{-24}$	$9.99 \cdot 10^{-22}$	$1.04 \cdot 10^{-20}$	$9.29 \cdot 10^{-21}$	$1.47 \cdot 10^{-20}$
595.662	$6.02 \cdot 10^{-24}$	$8.05 \cdot 10^{-22}$	$1.06 \cdot 10^{-20}$	$7.02 \cdot 10^{-21}$	$1.05 \cdot 10^{-20}$
668.344	$6.12 \cdot 10^{-24}$	$7.15 \cdot 10^{-22}$	$1.11 \cdot 10^{-20}$	$5.95 \cdot 10^{-21}$	$8.549 \cdot 10^{-21}$
749.894	$5.26 \cdot 10^{-24}$	$6.29 \cdot 10^{-22}$	$1.07 \cdot 10^{-20}$	$5.06 \cdot 10^{-21}$	$7.07 \cdot 10^{-21}$
841.395	$5.13 \cdot 10^{-24}$	$5.54 \cdot 10^{-22}$	$9.77 \cdot 10^{-21}$	$4.33 \cdot 10^{-21}$	$5.93 \cdot 10^{-21}$
944.061	$4.78 \cdot 10^{-24}$	$5.1 \cdot 10^{-22}$	$8.96 \cdot 10^{-21}$	$3.89 \cdot 10^{-21}$	$5.24 \cdot 10^{-21}$
1,059.25	$5.19 \cdot 10^{-24}$	$5.16 \cdot 10^{-22}$	$8.76 \cdot 10^{-21}$	$3.86 \cdot 10^{-21}$	$5.13 \cdot 10^{-21}$
1,188.50	$4.43 \cdot 10^{-24}$	$5.2 \cdot 10^{-22}$	$8.35 \cdot 10^{-21}$	$3.83 \cdot 10^{-21}$	$5.01 \cdot 10^{-21}$
1,333.52	$4.04 \cdot 10^{-24}$	$5.21 \cdot 10^{-22}$	$7.8 \cdot 10^{-21}$	$3.77 \cdot 10^{-21}$	$4.86 \cdot 10^{-21}$
1,496.24	$3.98 \cdot 10^{-24}$	$5.41 \cdot 10^{-22}$	$7.50 \cdot 10^{-21}$	$3.86 \cdot 10^{-21}$	$4.92 \cdot 10^{-21}$
1,678.80	$4.39 \cdot 10^{-24}$	$5.67 \cdot 10^{-22}$	$7.25 \cdot 10^{-21}$	$3.99 \cdot 10^{-21}$	$5.02 \cdot 10^{-21}$
1,883.65	$4.31 \cdot 10^{-24}$	$6.1 \cdot 10^{-22}$	$7.19 \cdot 10^{-21}$	$4.25 \cdot 10^{-21}$	$5.27 \cdot 10^{-21}$
2,113.49	$5.23 \cdot 10^{-24}$	$6.59 \cdot 10^{-22}$	$7.18 \cdot 10^{-21}$	$4.54 \cdot 10^{-21}$	$5.56 \cdot 10^{-21}$
2,371.37	$5.36 \cdot 10^{-24}$	$7.17 \cdot 10^{-22}$	$7.26 \cdot 10^{-21}$	$4.91 \cdot 10^{-21}$	$5.93 \cdot 10^{-21}$
2,660.73	$4.43 \cdot 10^{-24}$	$7.9 \cdot 10^{-22}$	$7.46 \cdot 10^{-21}$	$5.38 \cdot 10^{-21}$	$6.41 \cdot 10^{-21}$
2,985.38	$4.34 \cdot 10^{-24}$	$8.79 \cdot 10^{-22}$	$7.809 \cdot 10^{-21}$	$5.98 \cdot 10^{-21}$	$7.03 \cdot 10^{-21}$
3,349.65	$4.65 \cdot 10^{-24}$	$9.95 \cdot 10^{-22}$	$8.359 \cdot 10^{-21}$	$6.78 \cdot 10^{-21}$	$7.85 \cdot 10^{-21}$

3,758.37	$4.45 \cdot 10^{-24}$	$1.13 \cdot 10^{-21}$	$9.03 \cdot 10^{-21}$	$7.72 \cdot 10^{-21}$	$8.82 \cdot 10^{-21}$
4,216.97	$5.77 \cdot 10^{-24}$	$1.29 \cdot 10^{-21}$	$9.90 \cdot 10^{-21}$	$8.89 \cdot 10^{-21}$	$9.99 \cdot 10^{-21}$
4,731.51	$5.99 \cdot 10^{-24}$	$1.49 \cdot 10^{-21}$	$1.1 \cdot 10^{-20}$	$1.03 \cdot 10^{-20}$	$1.15 \cdot 10^{-20}$
5,308.84	$7.81 \cdot 10^{-24}$	$1.74 \cdot 10^{-21}$	$1.25 \cdot 10^{-20}$	$1.22 \cdot 10^{-20}$	$1.35 \cdot 10^{-20}$
5,956.62	$6.22 \cdot 10^{-24}$	$2.04 \cdot 10^{-21}$	$1.43 \cdot 10^{-20}$	$1.46 \cdot 10^{-20}$	$1.58 \cdot 10^{-20}$
6,683.44	$5.66 \cdot 10^{-24}$	$2.39 \cdot 10^{-21}$	$1.65 \cdot 10^{-20}$	$1.74 \cdot 10^{-20}$	$1.87 \cdot 10^{-20}$
7,498.94	$3.51 \cdot 10^{-24}$	$2.82 \cdot 10^{-21}$	$1.92 \cdot 10^{-20}$	$2.09 \cdot 10^{-20}$	$2.22 \cdot 10^{-20}$

Stacked

188.365	$4.87 \cdot 10^{-24}$	0	0	0	0
211.349	$4.08 \cdot 10^{-24}$	0	0	0	0
237.137	$4.43 \cdot 10^{-24}$	0	0	0	0
266.073	$2.92 \cdot 10^{-24}$	0	0	0	0
298.538	$2.79 \cdot 10^{-24}$	0	0	0	0
334.965	$2.75 \cdot 10^{-24}$	$6.15 \cdot 10^{-21}$	$5.77 \cdot 10^{-21}$	$7.06 \cdot 10^{-20}$	$2.1 \cdot 10^{-19}$
375.837	$2.63 \cdot 10^{-24}$	$1.72 \cdot 10^{-21}$	$4.51 \cdot 10^{-21}$	$2.12 \cdot 10^{-20}$	$4.85 \cdot 10^{-20}$
421.697	$2.92 \cdot 10^{-24}$	$9.6 \cdot 10^{-22}$	$4.82 \cdot 10^{-21}$	$1.06 \cdot 10^{-20}$	$2.02 \cdot 10^{-20}$
473.151	$2.66 \cdot 10^{-24}$	$5.54 \cdot 10^{-22}$	$4.38 \cdot 10^{-21}$	$5.43 \cdot 10^{-21}$	$9.18 \cdot 10^{-21}$
530.884	$2.66 \cdot 10^{-24}$	$3.8 \cdot 10^{-22}$	$4.15 \cdot 10^{-21}$	$3.39 \cdot 10^{-21}$	$5.3 \cdot 10^{-21}$
595.662	$2.81 \cdot 10^{-24}$	$3 \cdot 10^{-22}$	$4.1 \cdot 10^{-21}$	$2.5 \cdot 10^{-21}$	$3.71 \cdot 10^{-21}$
668.344	$2.82 \cdot 10^{-24}$	$2.6 \cdot 10^{-22}$	$4.09 \cdot 10^{-21}$	$2.07 \cdot 10^{-21}$	$2.95 \cdot 10^{-21}$
749.894	$2.55 \cdot 10^{-24}$	$2.37 \cdot 10^{-22}$	$4 \cdot 10^{-21}$	$1.81 \cdot 10^{-21}$	$2.51 \cdot 10^{-21}$
841.395	$2.46 \cdot 10^{-24}$	$2.13 \cdot 10^{-22}$	$3.67 \cdot 10^{-21}$	$1.58 \cdot 10^{-21}$	$2.15 \cdot 10^{-21}$
944.061	$2.42 \cdot 10^{-24}$	$2.03 \cdot 10^{-22}$	$3.42 \cdot 10^{-21}$	$1.46 \cdot 10^{-21}$	$1.96 \cdot 10^{-21}$
1,059.25	$2.58 \cdot 10^{-24}$	$2.03 \cdot 10^{-22}$	$3.24 \cdot 10^{-21}$	$1.42 \cdot 10^{-21}$	$1.88 \cdot 10^{-21}$
1,188.50	$2.37 \cdot 10^{-24}$	$2.05 \cdot 10^{-22}$	$3.06 \cdot 10^{-21}$	$1.41 \cdot 10^{-21}$	$1.84 \cdot 10^{-21}$
1,333.52	$2.4 \cdot 10^{-24}$	$2.09 \cdot 10^{-22}$	$2.86 \cdot 10^{-21}$	$1.4 \cdot 10^{-21}$	$1.8 \cdot 10^{-21}$
1,496.24	$2.61 \cdot 10^{-24}$	$2.17 \cdot 10^{-22}$	$2.71 \cdot 10^{-21}$	$1.43 \cdot 10^{-21}$	$1.81 \cdot 10^{-21}$
1,678.80	$2.49 \cdot 10^{-24}$	$2.33 \cdot 10^{-22}$	$2.66 \cdot 10^{-21}$	$1.5 \cdot 10^{-21}$	$1.88 \cdot 10^{-21}$
1,883.65	$2.51 \cdot 10^{-24}$	$2.52 \cdot 10^{-22}$	$2.62 \cdot 10^{-21}$	$1.6 \cdot 10^{-21}$	$1.97 \cdot 10^{-21}$
2,113.49	$2.87 \cdot 10^{-24}$	$2.8 \cdot 10^{-22}$	$2.67 \cdot 10^{-21}$	$1.75 \cdot 10^{-21}$	$2.12 \cdot 10^{-21}$
2,371.37	$2.66 \cdot 10^{-24}$	$3.09 \cdot 10^{-22}$	$2.72 \cdot 10^{-21}$	$1.91 \cdot 10^{-21}$	$2.28 \cdot 10^{-21}$
2,660.73	$2.56 \cdot 10^{-24}$	$3.47 \cdot 10^{-22}$	$2.84 \cdot 10^{-21}$	$2.12 \cdot 10^{-21}$	$2.5 \cdot 10^{-21}$
2,985.38	$2.34 \cdot 10^{-24}$	$3.93 \cdot 10^{-22}$	$3 \cdot 10^{-21}$	$2.38 \cdot 10^{-21}$	$2.78 \cdot 10^{-21}$
3,349.65	$2.53 \cdot 10^{-24}$	$4.48 \cdot 10^{-22}$	$3.22 \cdot 10^{-21}$	$2.71 \cdot 10^{-21}$	$3.11 \cdot 10^{-21}$
3,758.37	$2.6 \cdot 10^{-24}$	$5.14 \cdot 10^{-22}$	$3.51 \cdot 10^{-21}$	$3.11 \cdot 10^{-21}$	$3.52 \cdot 10^{-21}$
4,216.97	$2.88 \cdot 10^{-24}$	$5.95 \cdot 10^{-22}$	$3.88 \cdot 10^{-21}$	$3.61 \cdot 10^{-21}$	$4.04 \cdot 10^{-21}$

4,731.51	$2.78 \cdot 10^{-24}$	$6.92 \cdot 10^{-22}$	$4.34 \cdot 10^{-21}$	$4.23 \cdot 10^{-21}$	$4.67 \cdot 10^{-21}$
5,308.84	$2.92 \cdot 10^{-24}$	$8.14 \cdot 10^{-22}$	$4.95 \cdot 10^{-21}$	$5.02 \cdot 10^{-21}$	$5.47 \cdot 10^{-21}$
5,956.62	$2.62 \cdot 10^{-24}$	$9.61 \cdot 10^{-22}$	$5.7 \cdot 10^{-21}$	$6 \cdot 10^{-21}$	$6.46 \cdot 10^{-21}$
6,683.44	$2.81 \cdot 10^{-24}$	$1.14 \cdot 10^{-21}$	$6.63 \cdot 10^{-21}$	$7.22 \cdot 10^{-21}$	$7.69 \cdot 10^{-21}$
7,498.94	$2.2 \cdot 10^{-24}$	$1.36 \cdot 10^{-21}$	$7.77 \cdot 10^{-21}$	$8.739 \cdot 10^{-21}$	$9.21 \cdot 10^{-21}$

Table C.2: DM upper-limit values for GrISU-based analysis that are displayed in Fig. 6.22-6.25. The energy is in units of GeV and the cross sections are in units of cm^3s^{-1}.

Energy	$\gamma\gamma$	$\tau\tau$	bb	WW	ZZ
Boötes I					
298.538	$9.73063 \cdot 10^{-24}$	0	0	0	0
334.965	$1.35533 \cdot 10^{-23}$	$7.60445 \cdot 10^{-21}$	$7.34755 \cdot 10^{-21}$	$8.79289 \cdot 10^{-20}$	$2.59706 \cdot 10^{-19}$
375.837	$1.59422 \cdot 10^{-23}$	$2.01778 \cdot 10^{-21}$	$5.5682 \cdot 10^{-21}$	$2.47095 \cdot 10^{-20}$	$5.61067 \cdot 10^{-20}$
421.697	$1.7704 \cdot 10^{-23}$	$1.37175 \cdot 10^{-21}$	$7.27084 \cdot 10^{-21}$	$1.4836 \cdot 10^{-20}$	$2.80386 \cdot 10^{-20}$
473.151	$1.78481 \cdot 10^{-23}$	$9.50018 \cdot 10^{-22}$	$7.87962 \cdot 10^{-21}$	$9.07707 \cdot 10^{-21}$	$1.52012 \cdot 10^{-20}$
530.884	$1.99518 \cdot 10^{-23}$	$8.61578 \cdot 10^{-22}$	$9.73004 \cdot 10^{-21}$	$7.48489 \cdot 10^{-21}$	$1.15845 \cdot 10^{-20}$
595.662	$2.11949 \cdot 10^{-23}$	$7.81031 \cdot 10^{-22}$	$1.08263 \cdot 10^{-20}$	$6.3358 \cdot 10^{-21}$	$9.30989 \cdot 10^{-21}$
668.344	$2.11987 \cdot 10^{-23}$	$7.40326 \cdot 10^{-22}$	$1.16205 \cdot 10^{-20}$	$5.71513 \cdot 10^{-21}$	$8.10751 \cdot 10^{-21}$
749.894	$2.18965 \cdot 10^{-23}$	$6.85703 \cdot 10^{-22}$	$1.14358 \cdot 10^{-20}$	$5.0981 \cdot 10^{-21}$	$7.05302 \cdot 10^{-21}$
841.395	$2.11486 \cdot 10^{-23}$	$6.45795 \cdot 10^{-22}$	$1.08843 \cdot 10^{-20}$	$4.65652 \cdot 10^{-21}$	$6.31947 \cdot 10^{-21}$
944.061	$2.14803 \cdot 10^{-23}$	$6.4875 \cdot 10^{-22}$	$1.06349 \cdot 10^{-20}$	$4.55397 \cdot 10^{-21}$	$6.08217 \cdot 10^{-21}$
1,059.25	$2.025 \cdot 10^{-23}$	$6.46101 \cdot 10^{-22}$	$1.00179 \cdot 10^{-20}$	$4.42418 \cdot 10^{-21}$	$5.82437 \cdot 10^{-21}$
1,188.50	$2.0299 \cdot 10^{-23}$	$6.6303 \cdot 10^{-22}$	$9.53942 \cdot 10^{-21}$	$4.43425 \cdot 10^{-21}$	$5.75801 \cdot 10^{-21}$
1,333.52	$2.41056 \cdot 10^{-23}$	$7.04412 \cdot 10^{-22}$	$9.29546 \cdot 10^{-21}$	$4.60611 \cdot 10^{-21}$	$5.90048 \cdot 10^{-21}$
1,496.24	$2.06039 \cdot 10^{-23}$	$7.40664 \cdot 10^{-22}$	$8.91329 \cdot 10^{-21}$	$4.74124 \cdot 10^{-21}$	$5.99103 \cdot 10^{-21}$
1,678.80	$2.07873 \cdot 10^{-23}$	$8.01867 \cdot 10^{-22}$	$8.78919 \cdot 10^{-21}$	$5.03295 \cdot 10^{-21}$	$6.27196 \cdot 10^{-21}$
1,883.65	$2.00077 \cdot 10^{-23}$	$8.71732 \cdot 10^{-22}$	$8.72027 \cdot 10^{-21}$	$5.37541 \cdot 10^{-21}$	$6.60509 \cdot 10^{-21}$
2,113.49	$1.98179 \cdot 10^{-23}$	$9.64167 \cdot 10^{-22}$	$8.84034 \cdot 10^{-21}$	$5.85488 \cdot 10^{-21}$	$7.09271 \cdot 10^{-21}$
2,371.37	$1.98118 \cdot 10^{-23}$	$1.07569 \cdot 10^{-21}$	$9.09324 \cdot 10^{-21}$	$6.45017 \cdot 10^{-21}$	$7.70323 \cdot 10^{-21}$
2,660.73	$1.93993 \cdot 10^{-23}$	$1.21943 \cdot 10^{-21}$	$9.56937 \cdot 10^{-21}$	$7.2422 \cdot 10^{-21}$	$8.52711 \cdot 10^{-21}$
2,985.38	$2.02388 \cdot 10^{-23}$	$1.39806 \cdot 10^{-21}$	$1.02604 \cdot 10^{-20}$	$8.25014 \cdot 10^{-21}$	$9.57824 \cdot 10^{-21}$
3,349.65	$2.01793 \cdot 10^{-23}$	$1.61662 \cdot 10^{-21}$	$1.11805 \cdot 10^{-20}$	$9.51028 \cdot 10^{-21}$	$1.08896 \cdot 10^{-20}$
3,758.37	$2.23996 \cdot 10^{-23}$	$1.87443 \cdot 10^{-21}$	$1.23081 \cdot 10^{-20}$	$1.10282 \cdot 10^{-20}$	$1.2458 \cdot 10^{-20}$
4,216.97	$2.47758 \cdot 10^{-23}$	$2.18714 \cdot 10^{-21}$	$1.37329 \cdot 10^{-20}$	$1.29082 \cdot 10^{-20}$	$1.43912 \cdot 10^{-20}$

4,731.51	$3.81899 \cdot 10^{-23}$	$2.58112 \cdot 10^{-21}$	$1.55998 \cdot 10^{-20}$	$1.53223 \cdot 10^{-20}$	$1.68659 \cdot 10^{-20}$
5,308.84	$4.42729 \cdot 10^{-23}$	$3.04849 \cdot 10^{-21}$	$1.78406 \cdot 10^{-20}$	$1.82447 \cdot 10^{-20}$	$1.98365 \cdot 10^{-20}$
5,956.62	$4.57912 \cdot 10^{-23}$	$3.61299 \cdot 10^{-21}$	$2.05825 \cdot 10^{-20}$	$2.18419 \cdot 10^{-20}$	$2.34667 \cdot 10^{-20}$
6,683.44	$4.72723 \cdot 10^{-23}$	$4.32808 \cdot 10^{-21}$	$2.41108 \cdot 10^{-20}$	$2.64688 \cdot 10^{-20}$	$2.81138 \cdot 10^{-20}$
7,498.94	$5.17477 \cdot 10^{-23}$	$5.19101 \cdot 10^{-21}$	$2.83966 \cdot 10^{-20}$	$3.21592 \cdot 10^{-20}$	$3.37835 \cdot 10^{-20}$

Segue 1

188.365	$3.52 \cdot 10^{-25}$	0	0	0	0
211.349	$8.56 \cdot 10^{-26}$	0	0	0	0
237.137	$8.720 \cdot 10^{-26}$	0	0	0	0
266.073	$9.109 \cdot 10^{-26}$	0	0	0	0
298.538	$8.81 \cdot 10^{-26}$	0	0	0	0
334.965	$9.06 \cdot 10^{-26}$	$9.16 \cdot 10^{-23}$	$8.58 \cdot 10^{-23}$	$1.05 \cdot 10^{-21}$	$3.12 \cdot 10^{-21}$
375.837	$1.03 \cdot 10^{-25}$	$2.52 \cdot 10^{-23}$	$6.61 \cdot 10^{-23}$	$3.11 \cdot 10^{-22}$	$7.12 \cdot 10^{-22}$
421.697	$1.19 \cdot 10^{-25}$	$1.4 \cdot 10^{-23}$	$7.05 \cdot 10^{-23}$	$1.55 \cdot 10^{-22}$	$2.95 \cdot 10^{-22}$
473.151	$1.34 \cdot 10^{-25}$	$1.05 \cdot 10^{-23}$	$8.37 \cdot 10^{-23}$	$1.03 \cdot 10^{-22}$	$1.74 \cdot 10^{-22}$
530.884	$1.33 \cdot 10^{-25}$	$7.97 \cdot 10^{-24}$	$8.79 \cdot 10^{-23}$	$7.11 \cdot 10^{-23}$	$1.11 \cdot 10^{-22}$
595.662	$1.47 \cdot 10^{-25}$	$6.53 \cdot 10^{-24}$	$8.99 \cdot 10^{-23}$	$5.43 \cdot 10^{-23}$	$8.03 \cdot 10^{-23}$
668.344	$1.62 \cdot 10^{-25}$	$5.7 \cdot 10^{-24}$	$9.01 \cdot 10^{-23}$	$4.5 \cdot 10^{-23}$	$6.41 \cdot 10^{-23}$
749.894	$1.39 \cdot 10^{-25}$	$5.18 \cdot 10^{-24}$	$8.78 \cdot 10^{-23}$	$3.93 \cdot 10^{-23}$	$5.450 \cdot 10^{-23}$
841.395	$1.43 \cdot 10^{-25}$	$5.01 \cdot 10^{-24}$	$8.62 \cdot 10^{-23}$	$3.68 \cdot 10^{-23}$	$5 \cdot 10^{-23}$
944.061	$1.7 \cdot 10^{-25}$	$4.93 \cdot 10^{-24}$	$8.26 \cdot 10^{-23}$	$3.51 \cdot 10^{-23}$	$4.7 \cdot 10^{-23}$
1,059.25	$1.54 \cdot 10^{-25}$	$5.07 \cdot 10^{-24}$	$8.03 \cdot 10^{-23}$	$3.52 \cdot 10^{-23}$	$4.64 \cdot 10^{-23}$
1,188.50	$1.63 \cdot 10^{-25}$	$5.25 \cdot 10^{-24}$	$7.7 \cdot 10^{-23}$	$3.55 \cdot 10^{-23}$	$4.61 \cdot 10^{-23}$
1,333.52	$1.62 \cdot 10^{-25}$	$5.58 \cdot 10^{-24}$	$7.49 \cdot 10^{-23}$	$3.68 \cdot 10^{-23}$	$4.72 \cdot 10^{-23}$
1,496.24	$1.67 \cdot 10^{-25}$	$6.01 \cdot 10^{-24}$	$7.35 \cdot 10^{-23}$	$3.88 \cdot 10^{-23}$	$4.9 \cdot 10^{-23}$
1,678.80	$1.79 \cdot 10^{-25}$	$6.55 \cdot 10^{-24}$	$7.27 \cdot 10^{-23}$	$4.13 \cdot 10^{-23}$	$5.16 \cdot 10^{-23}$
1,883.65	$1.68 \cdot 10^{-25}$	$7.23 \cdot 10^{-24}$	$7.3 \cdot 10^{-23}$	$4.47 \cdot 10^{-23}$	$5.5 \cdot 10^{-23}$
2,113.49	$2.05 \cdot 10^{-25}$	$8.05 \cdot 10^{-24}$	$7.42 \cdot 10^{-23}$	$4.89 \cdot 10^{-23}$	$5.93 \cdot 10^{-23}$
2,371.37	$1.97 \cdot 10^{-25}$	$9.06 \cdot 10^{-24}$	$7.67 \cdot 10^{-23}$	$5.42 \cdot 10^{-23}$	$6.48 \cdot 10^{-23}$
2,660.73	$1.98 \cdot 10^{-25}$	$1.04 \cdot 10^{-23}$	$8.11 \cdot 10^{-23}$	$6.12 \cdot 10^{-23}$	$7.21 \cdot 10^{-23}$
2,985.38	$1.98 \cdot 10^{-25}$	$1.19 \cdot 10^{-23}$	$8.64 \cdot 10^{-23}$	$6.93 \cdot 10^{-23}$	$8.05 \cdot 10^{-23}$
3,349.65	$2.3 \cdot 10^{-25}$	$1.37 \cdot 10^{-23}$	$9.36 \cdot 10^{-23}$	$7.95 \cdot 10^{-23}$	$9.110 \cdot 10^{-23}$
3,758.37	$2.8 \cdot 10^{-25}$	$1.59 \cdot 10^{-23}$	$1.02 \cdot 10^{-22}$	$9.18 \cdot 10^{-23}$	$1.04 \cdot 10^{-22}$
4,216.97	$3.04 \cdot 10^{-25}$	$1.87 \cdot 10^{-23}$	$1.15 \cdot 10^{-22}$	$1.08 \cdot 10^{-22}$	$1.2 \cdot 10^{-22}$
4,731.51	$3.06 \cdot 10^{-25}$	$2.2 \cdot 10^{-23}$	$1.29 \cdot 10^{-22}$	$1.27 \cdot 10^{-22}$	$1.4 \cdot 10^{-22}$
5,308.84	$3.74 \cdot 10^{-25}$	$2.61 \cdot 10^{-23}$	$1.47 \cdot 10^{-22}$	$1.51 \cdot 10^{-22}$	$1.64 \cdot 10^{-22}$

5,956.62	$4.28 \cdot 10^{-25}$	$3.12 \cdot 10^{-23}$	$1.7 \cdot 10^{-22}$	$1.81 \cdot 10^{-22}$	$1.95 \cdot 10^{-22}$
6,683.44	$4.4 \cdot 10^{-25}$	$3.75 \cdot 10^{-23}$	$1.99 \cdot 10^{-22}$	$2.19 \cdot 10^{-22}$	$2.33 \cdot 10^{-22}$
7,498.94	$5.07 \cdot 10^{-25}$	$4.54 \cdot 10^{-23}$	$2.35 \cdot 10^{-22}$	$2.68 \cdot 10^{-22}$	$2.81 \cdot 10^{-22}$

Ursa Minor

237.137	$5.72 \cdot 10^{-25}$	0	0	0	0
266.073	$3.7 \cdot 10^{-25}$	0	0	0	0
298.538	$3.81 \cdot 10^{-25}$	0	0	0	0
334.965	$2.8 \cdot 10^{-25}$	$1.91 \cdot 10^{-22}$	$1.78 \cdot 10^{-22}$	$2.19 \cdot 10^{-21}$	$6.51 \cdot 10^{-21}$
375.837	$2.71 \cdot 10^{-25}$	$6.76 \cdot 10^{-23}$	$1.75 \cdot 10^{-22}$	$8.35 \cdot 10^{-22}$	$1.92 \cdot 10^{-21}$
421.697	$2.64 \cdot 10^{-25}$	$3.9 \cdot 10^{-23}$	$1.91 \cdot 10^{-22}$	$4.33 \cdot 10^{-22}$	$8.29 \cdot 10^{-22}$
473.151	$2.51 \cdot 10^{-25}$	$2.5 \cdot 10^{-23}$	$1.93 \cdot 10^{-22}$	$2.48 \cdot 10^{-22}$	$4.21 \cdot 10^{-22}$
530.884	$3.01 \cdot 10^{-25}$	$1.96 \cdot 10^{-23}$	$2.09 \cdot 10^{-22}$	$1.78 \cdot 10^{-22}$	$2.78 \cdot 10^{-22}$
595.662	$2.74 \cdot 10^{-25}$	$1.56 \cdot 10^{-23}$	$2.1 \cdot 10^{-22}$	$1.32 \cdot 10^{-22}$	$1.97 \cdot 10^{-22}$
668.344	$3.19 \cdot 10^{-25}$	$1.29 \cdot 10^{-23}$	$2.0 \cdot 10^{-22}$	$1.04 \cdot 10^{-22}$	$1.49 \cdot 10^{-22}$
749.894	$2.95 \cdot 10^{-25}$	$1.2 \cdot 10^{-23}$	$2.02 \cdot 10^{-22}$	$9.34 \cdot 10^{-23}$	$1.3 \cdot 10^{-22}$
841.395	$2.67 \cdot 10^{-25}$	$1.11 \cdot 10^{-23}$	$1.93 \cdot 10^{-22}$	$8.43 \cdot 10^{-23}$	$1.15 \cdot 10^{-22}$
944.061	$3.03 \cdot 10^{-25}$	$1.08 \cdot 10^{-23}$	$1.86 \cdot 10^{-22}$	$8.03 \cdot 10^{-23}$	$1.08 \cdot 10^{-22}$
1,059.25	$2.74 \cdot 10^{-25}$	$1.09 \cdot 10^{-23}$	$1.79 \cdot 10^{-22}$	$7.88 \cdot 10^{-23}$	$1.04 \cdot 10^{-22}$
1,188.50	$2.92 \cdot 10^{-25}$	$1.13 \cdot 10^{-23}$	$1.74 \cdot 10^{-22}$	$8.03 \cdot 10^{-23}$	$1.05 \cdot 10^{-22}$
1,333.52	$2.9 \cdot 10^{-25}$	$1.17 \cdot 10^{-23}$	$1.68 \cdot 10^{-22}$	$8.21 \cdot 10^{-23}$	$1.06 \cdot 10^{-22}$
1,496.24	$2.81 \cdot 10^{-25}$	$1.25 \cdot 10^{-23}$	$1.65 \cdot 10^{-22}$	$8.58 \cdot 10^{-23}$	$1.09 \cdot 10^{-22}$
1,678.80	$3.11 \cdot 10^{-25}$	$1.33 \cdot 10^{-23}$	$1.61 \cdot 10^{-22}$	$8.99 \cdot 10^{-23}$	$1.13 \cdot 10^{-22}$
1,883.65	$2.95 \cdot 10^{-25}$	$1.44 \cdot 10^{-23}$	$1.61 \cdot 10^{-22}$	$9.65 \cdot 10^{-23}$	$1.19 \cdot 10^{-22}$
2,113.49	$2.93 \cdot 10^{-25}$	$1.6 \cdot 10^{-23}$	$1.65 \cdot 10^{-22}$	$1.06 \cdot 10^{-22}$	$1.29 \cdot 10^{-22}$
2,371.37	$2.99 \cdot 10^{-25}$	$1.78 \cdot 10^{-23}$	$1.7 \cdot 10^{-22}$	$1.17 \cdot 10^{-22}$	$1.41 \cdot 10^{-22}$
2,660.73	$2.9 \cdot 10^{-25}$	$2 \cdot 10^{-23}$	$1.78 \cdot 10^{-22}$	$1.3 \cdot 10^{-22}$	$1.55 \cdot 10^{-22}$
2,985.38	$2.92 \cdot 10^{-25}$	$2.26 \cdot 10^{-23}$	$1.89 \cdot 10^{-22}$	$1.47 \cdot 10^{-22}$	$1.72 \cdot 10^{-22}$
3,349.65	$2.75 \cdot 10^{-25}$	$2.58 \cdot 10^{-23}$	$2.04 \cdot 10^{-22}$	$1.68 \cdot 10^{-22}$	$1.94 \cdot 10^{-22}$
3,758.37	$2.95 \cdot 10^{-25}$	$2.96 \cdot 10^{-23}$	$2.23 \cdot 10^{-22}$	$1.93 \cdot 10^{-22}$	$2.2 \cdot 10^{-22}$
4,216.97	$2.79 \cdot 10^{-25}$	$3.42 \cdot 10^{-23}$	$2.47 \cdot 10^{-22}$	$2.25 \cdot 10^{-22}$	$2.53 \cdot 10^{-22}$
4,731.51	$3 \cdot 10^{-25}$	$3.99 \cdot 10^{-23}$	$2.78 \cdot 10^{-22}$	$2.65 \cdot 10^{-22}$	$2.94 \cdot 10^{-22}$
5,308.84	$2.93 \cdot 10^{-25}$	$4.66 \cdot 10^{-23}$	$3.16 \cdot 10^{-22}$	$3.13 \cdot 10^{-22}$	$3.44 \cdot 10^{-22}$
5,956.62	$3.54 \cdot 10^{-25}$	$5.48 \cdot 10^{-23}$	$3.63 \cdot 10^{-22}$	$3.74 \cdot 10^{-22}$	$4.06 \cdot 10^{-22}$
6,683.44	$3.91 \cdot 10^{-25}$	$6.44 \cdot 10^{-23}$	$4.19 \cdot 10^{-22}$	$4.48 \cdot 10^{-22}$	$4.8 \cdot 10^{-22}$
7,498.94	$4.4 \cdot 10^{-25}$	$7.67 \cdot 10^{-23}$	$4.93 \cdot 10^{-22}$	$5.43 \cdot 10^{-22}$	$5.76 \cdot 10^{-22}$

Willman 1

375.837	$1.34 \cdot 10^{-24}$	$1.21 \cdot 10^{-22}$	$3.33 \cdot 10^{-22}$	$1.48 \cdot 10^{-21}$	$3.36 \cdot 10^{-21}$
421.697	$1.44 \cdot 10^{-24}$	$8.99 \cdot 10^{-23}$	$4.8 \cdot 10^{-22}$	$9.72 \cdot 10^{-22}$	$1.84 \cdot 10^{-21}$
473.151	$1.42 \cdot 10^{-24}$	$5.42 \cdot 10^{-23}$	$4.54 \cdot 10^{-22}$	$5.16 \cdot 10^{-22}$	$8.64 \cdot 10^{-22}$
530.884	$1.39 \cdot 10^{-24}$	$4.83 \cdot 10^{-23}$	$5.49 \cdot 10^{-22}$	$4.17 \cdot 10^{-22}$	$6.45 \cdot 10^{-22}$
595.662	$1.51 \cdot 10^{-24}$	$4.61 \cdot 10^{-23}$	$6.39 \cdot 10^{-22}$	$3.72 \cdot 10^{-22}$	$5.46 \cdot 10^{-22}$
668.344	$1.23 \cdot 10^{-24}$	$4.29 \cdot 10^{-23}$	$6.7 \cdot 10^{-22}$	$3.3 \cdot 10^{-22}$	$4.68 \cdot 10^{-22}$
749.894	$1.37 \cdot 10^{-24}$	$3.95 \cdot 10^{-23}$	$6.53 \cdot 10^{-22}$	$2.93 \cdot 10^{-22}$	$4.05 \cdot 10^{-22}$
841.395	$1.34 \cdot 10^{-24}$	$3.9 \cdot 10^{-23}$	$6.52 \cdot 10^{-22}$	$2.81 \cdot 10^{-22}$	$3.82 \cdot 10^{-22}$
944.061	$1.25 \cdot 10^{-24}$	$3.9 \cdot 10^{-23}$	$6.38 \cdot 10^{-22}$	$2.75 \cdot 10^{-22}$	$3.68 \cdot 10^{-22}$
1,059.25	$1.19 \cdot 10^{-24}$	$3.89 \cdot 10^{-23}$	$6.03 \cdot 10^{-22}$	$2.68 \cdot 10^{-22}$	$3.53 \cdot 10^{-22}$
1,188.50	$1.18 \cdot 10^{-24}$	$4.03 \cdot 10^{-23}$	$5.83 \cdot 10^{-22}$	$2.73 \cdot 10^{-22}$	$3.54 \cdot 10^{-22}$
1,333.52	$1.48 \cdot 10^{-24}$	$4.28 \cdot 10^{-23}$	$5.73 \cdot 10^{-22}$	$2.85 \cdot 10^{-22}$	$3.65 \cdot 10^{-22}$
1,496.24	$1.28 \cdot 10^{-24}$	$4.61 \cdot 10^{-23}$	$5.67 \cdot 10^{-22}$	$3.02 \cdot 10^{-22}$	$3.82 \cdot 10^{-22}$
1,678.80	$1.33 \cdot 10^{-24}$	$5.09 \cdot 10^{-23}$	$5.74 \cdot 10^{-22}$	$3.28 \cdot 10^{-22}$	$4.1 \cdot 10^{-22}$
1,883.65	$1.24 \cdot 10^{-24}$	$5.52 \cdot 10^{-23}$	$5.72 \cdot 10^{-22}$	$3.51 \cdot 10^{-22}$	$4.32 \cdot 10^{-22}$
2,113.49	$1.34 \cdot 10^{-24}$	$6.19 \cdot 10^{-23}$	$5.92 \cdot 10^{-22}$	$3.9 \cdot 10^{-22}$	$4.73 \cdot 10^{-22}$
2,371.37	$1.26 \cdot 10^{-24}$	$6.87 \cdot 10^{-23}$	$6.1 \cdot 10^{-22}$	$4.29 \cdot 10^{-22}$	$5.14 \cdot 10^{-22}$
2,660.73	$1.16 \cdot 10^{-24}$	$7.78 \cdot 10^{-23}$	$6.44 \cdot 10^{-22}$	$4.83 \cdot 10^{-22}$	$5.7 \cdot 10^{-22}$
2,985.38	$1.19 \cdot 10^{-24}$	$8.81 \cdot 10^{-23}$	$6.86 \cdot 10^{-22}$	$5.46 \cdot 10^{-22}$	$6.35 \cdot 10^{-22}$
3,349.65	$1.22 \cdot 10^{-24}$	$1.01 \cdot 10^{-22}$	$7.43 \cdot 10^{-22}$	$6.24 \cdot 10^{-22}$	$7.17 \cdot 10^{-22}$
3,758.37	$1.35 \cdot 10^{-24}$	$1.16 \cdot 10^{-22}$	$8.1 \cdot 10^{-22}$	$7.16 \cdot 10^{-22}$	$8.12 \cdot 10^{-22}$
4,216.97	$1.29 \cdot 10^{-24}$	$1.34 \cdot 10^{-22}$	$8.97 \cdot 10^{-22}$	$8.32 \cdot 10^{-22}$	$9.310 \cdot 10^{-22}$
4,731.51	$1.6 \cdot 10^{-24}$	$1.57 \cdot 10^{-22}$	$1.02 \cdot 10^{-21}$	$9.84 \cdot 10^{-22}$	$1.09 \cdot 10^{-21}$
5,308.84	$1.74 \cdot 10^{-24}$	$1.85 \cdot 10^{-22}$	$1.16 \cdot 10^{-21}$	$1.17 \cdot 10^{-21}$	$1.28 \cdot 10^{-21}$
5,956.62	$2 \cdot 10^{-24}$	$2.19 \cdot 10^{-22}$	$1.34 \cdot 10^{-21}$	$1.4 \cdot 10^{-21}$	$1.51 \cdot 10^{-21}$
6,683.44	$2.57 \cdot 10^{-24}$	$2.61 \cdot 10^{-22}$	$1.56 \cdot 10^{-21}$	$1.69 \cdot 10^{-21}$	$1.8 \cdot 10^{-21}$
7,498.94	$2.63 \cdot 10^{-24}$	$3.12 \cdot 10^{-22}$	$1.83 \cdot 10^{-21}$	$2.05 \cdot 10^{-21}$	$2.16 \cdot 10^{-21}$

Stacked

188.365	$4.46 \cdot 10^{-25}$	0	0	0	0
211.349	$9.84 \cdot 10^{-26}$	0	0	0	0
237.137	$9.22 \cdot 10^{-26}$	0	0	0	0
266.073	$6.22 \cdot 10^{-26}$	0	0	0	0
298.538	$5.71 \cdot 10^{-26}$	0	0	0	0
334.965	$5.40 \cdot 10^{-26}$	$6.56 \cdot 10^{-23}$	$6.16 \cdot 10^{-23}$	$7.54 \cdot 10^{-22}$	$2.24 \cdot 10^{-21}$

375.837	$5.75 \cdot 10^{-26}$	$1.94 \cdot 10^{-23}$	$5.09 \cdot 10^{-23}$	$2.39 \cdot 10^{-22}$	$5.47 \cdot 10^{-22}$
421.697	$6.23 \cdot 10^{-26}$	$1.04 \cdot 10^{-23}$	$5.22 \cdot 10^{-23}$	$1.15 \cdot 10^{-22}$	$2.19 \cdot 10^{-22}$
473.151	$6.28 \cdot 10^{-26}$	$7.21 \cdot 10^{-24}$	$5.697 \cdot 10^{-23}$	$7.07 \cdot 10^{-23}$	$1.20 \cdot 10^{-22}$
530.884	$6.82 \cdot 10^{-26}$	$5.42 \cdot 10^{-24}$	$5.91 \cdot 10^{-23}$	$4.85 \cdot 10^{-23}$	$7.57 \cdot 10^{-23}$
595.662	$7.00 \cdot 10^{-26}$	$4.40 \cdot 10^{-24}$	$6.00 \cdot 10^{-23}$	$3.69 \cdot 10^{-23}$	$5.45 \cdot 10^{-23}$
668.344	$7.65 \cdot 10^{-26}$	$3.79 \cdot 10^{-24}$	$5.94 \cdot 10^{-23}$	$3.02 \cdot 10^{-23}$	$4.31 \cdot 10^{-23}$
749.894	$7.07 \cdot 10^{-26}$	$3.45 \cdot 10^{-24}$	$5.82 \cdot 10^{-23}$	$2.65 \cdot 10^{-23}$	$3.68 \cdot 10^{-23}$
841.395	$6.76 \cdot 10^{-26}$	$3.27 \cdot 10^{-24}$	$5.63 \cdot 10^{-23}$	$2.43 \cdot 10^{-23}$	$3.31 \cdot 10^{-23}$
944.061	$7.77 \cdot 10^{-26}$	$3.20 \cdot 10^{-24}$	$5.40 \cdot 10^{-23}$	$2.32 \cdot 10^{-23}$	$3.10 \cdot 10^{-23}$
1,059.25	$6.95 \cdot 10^{-26}$	$3.22 \cdot 10^{-24}$	$5.18 \cdot 10^{-23}$	$2.28 \cdot 10^{-23}$	$3.01 \cdot 10^{-23}$
1,188.50	$7.31 \cdot 10^{-26}$	$3.32 \cdot 10^{-24}$	$4.98 \cdot 10^{-23}$	$2.30 \cdot 10^{-23}$	$3.00 \cdot 10^{-23}$
1,333.52	$7.43 \cdot 10^{-26}$	$3.49 \cdot 10^{-24}$	$4.82 \cdot 10^{-23}$	$2.36 \cdot 10^{-23}$	$3.04 \cdot 10^{-23}$
1,496.24	$7.18 \cdot 10^{-26}$	$3.73 \cdot 10^{-24}$	$4.72 \cdot 10^{-23}$	$2.48 \cdot 10^{-23}$	$3.14 \cdot 10^{-23}$
1,678.80	$7.54 \cdot 10^{-26}$	$4.03 \cdot 10^{-24}$	$4.67 \cdot 10^{-23}$	$2.63 \cdot 10^{-23}$	$3.29 \cdot 10^{-23}$
1,883.65	$7.19 \cdot 10^{-26}$	$4.41 \cdot 10^{-24}$	$4.68 \cdot 10^{-23}$	$2.84 \cdot 10^{-23}$	$3.59 \cdot 10^{-23}$
2,113.49	$8.04 \cdot 10^{-26}$	$4.90 \cdot 10^{-24}$	$4.77 \cdot 10^{-23}$	$3.11 \cdot 10^{-23}$	$3.78 \cdot 10^{-23}$
2,371.37	$8.00 \cdot 10^{-26}$	$5.48 \cdot 10^{-24}$	$4.92 \cdot 10^{-23}$	$3.43 \cdot 10^{-23}$	$4.11 \cdot 10^{-23}$
2,660.73	$7.89 \cdot 10^{-26}$	$6.19 \cdot 10^{-24}$	$5.16 \cdot 10^{-23}$	$3.84 \cdot 10^{-23}$	$4.54 \cdot 10^{-23}$
2,985.38	$7.83 \cdot 10^{-26}$	$7.05 \cdot 10^{-24}$	$5.49 \cdot 10^{-23}$	$4.35 \cdot 10^{-23}$	$5.07 \cdot 10^{-23}$
3,349.65	$7.83 \cdot 10^{-26}$	$8.07 \cdot 10^{-24}$	$5.94 \cdot 10^{-23}$	$4.96 \cdot 10^{-23}$	$5.70 \cdot 10^{-23}$
3,758.37	$9.03 \cdot 10^{-26}$	$9.27 \cdot 10^{-24}$	$6.46 \cdot 10^{-23}$	$5.70 \cdot 10^{-23}$	$6.47 \cdot 10^{-23}$
4,216.97	$9.27 \cdot 10^{-26}$	$1.08 \cdot 10^{-23}$	$7.16 \cdot 10^{-23}$	$6.63 \cdot 10^{-23}$	$7.42 \cdot 10^{-23}$
4,731.51	$9.191 \cdot 10^{-26}$	$1.26 \cdot 10^{-23}$	$8.07 \cdot 10^{-23}$	$7.82 \cdot 10^{-23}$	$8.64 \cdot 10^{-23}$
5,308.84	$1.08 \cdot 10^{-25}$	$1.48 \cdot 10^{-23}$	$9.17 \cdot 10^{-23}$	$9.25 \cdot 10^{-23}$	$1.01 \cdot 10^{-22}$
5,956.62	$1.17 \cdot 10^{-25}$	$1.75 \cdot 10^{-23}$	$1.06 \cdot 10^{-22}$	$1.11 \cdot 10^{-22}$	$1.19 \cdot 10^{-22}$
6,683.44	$1.29 \cdot 10^{-25}$	$2.08 \cdot 10^{-23}$	$1.22 \cdot 10^{-22}$	$1.33 \cdot 10^{-22}$	$1.42 \cdot 10^{-22}$
7,498.94	$1.25 \cdot 10^{-25}$	$2.49 \cdot 10^{-23}$	$1.44 \cdot 10^{-22}$	$1.62 \cdot 10^{-22}$	$1.70 \cdot 10^{-22}$

Table C.3: Line significance values for the CARE-based analysis that are displayed in Fig. 6.17. The energy is in units of GeV. Note: significances below $1 \cdot 10^{-5}$ is set to 0.

Energy	Segue 1	Ursa Minor	Segue 1 corr.	Ursa Minor corr.
188.365	0	0	0	0
211.349	$2.10 \cdot 10^{-1}$	0	0	0
237.137	0	0	0	0
266.073	0	0	0	0
298.538	1.06	0	$1.51 \cdot 10^{-3}$	0
334.965	0	0	0	0
375.837	0	0	0	0
421.697	1.43	2.73	$4.66 \cdot 10^{-2}$	1.56
473.151	0	0	0	0
530.884	0	2.03	0	$5.63 \cdot 10^{-1}$
595.662	0	$4.37 \cdot 10^{-1}$	0	0
668.344	1.61	0	$1.35 \cdot 10^{-1}$	0
749.894	2.22	0	$8.26 \cdot 10^{-1}$	0
841.395	0	0	0	0
944.061	0	0	0	0
1,059.25	$6.35 \cdot 10^{-1}$	0	0	0
1,188.50	$5.57 \cdot 10^{-1}$	0	0	0
1,333.52	0	0	0	0
1,496.24	0	0	0	0
1,678.80	$3.40 \cdot 10^{-1}$	0	0	0
1,883.65	0	0	0	0
2,113.49	$6.71 \cdot 10^{-1}$	0	0	0
2,371.37	0	0	0	0
2,660.73	$2.95 \cdot 10^{-1}$	0	0	0
2,985.38	0	0	0	0
3,349.65	0	0	0	0
3,758.37	0	0	0	0
4,216.97	$8.08 \cdot 10^{-2}$	0	0	0
4,731.51	0	$9.50 \cdot 10^{-2}$	0	0
5,308.84	0	$5.65 \cdot 10^{-1}$	0	0
5,956.62	$1.23 \cdot 10^{-1}$	0	0	0
6,683.44	$2.79 \cdot 10^{-1}$	0	0	0
7,498.94	0	0	0	0

Table C.4: Line significance values for the GrISU-based analysis that are displayed in Fig. 6.20. The energy is in units of GeV.

Energy	Segue 1	Boötes I	Ursa Minor	Draco	Willman 1
188.365	0	0	0	0	0
211.349	0	0	0	0	0
237.137	0	0	0	0	0
266.073	0	0	0	0	0
298.538	0	0	0	0	0
334.965	0	0	0	0	0
375.837	0	0	0	0	0
421.697	0	0	0	0	$7.13 \cdot 10^{-1}$
473.151	1.43	0	0	0	0
530.884	0	0	0	0	0
595.662	0	0	0	0	0
668.344	0	$6.30 \cdot 10^{-1}$	0	0	0
749.894	0	0	0	0	0
841.395	0	0	0	$4.87 \cdot 10^{-1}$	$1.95 \cdot 10^{-1}$
944.061	0	$1.87 \cdot 10^{-1}$	0	0	0
1,059.25	$5.81 \cdot 10^{-1}$	0	0	0	0
1,188.50	0	0	0	0	0
1,333.52	0	0	0	0	0
1,496.24	0	0	0	$9.82 \cdot 10^{-2}$	$2.72 \cdot 10^{-1}$
1,678.80	0	0	0	$3.88 \cdot 10^{-1}$	$8.64 \cdot 10^{-1}$
1,883.65	$7.07 \cdot 10^{-2}$	0	0	$1.91 \cdot 10^{-1}$	0
2,113.49	0	0	0	0	0
2,371.37	0	0	0	0	0
2,660.73	$3.39 \cdot 10^{-1}$	0	0	$3.49 \cdot 10^{-1}$	0
2,985.38	0	0	0	$1.65 \cdot 10^{-1}$	0
3,349.65	0	0	0	$2.05 \cdot 10^{-1}$	$1.08 \cdot 10^{-1}$
3,758.37	0	0	0	0	0
4,216.97	0	0	0	0	0
4,731.51	0	0	0	0	0
5,308.84	$8.74 \cdot 10^{-2}$	$1.65 \cdot 10^{-1}$	$1.93 \cdot 10^{-1}$	0	0
5,956.62	0	0	0	0	0
6,683.44	0	0	0	0	0
7,498.94	0	0	$1.41 \cdot 10^{-1}$	$1.88 \cdot 10^{-1}$	0

Energy	Segue 1 corr.	Boötes I corr.	Ursa Minor corr.	Draco corr.	Willman 1 corr.
188.365	0	0	0	0	0
211.349	0	0	0	0	0
237.137	0	0	0	0	0
266.073	0	0	0	0	0
298.538	0	0	0	0	0
334.965	0	0	0	0	0
375.837	0	0	0	0	0
421.697	0	0	0	0	0
473.151	$1.30 \cdot 10^{-3}$	0	0	0	0
530.884	0	0	0	0	0
595.662	0	0	0	0	0
668.344	0	0	0	0	0
749.894	0	0	0	0	0
841.395	0	0	0	0	0
944.061	0	0	0	0	0
1,059.25	0	0	0	0	0
1,188.50	0	0	0	0	0
1,333.52	0	0	0	0	0
1,496.24	0	0	0	0	0
1,678.80	0	0	0	0	0
1,883.65	0	0	0	0	0
2,113.49	0	0	0	0	0
2,371.37	0	0	0	0	0
2,660.73	0	0	0	0	0
2,985.38	0	0	0	0	0
3,349.65	0	0	0	0	0
3,758.37	0	0	0	0	0
4,216.97	0	0	0	0	0
4,731.51	0	0	0	0	0
5,308.84	0	0	0	0	0
5,956.62	0	0	0	0	0
6,683.44	0	0	0	0	0
7,498.94	0	0	0	0	0

Table C.5: Line significance values for the stacked analysis that are displayed in Fig. 6.26. The energy is in units of GeV.

Energy	CARE	GrISU	CARE corr.	GrISU corr.
188.365	0	0	0	0
211.349	$2.35 \cdot 10^{-1}$	0	0	0
237.137	$9.00 \cdot 10^{-1}$	0	$2.42 \cdot 10^{-2}$	0
266.073	0	0	0	0
298.538	0	0	0	0
334.965	0	0	0	0
375.837	0	0	0	0
421.697	1.66	0	$5.45 \cdot 10^{-1}$	0
473.151	0	$7.20 \cdot 10^{-1}$	0	$1.66 \cdot 10^{-3}$
530.884	0	0	0	0
595.662	0	0	0	0
668.344	1.31	0	$2.97 \cdot 10^{-1}$	0
749.894	1.59	0	$4.69 \cdot 10^{-1}$	0
841.395	0	0	0	0
944.061	0	0	0	0
1,059.25	$4.60 \cdot 10^{-1}$	$1.06 \cdot 10^{-1}$	$1.68 \cdot 10^{-4}$	0
1,188.50	$4.25 \cdot 10^{-1}$	$8.12 \cdot 10^{-2}$	$8.90 \cdot 10^{-5}$	0
1,333.52	0	0	0	0
1,496.24	0	0	0	0
1,678.80	$3.77 \cdot 10^{-2}$	0	0	0
1,883.65	0	0	0	0
2,113.49	0	0	0	0
2,371.37	0	0	0	0
2,660.73	$1.89 \cdot 10^{-2}$	$1.27 \cdot 10^{-1}$	0	0
2,985.38	0	0	0	0
3,349.65	0	0	0	0
3,758.37	0	0	0	0
4,216.97	0	0	0	0
4,731.51	0	0	0	0
5,308.84	$1.67 \cdot 10^{-1}$	$1.14 \cdot 10^{-1}$	0	0
5,956.62	0	0	0	0
6,683.44	$7.91 \cdot 10^{-2}$	0	0	0
7,498.94	0	$3.80 \cdot 10^{-2}$	0	0

Table C.6: Line significance values that are displayed in Fig. 6.29. GrISU based analysis using the CARE run list. The energy is in units of GeV.

Energy	Segue 1	Ursa Minor	Segue 1 corr.	Ursa Minor corr.
188.365	0	0	0	0
211.349	0	0	0	0
237.137	0	0	0	0
266.073	0	0	0	0
298.538	0	1.51	0	$4.02 \cdot 10^{-1}$
334.965	0	2.74	0	1.96
375.837	2.66	3.68	1.84	3.10
421.697	$6.39 \cdot 10^{-1}$	2.10	$2.17 \cdot 10^{-3}$	1.12
473.151	$8.24 \cdot 10^{-1}$	1.51	$1.34 \cdot 10^{-2}$	$3.97 \cdot 10^{-1}$
530.884	$9,85 \cdot 10^{-1}$	1.33	$4.28 \cdot 10^{-2}$	$2.37 \cdot 10^{-1}$
595.662	0	0	0	0
668.344	0	0	0	0
749.894	0	0	0	0
841.395	0	0	0	0
944.061	0	0	0	0
1,059.25	0	0	0	0
1,188.50	$6.61 \cdot 10^{-1}$	0	$2.78 \cdot 10^{-3}$	0
1,333.52	$8.13 \cdot 10^{-1}$	$6.55 \cdot 10^{-1}$	$1.22 \cdot 10^{-2}$	$3.21 \cdot 10^{-3}$
1,496.24	0	0	0	0
1,678.80	$5.32 \cdot 10^{-1}$	0	$5.30 \cdot 10^{-4}$	0
1,883.65	0	0	0	0
2,113.49	0	0	0	0
2,371.37	0	$6.70 \cdot 10^{-1}$	0	$3.80 \cdot 10^{-3}$
2,660.73	$6.31 \cdot 10^{-1}$	0	$1.96 \cdot 10^{-3}$	0
2,985.38	0	0	0	0
3,349.65	0	0	0	0
3,758.37	0	0	0	0
4,216.97	$4.07 \cdot 10^{-1}$	0	$6.28 \cdot 10^{-5}$	0
4,731.51	$2.38 \cdot 10^{-1}$	0	0	0
5,308.84	$4.84 \cdot 10^{-1}$	0	$2.50 \cdot 10^{-4}$	0
5,956.62	0	$2.78 \cdot 10^{-1}$	0	0
6,683.44	0	0	0	0
7,498.94	0	1.00	0	$5.41 \cdot 10^{-2}$

Table C.7: Stacked line significance values that are displayed in 6.32. GrISU based analysis using the CARE run list. The energy is in units of GeV.

Energy	CARE stacked	GrISU stacked	CARE corr.	GrISU corr.
188.365	0	0	0	0
211.349	$2.35 \cdot 10^{-1}$	0	0	0
237.137	$9.00 \cdot 10^{-1}$	0	$1.06 \cdot 10^{-2}$	0
266.073	0	0	0	0
298.538	0	0	0	0
334.965	0	0	0	0
375.837	0	2.70	0	1.89
421.697	1.66	$8.10 \cdot 10^{-1}$	$4.46 \cdot 10^{-1}$	$1.19 \cdot 10^{-2}$
473.151	0	1.19	0	$1.25 \cdot 10^{-1}$
530.884	0	$4.04 \cdot 10^{-1}$	0	$5.88 \cdot 10^{-5}$
595.662	0	0	0	0
668.344	1.31	0	$1.41 \cdot 10^{-1}$	0
749.894	1.59	0	$3.74 \cdot 10^{-1}$	0
841.395	0	0	0	0
944.061	0	0	0	0
1,059.25	$4.60 \cdot 10^{-1}$	0	$2.61 \cdot 10^{-5}$	0
1,188.50	$4.25 \cdot 10^{-1}$	$5.20 \cdot 10^{-1}$	$1.21 \cdot 10^{-5}$	$4.43 \cdot 10^{-4}$
1,333.52	0	$9.70 \cdot 10^{-1}$	0	$3.91 \cdot 10^{-2}$
1,496.24	0	0	0	0
1,678.80	$3.77 \cdot 10^{-2}$	$4.36 \cdot 10^{-1}$	0	$1.10 \cdot 10^{-4}$
1,883.65	0	0	0	0
2,113.49	0	0	0	0
2,371.37	0	0	0	0
2,660.73	$1.89 \cdot 10^{-2}$	0	0	0
2,985.38	0	0	0	0
3,349.65	0	0	0	0
3,758.37	0	0	0	0
4,216.97	0	0	0	0
4,731.51	0	$4.24 \cdot 10^{-2}$	0	0
5,308.84	$1.67 \cdot 10^{-1}$	$2.09 \cdot 10^{-1}$	0	0
5,956.62	0	$3.69 \cdot 10^{-1}$	0	$2.81 \cdot 10^{-5}$
6,683.44	$7.91 \cdot 10^{-2}$	0	0	0
7,498.94	0	$1.57 \cdot 10^{-1}$	0	0

Selbstständigkeitserklärung

Hiermit versichere ich, dass ich die vorliegende Dissertation mit dem Titel "Dark Matter line search using 3D-modeling of Cherenkov showers < 10 TeV with VERITAS" selbstständig verfasst und nur die angegebenen Quellen und Hilfsmittel verwendet habe. Diese Arbeit wurde bisher an keiner anderen Hochschule eingereicht.

Potsdam, den 12th July 2017

Nils Håkansson